Department of Physics and Astronomy

University of Heidelberg

Bachelor Thesis in Physics

submitted by

Dongyu Lin

born in Zhengzhou (China)

2018

First Observation of the Decay $\Lambda_b^0 \rightarrow \Lambda_c^+ D^- \overline{K}^* (892)^0$ at the LHCb Experiment

This Bachelor Thesis has been carried out by Dongyu Lin at the
Physicalisches Institut in Heidelberg
under the supervision of
Dr. Sebastian Neubert

Abstract

The first observation of the decay $\Lambda_{\mathrm{b}}^{0} \rightarrow \Lambda_{\mathrm{c}}^{+}\mathrm{D}^{-}\overline{\mathrm{K}}^{*}(892)^{0}$ is presented in this thesis, using data corresponding to an integrated luminosity of $3.0\,\mathrm{fb}^{-1}$ collected at center-of-mass proton-proton colliding energies of $7\,\mathrm{TeV}$ and $8\,\mathrm{TeV}$ in 2011 and 2012 by the LHCb detector. The measured efficiency corrected signal yields are $N_{\Lambda_{\mathrm{b}}^{0}\rightarrow\Lambda_{\mathrm{c}}^{+}\mathrm{D}^{-}\overline{\mathrm{K}}^{*0},\mathrm{corr}} = 8900 \pm 1900$, with statistical error. A future branching fraction measurement with reference to the normalization channel $\Lambda_{\mathrm{b}}^{0} \rightarrow \Lambda_{\mathrm{c}}^{+}\mathrm{D}_{\mathrm{s}}^{-}$ can be performed, which allows an amplitude analysis of resonances of the $\Lambda_{\mathrm{c}}^{+}\mathrm{D}^{-}$ subsystem for the search for the neutral isospin partners of pentaquarks $\mathrm{P}_{\mathrm{c}}(4380)^{+}$ and $\mathrm{P}_{\mathrm{c}}(4450)^{+}$ observed in 2015 at LHCb.

Kurzfassung

Diese Arbeit widmet sich zur ersten Entdeckung des Zerfalls $\Lambda_{\mathrm{b}}^{0} \rightarrow \Lambda_{\mathrm{c}}^{+}\mathrm{D}^{-}\overline{\mathrm{K}}^{*}(892)^{0}$, extrahiert von Daten gesammelt vom LHCb Detektor in Proton-Proton-Kollisionen bei $\sqrt{s} = 7\,\mathrm{MeV}$ und $\sqrt{s} = 8\,\mathrm{MeV}$ im Jahr 2011 und 2012, welche einer integrierten Luminosität entsprechen. Die gemessene Anzahl der Ereignisse des Zerfalls mit Effizienzkorrektur beträgt $N_{\Lambda_{\mathrm{b}}^{0}\rightarrow\Lambda_{\mathrm{c}}^{+}\mathrm{D}^{-}\overline{\mathrm{K}}^{*0},\mathrm{corr}} = 8900 \pm 1900$, mit statistischem Fehler. Eine zukünftige Messung des Verzweigungsverhältnises relativ zum norminalen Zerfall $\Lambda_{\mathrm{b}}^{0} \rightarrow \Lambda_{\mathrm{c}}^{+}\mathrm{D}_{\mathrm{s}}^{-}$ kann durchgeführt werden, welche eine Amplitudenanalyse erlaubt, um die Resonanzen im $\Lambda_{\mathrm{c}}^{+}\mathrm{D}^{-}$ System zu studieren, die zur Suche nach den neutralen Isospinpaaren der im Jahr 2015 beobachteten Pentaquarks $\mathrm{P}_{\mathrm{c}}(4380)^{+}$ and $\mathrm{P}_{\mathrm{c}}(4450)^{+}$ bei LHCb führt.

Acknowledgements

This part is dedicated to the people, from whom I have received support in the last six months.

Firstly, I would like to thank my supervisor, Dr. Sebastian Neubert, for giving me the precious opportunity to work in the Heidelberg LHCb group and his critical comments, without which this thesis could not have been done. His leadership pushes the whole group towards success.

Secondly, I would like to thank Dr. Nicola Skidmore, for her collaboration on this analysis and selfless mentoring on a daily basis. Her relentless work on producing the real and simulated data and training the $\mathrm{D^-BDT}$ is the key to this first observation. I feel lucky and honored to be able to work with her, learn from her and be motivated by her.

I would also like to express my appreciation for the readiness and willingness of Dr. Marian Stahl and Alessio Piucci, to help me with assorted problems from technical to physical ones. The software frameworks used in this thesis for applying cuts, all fit procedures, training and applying BDTs are developed by the Heidelberg LHCb group [1]. My sincere thanks goes to the developers. Thank you to my fellow students Jan Maintok, Julian Bollig, Philipp Schultzen, Nils Hoyer and Bernd Mumme for not only sharing the same office, but the same passion for the work as well.

I would like to use this chance to thank my parents, who support me unconditionally. My special thanks goes to Yuwei Zhou. She will always be a source of inspiration.

My final thanks goes to the Heidelberg LHCb group, for providing me this experience in such a wonderful working environment and the unforgetable afternoon snacks.

Contents

Introduction

This thesis is devoted to the first observation of the decay mode $\Lambda_b^0 \rightarrow \Lambda_c^+ D^- \overline{K}^* (892)^0$, extracted from datasets corresponding to an integrated luminosity of $3.0\,\mathrm{fb}^{-1}$ collected at center-of-mass proton-proton colliding energies of $7\,\mathrm{TeV}$ and $8\,\mathrm{TeV}$ in 2011 and 2012 (run I data) by the LHCb detector. The efficieny corrected signal yields of the decay $\Lambda_b^0 \rightarrow \Lambda_c^+ D^- \overline{K}^{*0}$ (the signal channel) are measured. Being well-studied, this decay channel allows a future study on resonances of the $\Lambda_c^+ D^-$ subsystem, which would have a minimal quark content of $c\bar{c}udd$. These resonances could be pentaquark candidates, which are the neutral isospin partners to the pentaquark candidates with the quark content $c\bar{c}uud$ observed in 2015 [2].

The first step is to establish the decay channel, using a cut-based selection. Multi-dimensional mass fits and a brief efficiency study are conducted, to extract the efficiency corrected signal yields. The next step is to reexamine the decay channel, using a selecion involving two boosted decision trees (BDTs) and rectangular cuts. The efficiency corrected signal yields are obtained from mass fits and an efficiency study, which is compared to the measured efficiency corrected signal yields in the first step.

The thesis consists of nine sections. Section I provides a brief overview of the Standard Model of particle physics (SM). Section II is an introduction of the LHCb experiment. Section III gives a short summary of pentaquark searches. Section IV presents the cut-based selection, which is used to establish the signal decay from the data, and mass fits, which estiamte backgrounds related to partially reconstructed decays and the signal decay and deliver the signal yields. Efficiency corrected signal yields are given after a short efficiency study. This section serves as a first exploration of the runI data and a preparation for the offline selection using a combination of BDTs and one-dimensional cuts and corresponding mass fits, which are presented in Section V and VI. Section VII is devoted to an efficiency study. The measured efficiency corrected yields and a brief comparsion between the measured signal yields using two different selection methods are given in Section VIII. Systematic uncertainties are briefly discussed. Section IX concludes this thesis and provides an outlook for future study of this decay channel.

1 Brief Overview of the Standard Model

The Standard Model of particle physics describes the elementary particles and the interactions between them [3]. The elementary particles are divided into the fundamental fermions, which constitute matter, and the fundamental bosons, which mediate the interaction between the fundamental fermions. The fundamental fermions have spin $\frac{1}{2}$ and are further divided into six quarks and six leptons. The six different types of quarks and leptons are called six flavors. The quarks and lepton are divided into three generations. In each generation, there is a charged ($q = -e$) lepton, a neutral neutrino, a positive charged ($q = \frac{2}{3}e$) quark and a negative charged ($q = -\frac{1}{3}e$) quark. The twelve fundamental fermion are listed in Table 1 with their masses charges.

	First Generation			**Second Generation**			**Third Generation**		
type	flavor	q/e	m/GeV	flavor	q/e	m/GeV	flavor	q/e	m/GeV
Quarks	up (u)	$+\frac{2}{3}$	0.005	charm (c)	$+\frac{2}{3}$	1.3	top (t)	$+\frac{2}{3}$	174
	down (d)	$-\frac{1}{3}$	0.003	strange (s)	$-\frac{1}{3}$	0.1	bottom (b)	$-\frac{1}{3}$	4.5
Leptons	electron (e^-)	-1	0.0005	muon (μ^-)	-1	0.106	tau (τ^-)	-1	1.78
	electron neutrino (ν_e)	0	$< 10^{-9}$	muon neutrino (ν_μ)	0	$< 10^{-9}$	tau neutrino (ν_τ)	0	$< 10^{-9}$

Table 1: The fundamental fermions with their charges and masses.

The three fundamental forces (electromagnetic, strong and weak forces) are described by quantum field theories (QFTs) corresponding to the exchange of spin 1 gauge bosons. The interactions between charged particles are mediated via exchange of virtual photons are described by quantum electrodynamics (QED). Gluons are the force-carriers of the strong interactions between quarks, which are described by quantum chromodynamics (QCD). The weak charged-current interaction and weak neutral-current interction are mediated by the charged $\mathrm{W}^{\pm}$ bosons and the neutral Z boson. The gauge bosons and the forces that they carry are listed in Table 2. The Higgs boson, the last element of the SM, was dicovered in 2012 [4, 5], which has a mass of $m_{\mathrm{H}} \approx 125\,\mathrm{GeV}$ and spin 0. In the SM, the Higgs boson assigns masses to other fundamental particles through the Higgs mechanism. Because of the half-interger spin, the fundamenal fermions follow Fermi-Dirac statistics. On the contrary, the fundamental bosons have integer spin (1 for the four gauge bosons and 0 for the Higgs boson) and follow Bose-Einstein statistics. In QFT, a gauge boson couples to a elementary particle only when it carries the charge of the associated interaction. The charge associated with QED is the electric charge, while the charges associated with QCD and the weak interaction are the color charge and the weak isospin. The coupling of the gauge bosons to other particles can be described by an interaction vertex, which is the intersection of the gauge boson, one incoming particle and one outgoing particle, using Feynman rules [6]. These concepts are illustrated in the following.

name	q/e	m/GeV	force
photon (γ)	0	0	electromagnetic
gluon (g)	0	0	strong
W boson ($\mathrm{W}^{\pm}$)	±1	80.4	weak
Z boson (Z)	0	91.2	

Table 2: The gauge bosons with their charges, masses and the forces that they carry.

1.1 The Electromagnetic Interaction

In QED, the charge carried by a particle that allows it couple to the photon is the electric charge. Due to electric charge conservation and flavor conservation at the interaction vertex, a vertex in QED correspond to either annihilation, creation of a particle-antiparticle pair or scattering of a charged particle at the presence of another charged particle. The coupling strength is described by a scalar $\alpha \approx \frac{1}{137}$. Three examples are given in Figure 1 to illustrate the QED vertices.

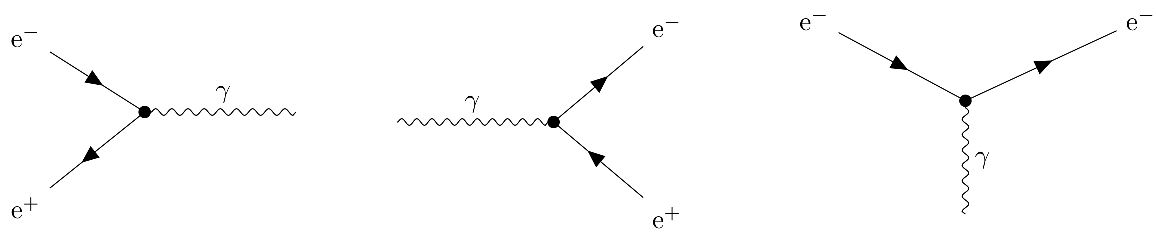

(a) $\mathrm{e}^-\mathrm{e}^+$ pair annihilation.

(b) $\mathrm{e}^-\mathrm{e}^+$ pair creation.

(c) e^- scattering in the electric potential of another charged particles.

Figure 1: Examples of QED vertices.

1.2 The Strong Interaction

In QCD, the charge responsible for the strong interaction is the color charge. Since only quarks and gluons carry color charges, only they participate in the strong interaction. So far no free quark has been observed, which motivates the hypothesis of color confinement, which requires that color charged particles be confined to color singlet states [7]. Consequently the quarks are always observed in bounded states, which takes the form of mesons ($\mathrm{q\overline{q}}$), baryons (qqq) and anti-baryons ($\overline{\mathrm{qqq}}$). Because of electric charge conservation, flavor conservation and color conservation at the strong interaction vertex, a vertex in QCD represents the interaction between two quarks via a gluon or self-interactions of gluons. The coupling strength at a QCD vertex is given by α_S. Experiments studying τ decay, deep inelastic scattering of electrons, $\mathrm{e}^+\mathrm{e}^-$ annilation and quarkonia showed evidence that the coupling strength α_S becomes smaller (~ 0.1) when $|q| > 100\,\mathrm{GeV}$, where q is the four-momentum of the exchange particle at the vertex. This is known as asymptotic freedom. This is quite convenient for experiments involving high-energy particle accelerators, since with

$\alpha_S \sim 0.1$, perturbation theory is applicable. However, the value of α_S is not so small that higher-order correction for a process is negligible. This remains as a challenge for the study of QCD. Some QCD vertices are demonstrated in Figure 2 as an example.

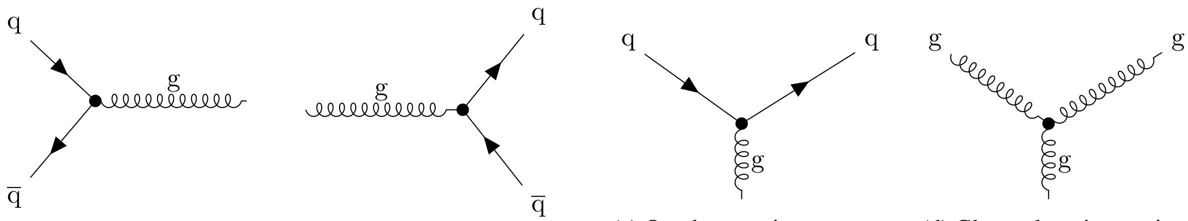

(a) q$\overline{\text{q}}$ pair annihilation. (b) q$\overline{\text{q}}$ pair creation. (c) Quark scattering process. (d) Gluon-gluon interaction.

Figure 2: Examples of QCD vertices.

1.3 The Weak Interaction

In quantum mechanics, the parity operation can be associated with its operator $\hat{P}$, which is defined as

$$\psi\left(\vec{x}, t\right) \rightarrow \psi'\left(\vec{x}, t\right) = \hat{P}\psi\left(\vec{x}, t\right) = \psi\left(-\vec{x}, t\right), \tag{1}$$

which is equivalent to spatial inversion [8]. It can be easily shown that parity is conserved in QED and QCD, by applying the parity operator for Dirac spinors[1] to the QED and QCD four-vector currents [9]. Parity violation was first proposed by T. D. Lee and C. N. Yang [10] in 1956 and experimentally proven in the Wu experiment [11] in 1957. The V-A structure was then proposed for the current-current interaction, where the interference of the V and A parts gives rise to the parity violation and the chiral structure of the weak interaction in the limit $E \gg m$ for the interacting particles, which can be verbally described as "only left-handed chiral particles and right-handed chiral antiparticles participate in the charged-current weak interaction" [7]. Experimentally it was found that the charged-current weak interaction is mediated by $\mathrm{W}^{\pm}$ boson [12, 13]. The signal decay involves two weak interaction vertices mediated via a W^{-} boson (see Figure 6 (a)).

2 The LHCb Detector

The Large Hadron Collider beauty (LHCb) experiment is one of the seven experiments that are currently running at the Large Hadron Collider (LHC) at the European Organization for Nuclear Research (CERN, French: conseil

[1] It can be shown that the parity operator for Dirac spinors can be written in matrix representation as $\hat{P} = \begin{pmatrix} 1 & 0 & 0 & 0 \\ 0 & 1 & 0 & 0 \\ 0 & 0 & -1 & 0 \\ 0 & 0 & 0 & -1 \end{pmatrix}$

européen pour la recherche nucléaire). It is designed to investigate why our universe mainly consists of matter rather than antimatter by studying the CP violation involving b quark [14]. The LHCb detector is a single-arm forward spectrometer, of a weight of 5600 tons and a volume of $21 \times 13 \times 10\,\mathrm{m}^3$, for the purpose of precise measurement of decays of the b quark. The main contribution to beauty production at the LHC is gluon-gluon fusion [15, 16]. Two patrons participating in the creation of a $\mathrm{b\overline{b}}$ pair have asymmetrical momenta, causing a boost of the $\mathrm{b\overline{b}}$ pair along the beam axis in the laboratory frame [17]. Comparing deviations between the results from precise measurements to SM predictions may reveal new physics beyond the SM.

2.1 The Large Hadron Collider

The LHC collides pp, pPb and PbPb beams, with a series of accelerating structures, inside a 27-kilometer ring of superconducting magnets, to test the theoretical predictions in particle physics and search for new physics beyond the SM. The LHC was operated for proton-proton collision at center-of-mass energies $7\,\mathrm{TeV}$ in 2011, $8\,\mathrm{TeV}$ in 2012 and $13\,\mathrm{TeV}$ in 2015 and 2016 respectively [18].

2.2 The LHCb Design

With the large $\mathrm{b\overline{b}}$ production cross section of $\sim\, 500\mu\mathrm{b}$ expected at an energy of $14\,\mathrm{TeV}$, the LHC will be the largest b quark factory in the world. With a luminosity of $2 \times 10^{32}\,\mathrm{cm}^{-2}\mathrm{s}^{-1}$, 10^{12} $\mathrm{b\overline{b}}$ pairs would be produced in $10^7\,\mathrm{s}$, corresponding to the canonical one year of data taking at LHCb [14]. This moderate luminosity allows simpler analysis with less primary pp interactions and reduces radiation damage to the detector. The LHCb detector is located near the intersection point 8 of the LHC to detect the forward flying particles from the pp collision. Besides its superb capability for b quark research, LHCb is also a prominent charm factory [19, 20]. In the following each of the subdetectors is briefly explained. A schematic side view of the LHCb detector is given in Figure 3 [21].

2.2.1 Vertex Locator

The vertex locator (VELO) measures tracks of charged particles near the interaction point to reconstruct the primary vertices and the displaced secondary vertices of b or c-hadrons, which are distinctive feature of b and c-hadron decays [22]. In this way, the VELO allows lifetime measurement of b and c-hadrons and the impact parameter (IP) (see section 4.1) of the tracks of charged particles, which is an important parameter to distinguish the prompt particles, which are coming from the pp collision, from the secondary particles from b and c-hadron decays. The VELO can detect particles with pseudorapidity[2] $1.6 < \eta < 4.9$ and within $10.6\,\mathrm{cm}$ range from the colliding point.

The VELO consists of many layers silicon modules, ϕ-modules and r-modules, which measure the radial distance r of a track to the beam and the azimuthal angle ϕ perpendicular to the beam direction and are divided in two halves.

[2] The pseudorapidity is defined as $\eta := -\ln\left(\tan\frac{\theta}{2}\right)$.

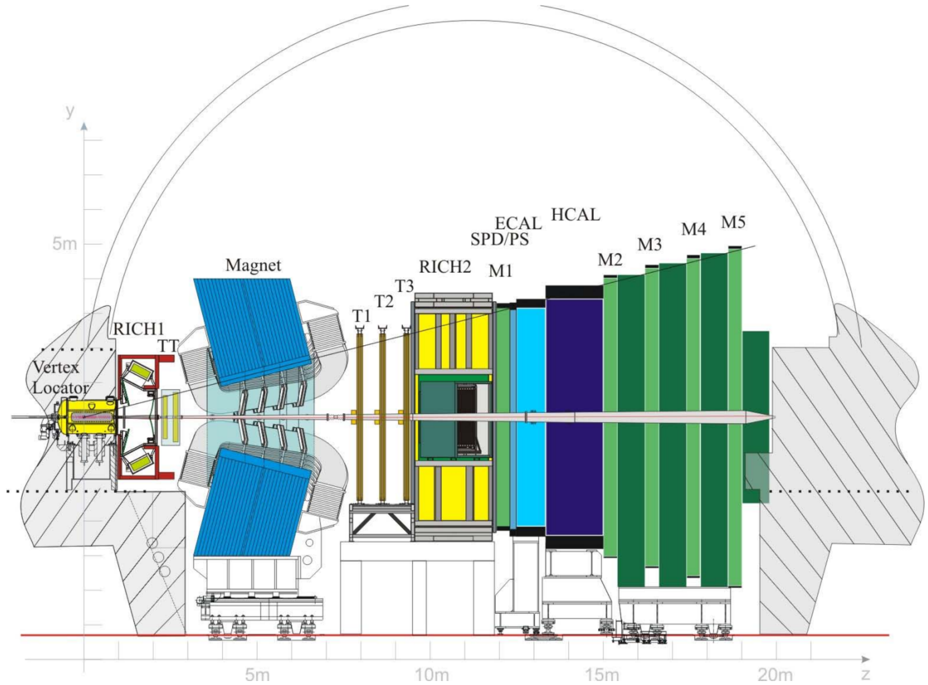

Figure 3: Schematic side view of the LHCb detector.

The two module types are alternately mounted at fixed position along the beam direction. The choice of $r\phi$ coordinates allows a fast track reconstruction in the LHCb trigger. With the measured r and ϕ and the position of the modules, 3D cylindrical coordinates of a track can be fully reconstructed.

An interesting feature of the VELO design is that the two halves are movable. The VELO is in open position with a separation of $6\,\mathrm{cm}$ during the tuning of the beam to avoid unnecessary radiation damage. Once the beam is stablized, it is switched to closed position for vertex reconstruction, at a distance of $8.2\,\mathrm{mm}$ to the beam. A schematic overview of the VELO is shown in Figure 4 [23].

2.2.2 Magnet

A dipole magnet of two coils generating an integrated magnetic field of $4\,\mathrm{Tm}$ in the y-direction is mounted 5 meters away from the colliding point, to meet the demand for momentum measurement for charged particles with a precision of about 0.4% for momenta up to $200\,\mathrm{GeV}$ [24]. Using the fact that a charged particle experiences the Lorentz force in a magnetic field and undergoes a circular motion, its momentum can be measured with given magnetic field strength and radius of the circular motion. The design of the LHCb detector (a forward spectrometer) requires magnet with an angualar coverage of $\pm 250\,\mathrm{mrad}$ vertically and $\pm 300\,\mathrm{mrad}$ horizontally to exploit the forward region of the pp collisions. The polarity changes during data taking, to avoid potential detector bias.

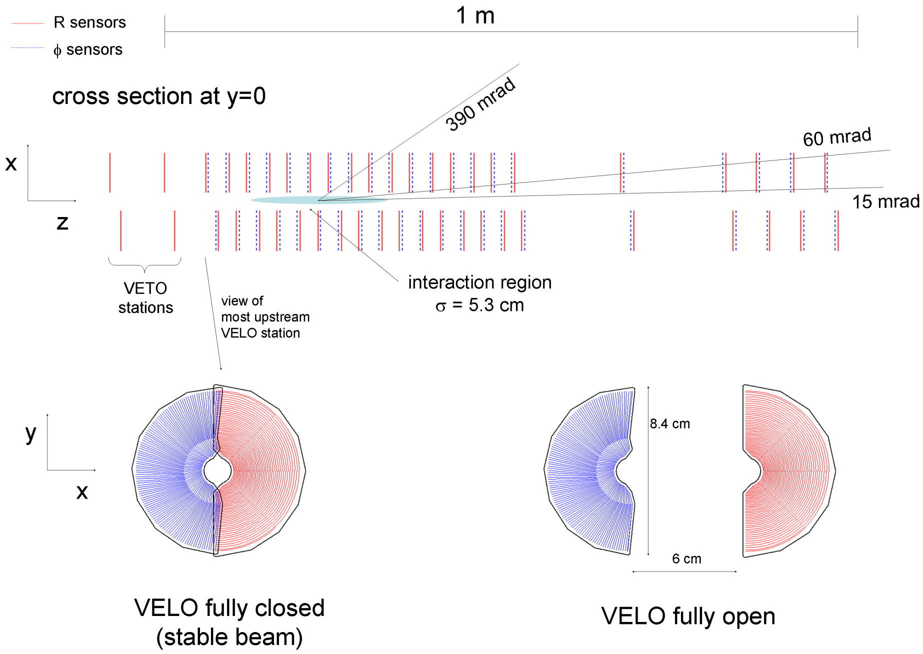

Figure 4: Overview diagram showing spacing of modules along z direction, and positions open and closed.

2.2.3 Tracking Stations

There are four planar tracking stations in the LHCb detector: the Tracker Turicensis (TT), which is mounted between RICH I and the magnet, T1, T2 and T3, which are located between the magnet and RICH II. Silicon microstrip detectors are used in the TT and in the Inner Trackers (ITs) of T1-T3, which are the sections near the beam [25]. The Outer Tracker (OT), the rest part of T1-T3, uses straw-tubes [26]. Like the VELO, the traking stations measure the 2D-coordinates of tracks of charged particles inside their own planes. Along with their mounted positions, 3D-coordinates of the tracks can be reconstructed for charged particles. For a given magnetic field, the momentum and charge (negative or positive) of a charged particle can be measured from the shape of its track.

2.2.4 Ring Imaging Cherenkov Detectors

Two Ring Imaging Cherenkov Detectors (RICH) are implemented in the LHCb detector for particle identification (PID). RICH I, which is located between the VELO and the TT, is used for PID of charged particles with low momenta ($p \sim 1 - 60\,\mathrm{GeV}$) using aerogel (only in runI) and $\mathrm{C_4F_{10}}$ gas radiator with a large angular coverage from $\pm 25\,\mathrm{mrad}$ to $\pm 300\,\mathrm{mrad}$ horizontally and $\pm 250\,\mathrm{mrad}$ vertically [27]. RICH II, which is mounted behind the T3, is used for PID of charged particles with higher momenta (from $p \sim 15$ to $\geqslant 100\,\mathrm{GeV}$) using aerogel (only in runI) and $\mathrm{CF_4}$ gas radiator with a smaller angular coverage from $\pm 15\,\mathrm{mrad}$ to $\pm 120\,\mathrm{mrad}$ horizontally and $\pm 100\,\mathrm{mrad}$ vertically.

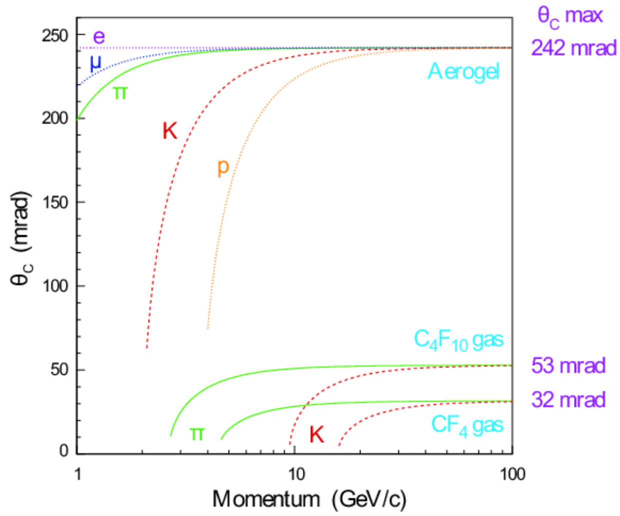

Figure 5: Cherenkov angle as a function of momentum of charged particles for the RICH radiators.

RICH uses the fact that a charged particle emits Cherenkov radiation [28], in form of photons, when travelling in a dielectric medium of refractive index n if its velocity v is larger than the speed of light in the medium ($v > \frac{c}{n}$). The angle θ_{C} between the emitted photons and the velocity of the charged particle is fixed. The relation between the angle θ_{C} and velocity v is given by

$$\cos\theta_{\mathrm{C}} = \frac{1}{n\beta},$$

where β is given as $\beta = \frac{v}{c}$. The emitted photons of wave length between $200 - 600\,\mathrm{nm}$ from the Cherenkov radiation are registered by layers of hybrid photon detectors (HPDs). The angle θ_{C} can be recontructed for each photon and extracted from the RICH system, which returns the velocity. Along with the information of the momentum of a charged particle provided by the tracking system, the mass, hence the idenfication, of the charged particle can be obtained.

In order to make the HPDs work, the magnetic field around the HPDs has to be smaller than $3\,\mathrm{mT}$. However the HPDs of the RICH I and the RICH 2 are mounted in a magneted field of $\sim 60\,\mathrm{mT}$ and $\sim 15\,\mathrm{mT}$ because of the presence of the dipole magnet. Magnetic shield needs to be implemented for both RICH I and RICH II. Requiring that the likelihood for each track with the kaon mass hypothesis be larger than that with the pion hypothesis and averaging over the momentum range 2-$100\,\mathrm{GeV}$, the kaon efficiency and pion misidentification fraction are found to be $\sim 95\%$ and $\sim 10\%$, respectively [29]. It is also found that the PID performance of the RICH system is a function of event multiplicity. A plot of θ_{C} as a function of p of charged particles for the RICH radiators is shown in Figure 5 [30].

2.2.5 Calorimeters

The calorimeter system has two main functions. It does the PID of electrons, photons and hadrons and measures their energies and positions. It can select particles with certain energies to be able to trigger different trigger lines for event reconstruction. The LHCb calorimeter system consists of a scintillator pad detector (SPD) plane in front of a preshower detector (PS), an electromagnetic calorimeter (ECAL) and a hadronic calorimeter (HCAL) [31]. For the PID of electrons, only electrons with high transverse energy can trigger L0Electron (see section 2.3). The PS and ECAL together distinguish between electrons and background of charged pions longitudinally. The SPD is used to distinguish electrons from the neutral pion background with high transverse energy.

2.2.6 Muon System

Muons are present in the final states of many CP-sensitive B decays and are thus vital to the LHCb experiment. The muon system provides fast information for the high-p_{T} muon trigger at the trigger Level-0 and muon identification for the high-level trigger (see section 2.3) and offline analysis [32]. The muon system of the LHCb detector consists of 5 muon stations M1-M5. M1 is located in front of the calorimeter system and M2-M5 are mounted behind the calorimeters. $80\,\mathrm{cm}$ thick iron absorbers are placed between M2-M5 to select muons, because muon can propagate easily through very thick iron plates, while other particles cannot. M1-M3 have a high spatial resolution in the x-direction (bending plane) and are used to define the track direction and to calculate the p_{T} of the muon candidate with a resolution of 20%. M4-M5 have a limited spatial resolution and are used for identification of penetrating particles. The muon trigger requires aligned hits in all five stations.

2.3 Trigger

Two levels of triggers are implement at the LHCb detector: the Level 0 (L0) trigger, and the High Level Trigger (HLT). When operating at an average luminosity of $2 \times 10^{32}\,\mathrm{cm}^{-2}\mathrm{s}^{-1}$, the pp collisons with interactions that can be detected by the LHCb detector are registered at a rate around $10\,\mathrm{MHz}$ [33]. The L0 and HLT triggers reduce the rate to about $2\,\mathrm{kHz}$, at which events are stored for further analysis. The trigger system reduces the data taking rate to a level where the data can be processed for the reconstruction and stored.

The L0 trigger reduces the LHC beam crossing rate of $40\,\mathrm{MHz}$ to $1\,\mathrm{MHz}$, at which the entire detector can be read out, by selecting hadrons, electrons and photon with high transverse energy ($\mathrm{E_T}$) deposit in the calorimeter system, or muons with high transverse momentum p_{T} registered in the muon stations [34]. The thresholds applied in L0 are givin in Table 3 [14].

	2011	2012
single muon p_{T}	$1.48\,\mathrm{GeV}$	$1.76\,\mathrm{GeV}$
dimuon p_{T}^2	$(1.296\,\mathrm{GeV})^2$	$(1.6\,\mathrm{GeV}^2)$
hadron $\mathrm{E_T}$	$3.5\,\mathrm{GeV}$	$3.7\,\mathrm{GeV}$
electron $\mathrm{E_T}$	$2.5\,\mathrm{GeV}$	$3\,\mathrm{GeV}$
photon $\mathrm{E_T}$	$2.5\,\mathrm{GeV}$	$3\,\mathrm{GeV}$

Table 3: L0 thresholds in 2011 and 2012.

The HLT trigger is divided into HLT1 and HLT2 two stages. The HLT utilizes a computing farm of around 16000 cores to process events and reduce the rate to about $2\,\mathrm{kHz}$. The purpose of HLT1 is to implement Level-0 confirmation using mainly information from the VELO and the tracking stations. HLT1 should reduce the rate to about $30\,\mathrm{kHz}$. The HLT2 stage uses cuts on invariant mass or on pointing of the B momentum towards the primary vertex, aiming to reduce the rate to about $2\,\mathrm{kHz}$. Two types of selections, inclusive and exclusive, are applied. Inclusive selections aim to collect decays of resonances which are useful for calibration and likely to have been produced in a B decay. Exclusive selections are specifically designed to provide the highest possible efficiency for fully-reconstructed B decays of interest, using all available information, including the mass, vertex quality and separation for the B candidate and the intermediate resonances [35].

The analysis presented in this thesis uses strategy L0Global_TIS and L0Muon_TOS at the Level 0, to reject tracks with low $\mathrm{E_T}$ or p_T. An event is classified as TOS (Trigger On Signal) if the trigger objects that are associated with the signal are sufficient to generate a postive trigger decision, while classified as TIS (Trigger Independent of Signal) if the "rest" of it is sufficient to generate a positive trigger decision, where the rest of the event is defined through an operational procedure consisting in remoing the signal and all detector hits belonging to it [36]. At the HLT2 stage several n-body ($\mathrm{n} \in \{2,3,4\}$) HLT2 topological lines are used, which triggers on B decaying to at least two charged daughters with high signal efficiency and a large background rejection factor based on a fast BDT selection [37]. The signal decay $\Lambda_\mathrm{b}^0 \to \Lambda_\mathrm{c}^+(\to \mathrm{p}^+\mathrm{K}^-\pi^+)\mathrm{D}^-(\to \mathrm{K}^+\pi^-\pi^-)\overline{\mathrm{K}}^{*0}(\to \mathrm{K}^-\pi^+)$ will be selected by Hlt2Topo2, Hlt2Topo3 and Hlt2Topo4 lines. An inclusive trigger line Hlt2IncPhi is also used, which is designed to select decays with intermediate resonance decay $\phi \to \mathrm{K}^+\mathrm{K}^-$ [38]. This line is crucial for the selection of, for example, the reference channel $\Lambda_\mathrm{b}^0 \to \Lambda_\mathrm{c}^+\mathrm{D}_\mathrm{s}^-(\to \phi(\to \mathrm{K}^+\mathrm{K}^-)\pi^-)$, where D_s^- decays into K^+, K^- and π^- via ϕ resonance.

3 Pentaquark Search

Possible hadrons with quark contents $\mathrm{qq\overline{q}\overline{q}}$ and $\mathrm{qqqq\overline{q}}$ were proposed by Gellmann [39] in 1964 along with hadrons with quark contents $\mathrm{q\overline{q}}$ and qqq, which are nowadays called mesons and baryons respectively. Quantitave descriptions of hadrons of multiquark content $\mathrm{qq\overline{q}\overline{q}}$ and $\mathrm{qqqq\overline{q}}$ and $\mathrm{q^5\overline{q}^2}$ were provided by Jaffe [40] in 1976 and Strottman [41] in 1979. Several papers have been published in the 2000s, claiming the existence of the pentaquark Θ^+ with quark content $\mathrm{\overline{s}uudd}$, but the results remained unconfirmed [42]. The first convincing evidence for the existence of pentaquarks $\mathrm{P_c(4380)^+}$ and $\mathrm{P_c(4450)^+}$ was founded in 2015 at the LHCb experiment with quark content $\mathrm{c\overline{c}uud}$, by studying the decay channel $\Lambda_\mathrm{b}^0 \to \mathrm{J}/\psi\mathrm{p}^+\mathrm{K}^-$ and resonances in the $\mathrm{J}/\psi\mathrm{p}^+$ subsystem. An amplitude analysis was conducted to test if interferring $\Lambda^*(\mathrm{p}^+\mathrm{K}^-)$ resonances were responsible for the peaking structure seen in the $m_{\mathrm{J}/\psi\mathrm{p}^+}$ distribution and if the inclusion of $\mathrm{P_c^+} \to \mathrm{J}/\psi\mathrm{p}^+$ decays in the amplitude model could reproduce the structure. It was shown that adequate descriptions of the dat are unattainable with only $\mathrm{p}^+\mathrm{K}^-$ resonances in the amplitude model and it was necessary to include two $\mathrm{J}/\psi\mathrm{p}^+$ resonances, with each having 9σ significance. One has a mass of

$4449.9 \pm 1.7 \pm 2.2\,\mathrm{MeV}$ and a width of $39 \pm 5 \pm 16\,\mathrm{MeV}$, while the second is broader, with a mass of $4380 \pm 8 \pm 29\,\mathrm{MeV}$ and a width of $205 \pm 18 \pm 87\,\mathrm{MeV}$.

3.1 The Search for Neutral Isospin Partners of $\mathrm{P_c(4380)^+}$ and $\mathrm{P_c(4450)^+}$

The search for pentaquark candidates with quark content $\mathrm{c\bar{c}udd}$, neutral isospin partners of the observed pentaquarks $\mathrm{P_c(4380)^+}$ and $\mathrm{P_c(4450)^+}$ would be an interesting task, since it might provide experimental evidence for the theoretical development of isospin symmetry in pentaquarks regime. An ideal decay channel for the search for $\mathrm{c\bar{c}udd}$ pentaquark candidates would be $\Lambda_\mathrm{b}^0 \to \mathrm{J}/\psi\mathrm{n}$, since the signal yields of this decay are expected very high. However, it is not possible to reconstruct the decay, because the neutron, which is electrically neutral, cannot be reconstructed by the LHCb detector. The decay $\Lambda_\mathrm{b}^0 \to \Lambda_\mathrm{c}^+\mathrm{D}^-\overline{\mathrm{K}}^{*0}$ provides an alternative, since the pentaquark candidates $\mathrm{c\bar{c}udd}$ could be found within resonances of the $\Lambda_\mathrm{c}^+\mathrm{D}^-$ subsystem.

The decay $\Lambda_\mathrm{b}^0 \to \Lambda_\mathrm{c}^+\mathrm{D}^-\overline{\mathrm{K}}^{*0}$, which has not yet benn observed before, has a weak decay $\mathrm{b} \to \mathrm{c}$ and a creation of a $\mathrm{d\bar{d}}$ pair via a strong interaction. This decay process is relatively simple. However, it has eight final-state particles, which are proton, kaons and pions, making it difficult to study due to more potential sources of particle misidentification, various unwanted resonances from combinations of different tracks, multiple combinatorial backgrounds and backgrounds of feed-down decays. The observation of this decay channel would lead to a branching fraction measurement with reference to the normalization channel $\Lambda_\mathrm{b}^0 \to \Lambda_\mathrm{c}^+\mathrm{D_s^-}$. With a well measured branching fraction measurement $\frac{\mathscr{B}\left(\Lambda_\mathrm{b}^0 \to \Lambda_\mathrm{c}^+\mathrm{D}^-\overline{\mathrm{K}}^{*0}\right)}{\mathscr{B}\left(\Lambda_\mathrm{b}^0 \to \Lambda_\mathrm{c}^+\mathrm{D_s^-}\right)}$, an amplitude analysis of the resonances in the $\Lambda_\mathrm{c}^+\mathrm{D}^-$ subsystem could be conducted for the search for the pentaquark candidates. Since the $\Lambda_\mathrm{c}^+\mathrm{D}^-$ subsystem is expected to have non-zero spin, its multiple helicity amplitudes must be considered and are expected to be sensitive to the branching fraction [43, 44, 45]. Also efficiencies of trigger, reconstruction, stripping, acceptance and the selection of Λ_c^0 can be cancelled out in branching fraction measurement, which will improve the precision of the efficiency measurement. Feynman diagrams of the decays of the signal channel and reference channel are given in Figure 6.

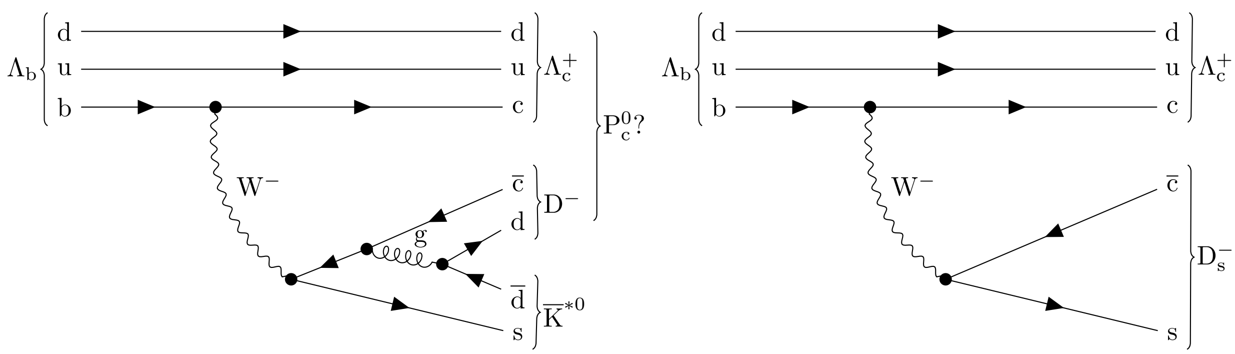

Figure 6: Feynman diagrams of the decays $\Lambda_\mathrm{b}^0 \to \Lambda_\mathrm{c}^+\mathrm{D}^-\overline{\mathrm{K}}^{*0}$ (left) and $\Lambda_\mathrm{b}^0 \to \Lambda_\mathrm{c}^+\mathrm{D_s^-}$ (rigiht).

4 First Observation of the Decay $\Lambda_b^0 \to \Lambda_c^+ D^- \overline{K}^{*0}$ using a Cut-based Selection

The stripping lines StrippingLb2LcDKstBeauty2CharmLine are applied to the data passing the trigger lines described in section 2.3. The stripping lines use a series of relatively loose one-dimensional cuts to select candidate events of the decay $\Lambda_b^0 \to \Lambda_c^+ D^- \overline{K}^{*0}$. Details of the stripping lines are described in section 4.1. A cut-based offline selection is conducted to the data passing the stripping lines, in order to explore the data and establish a clean signal decay. The strategy is to get convincing signal peaks for the three intermediate particles Λ_c^+, D^- and $\overline{K}^{*0}$, using some kinematic (e.g. p_T) and PID (e.g. ProbNN) cuts on the final-state particles and cuts to control decay vertex reconstruction quality (e.g. ENDVERTEX_CHI2NDOF) of the intermediate particles. With clear signal peaks of the three intermediate particles, cuts are applied to control decay vertex reconstruction quality and detector acceptance (η, pseudorapidity) of Λ_b^0. A convincing Λ_b^0 peak is established with all these cuts applied. Details are presented in section 4.2. To control possible misidentification, some veto cuts are applied after the cut-based selection, to reject undesirable resonance peaks, which are given in section 4.3. Some multi-dimensional mass fits are then applied to the decaying particles, in order to estimate various background compositions and signal yields. The fit procedures and the results are illustrated in section 4.4. A brief efficiency study is presented in section 4.5. The total stripping, reconstruction, acceptance and trigger efficiency and the efficiency of the offline non-PID cuts are estimated using the generated and fully detector simulated MC data. The efficieny of the PID cuts is obtained using the PIDCalib package [46]. The result of the efficiency corrected signal yields is given in section 4.6. A short summary given in section 4.6 ends the cut-based selection.

4.1 Stripping

Stripping lines StrippingLb2LcDKstBeauty2CharmLine of versions 21r1(21) are applied to 2011(2012) data [47, 48]. The cuts applied to the tracks in the stipping lines are listed in Table 4. The topology of the decay $\Lambda_b^0 \to \Lambda_c^+ D^- \overline{K}^{*0}$ is illustrated in Figure 7.

The selection strategy used in the stripping lines is descrbed in the following. The selection for D^- is conducted at first, starting with its final-state particles. Some very loose cuts on the kinematic variables PT and P, to reject tracks with low (transverse) momentum, which are not desirable because they are unlikely to form the decaying particle in the reconstruction and the PID uncertainty for those tracks are higher (see section 2.2.4). The variables TRGHP (probability that a reconstructed track is a ghost track) and $\mathrm{TRCHI2DOF}$ (χ^2/ndf of a reconstructed track) control the quality of the reconstructed tracks. $\mathrm{MIPCHI2DV(PRIMARY)} > 4$ (χ^2/ndf of the minimal impact parameter of a track to a series of vertices[3]), where the impact parameter is the closest distance between the trajectory of a particle projected back to the related primary vertex and the primary vertex (see Figure 7) will help reject prompt particles.

[3] A series of primary vertex candidates are reconstructed in the VELO.

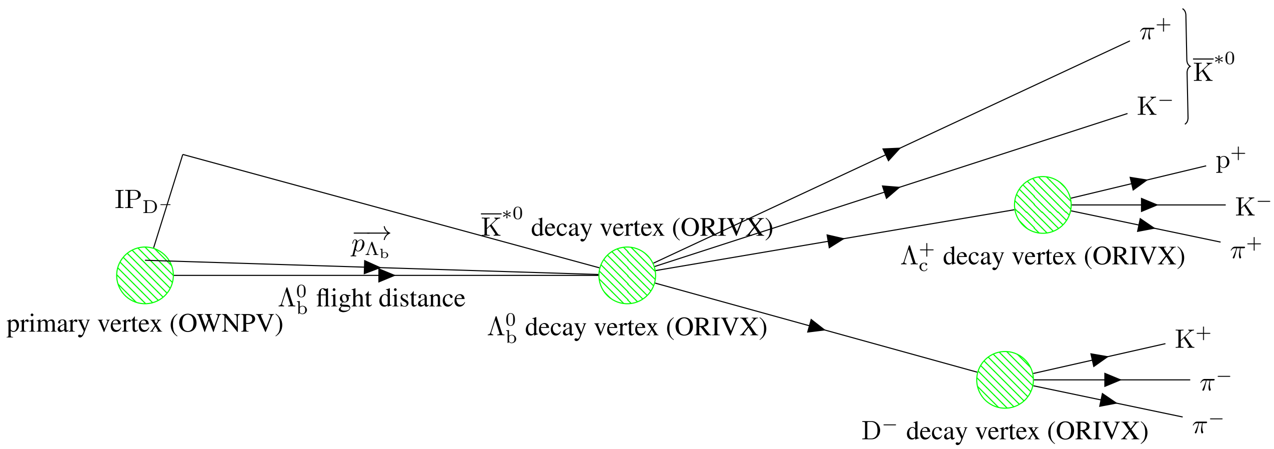

Figure 7: Topology of the decay $\Lambda_b^0 \to \Lambda_c^+ \mathrm{D}^- \overline{\mathrm{K}}^{*0}$.

The PIDX (X a particle) variable, also known as delta-log-likelihood (DLL), is define as

$$\mathrm{PIDX} \coloneqq \Delta \log \mathcal{L}_{\mathrm{X}-\pi} = \log \frac{\mathcal{L}_{\mathrm{X}}}{\mathcal{L}_{\pi}}, \tag{2}$$

where $\mathcal{L}$ is the log-likelihood for the given hypothesis. The final-state particles are required to be $\mathrm{PIDp} > -10$ for a proton, $\mathrm{PIDK} > -10$ for a kaon and $\mathrm{PIDK} < 20$ for a pion. Then to select D^- candidates, $\mathrm{ASUM(PT)}$, the sum of the transverse momenta of the final-state particles, is required to be larger than $1800\,\mathrm{MeV}$, so that the final-states particles have enough energy to be reconstructed as D^-. The variable $\mathrm{BPVVDCHI2}$ (χ^2-separation from the primary vertex) selects tracks that are less likely to come from the primary vertex. $\mathrm{ACUTDOCA} < 0.5\,\mathrm{mm}$ (distance of closest approach) selects daughter tracks, two of which are closer than $0.5\,\mathrm{mm}$. This limits the decay topology of D^-, requiring that the final-state particles are not separated far away from each other. $\mathrm{VFASPF(VCHI2/VDOF)} < 10$ (χ^2/ndf of recontructed decay vertex) controls the quality of the reconstructed decay vertex of D^-. The variable $\mathrm{BPVDIRA}$ (direction angle with reference to the primary vertex) is the cosine of the angle between the momentum of a particle and the direction from the best primary vertex to the decay vertex. $\mathrm{BPVDIRA} > 0$ selects downstream tracks[4]. The function $\mathrm{AHASCHILD}$ requires that at one track decaying from the mother particle satisfy the conditions in the function. $\mathrm{AWM(K+, pi-, pi-)}$, the invariant mass of K^+, π^- and π^- is set within the range $(1769.62\,\mathrm{MeV}, 2068.49\,\mathrm{MeV})$[5].

The selection of Λ_c^+ is almost the same. The only difference is that $\mathrm{ADMASS(Lambda\_c+)} < 100\,\mathrm{MeV}$ requires the reconstructed Λ_c^+ mass within $100\,\mathrm{MeV}$ around its PDG mass $2286.46 \pm 0.14\,\mathrm{MeV}$. The selection of $\overline{\mathrm{K}}^{*0}$ is basically the same, despite several differences. It needs to be mentioned that there is no PID cut on its daughter tracks.

The selection of Λ_b^0 involves more variables. $\mathrm{MIPDV(PRIMARY)} > 0.1\,\mathrm{mm}$ (minimal impact parameter with

[4]Downstream is define as positve z-direction, see Figure 3

[5]The D^- PDG mass is $1869.65 \pm 0.05\,\mathrm{MeV}$.

Particle	Requirements
p^+, $K^\pm$, $\pi^\pm$ (from Λ_c^+/D^-)	$\mathrm{PT} > 100\,\mathrm{MeV}$ and $\mathrm{P} > 1000\,\mathrm{MeV}$ $\mathrm{MIPCHI2DV(PRIMARY)} > 4$ $\mathrm{TRGHP} < 0.4$ $\mathrm{TRCHI2DOF} < 3$ PIDp/K> -10 for p^+ and $K^\pm$, PIDK< 20 for $\pi^\pm$
Λ_c^+/D^-	$\mathrm{ASUM(PT)} > 1800\,\mathrm{MeV}$ ACUTDOCA$< 0.5\,\mathrm{mm}$ $\mathrm{VFASPF(VCHI2/VDOF)} < 10$ AHASCHILD($\mathrm{PT} > 500\,\mathrm{MeV}$ and $\mathrm{P} > 5000\,\mathrm{MeV}$ and ($\mathrm{TRCHI2DOF} < 2.5$ or $\mathrm{BPVVDCHI2} > 1000$)) $\mathrm{BPVVDCHI2} > 36$ $\mathrm{BPVDIRA} > 0$ $1769.62\,\mathrm{MeV} < \mathrm{AWM(K+, pi-, pi-)} < 2068.49\,\mathrm{MeV}$ ADMASS(Lambda_c+ $< 100\,\mathrm{MeV}$
K^-, π^+ (from $\overline{K}^{*0}$)	$\mathrm{PT} > 100\,\mathrm{MeV}$ and $\mathrm{P} > 2000\,\mathrm{MeV}$ $\mathrm{TRCHI2DOF} < 3$ $\mathrm{MIPCHI2DV(PRIMARY)} > 4$ $\mathrm{TRGHP} < 0.4$
$\overline{K}^{*0}$	$\mathrm{ASUM(PT)} > 1000\,\mathrm{MeV}$ $\mathrm{AM} < 5.2\,\mathrm{GeV}$ ACUTDOCA$<\ 0.5\,\mathrm{mm}$ $\mathrm{VFASPF(VCHI2/VDOF)} < 16$ AHASCHILD($\mathrm{PT} > 500\,\mathrm{MeV}$ and $\mathrm{P} > 5000\,\mathrm{MeV}$ and ($\mathrm{TRCHI2DOF} < 2.5$ or $\mathrm{BPVVDCHI2} > 1000$)) $\mathrm{BPVVDCHI2} > 16$ $\mathrm{BPVDIRA} > 0$
Λ_b^0	$\mathrm{ASUM(SUMTREE(PT))} > 5000\,\mathrm{MeV}$ $\mathrm{VFASPF(VCHI2/VDOF)} < 10$ INTREE($\mathrm{PT} > 1700\,\mathrm{MeV}$ and $\mathrm{P} > 10000\,\mathrm{MeV}$ and $\mathrm{MIPCHI2DV(PRIMARY)} > 16$ and $\mathrm{MIPDV(PRIMARY)} > 0.1\,\mathrm{mm}$) NINTREE($\mathrm{PT} > 500\,\mathrm{MeV}$ and $\mathrm{PT} > 5000\,\mathrm{MeV}$ and ($\mathrm{TRCHI2DOF} < 2.5$ or $\mathrm{BPVVDCHI2} > 1000$)) > 1 $\mathrm{BPVLTIME()} > 0.2\,\mathrm{ps}$ $\mathrm{BPVIPCHI2()} < 25$ $\mathrm{BPVDIRA} > 0.999$ $5200\,\mathrm{MeV} < \mathrm{AM} < 7000\,\mathrm{MeV}$

Table 4: Cuts in the stripping lines.

reference to a set of reconstructed primary vertices) rejects tracks with low impact parameter, which is more likely to come from the primary vertex. The NINTREE function returns the number of tracks that satisfy its requirements. The variable $\mathrm{BPVLTIME()}$ is the lifetime of a particle with reference to the related primary vertex. $\mathrm{BPVLTIME()} > 0.2\,\mathrm{ps}$ selects Λ_b^0 candidate with a relatively long lifetime, since Λ_b^0 has quite long lifetime due to its high mass and broad decay modes. $\mathrm{BPVIPCHI2()}$ (χ^2 of impact parameter) is set smaller than 25, which selects Λ_b^0 that is likely to come from the primary vertex. For the same purpose $\mathrm{BPVDIRA} > 0.999$ require that the momentum of a Λ_b^0 candidate be almost identical as the direction between its generation and decay vertices. At last a loose cut on the invariant mass of Λ_c^+, D^- and $\overline{K}^{*0}$ is applied.

4.2 Cut-based Selection

The cuts applied in the stripping lines (see section 4.1) are very loose and no Λ_b^0 peak can be seen in the data. Some tighter cuts are applied to explore the data. After adjusting the cuts based on the knowledge of the topology of the signal decay and informed by other analyses of similar decay channels, e.g. [49], clear Λ_c^+, D^-, $\overline{K}^{*0}$ and Λ_b^0 peaks are seen. The cuts are then retuned on the fully detector simulated Monte-Carlo data, to maintain clear signal peaks and get an adequate number of event for the mass fits The cuts used to get Λ_c^+, D^- and $\overline{K}^{*0}$ signal peaks are listed in Table 5.

cuts	Λ_c^+	p^+	K^-	π^+	D^-	K^+	π^-	π^-	$\overline{K}^{0*}$	K^-	π^+
p_T /MeV	/	> 700	> 400	> 150	/	> 400	> 150	> 150	/	> 400	> 150
PIDK	/	/	/	/	/	/	/	/	/	> 3	< 3
prod_ProbNN	/	> 0.03	> 0.05	> 0.05	/	> 0.05	> 0.05	> 0.05	/	> 0.05	> 0.05
$\mathrm{ENDVERTEX}_{\chi^2/\mathrm{ndf}}$	< 4	/	/	/	< 4	/	/	/	< 4	/	/
η	/	/	/	/	/	/	/	/	/	< 5	< 5

Table 5: Applied cuts to get Λ_c^+, D^- and $\overline{K}^{*0}$ signals.

Some variables need to be briefly explained. The variable ProbNN is the reponse of a normalized artificial neural network (named PIDANN), using all PID information provided by the detector (RICH1, RICH2, the muon station, ECAL and HCAL) [50]. The PIDAAN algorithm is tuned on simulated signal and background samples. The variable prod_ProbNN is defined for various particles as [49]

$$\begin{aligned}
\mathrm{prod_ProbNN_p_K(p)} &= \mathrm{ProbNN_p(p)}(1 - \mathrm{ProbNN_K(p)}),\\
\mathrm{prod_ProbNN_p_K(p)} &= \mathrm{ProbNN_p(p)}(1 - \mathrm{ProbNN_K(p)}),\\
\mathrm{prod_ProbNN_}\pi\mathrm{_K}(\pi) &= \mathrm{ProbNN_}\pi(\pi)(1 - \mathrm{ProbNN_K}(\pi)),\\
\mathrm{prod_ProbNN_K_}\pi\mathrm{(K)} &= \mathrm{ProbNN_K(K)}(1 - \mathrm{ProbNN_}\pi\mathrm{(K)}).
\end{aligned}$$

Cuts on the first two definitions help select proton-like and un-kaon/pion-like particles; a cut on the third helps select kaon-like and un-pion-like particles; a cut on the fourth helps select pion-like and un-kaon-like particles. A cut on prod_ProbNN is more effective than an one-dimensional cut on ProbNN or DLL, seen in the data. $\mathrm{ENDVERTEX}_{\chi^2/\mathrm{ndf}}$ is the same as the variable $\mathrm{VFASPF(VCHI2/VDOF)}$ mentioned in section 4.1. η, the pseudorapidity, selects events that are inside the LHCb detector acceptance $1.6 < \eta < 4.9$ (see section 2.2.1). p_T thresholds are set higher for all the eight final-state tracks. The minimal values are tuned on MC data, because with these cuts tracks with relatively low p_T can be rejected while the signal efficiency stays relatively high. Seen from the MC data, pions have relatively low transverse momentum, compared to proton and kaons. The $\mathrm{ENDVERTEX}_{\chi^2/\mathrm{ndf}}$ cuts are set relatively strict, to select events with high quality of decay vertex reconstruction. The mass spectra of Λ_c^+, D^- and $\overline{K}^{*0}$ are shown in Figure 8.

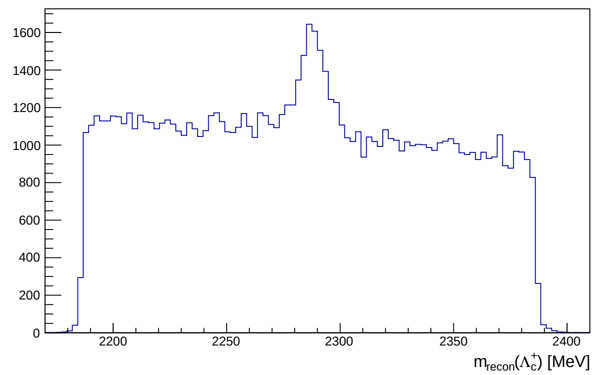

(a) Λ_c^+ peak.

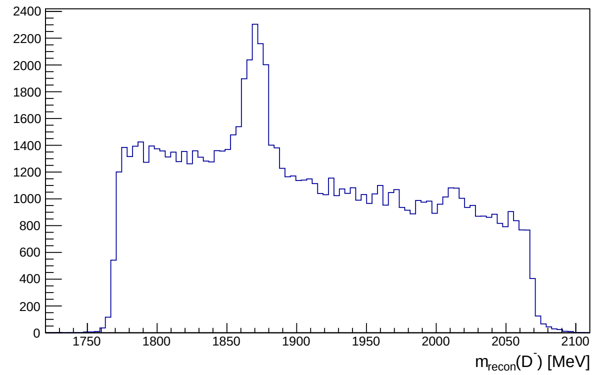

(b) D^- peak.

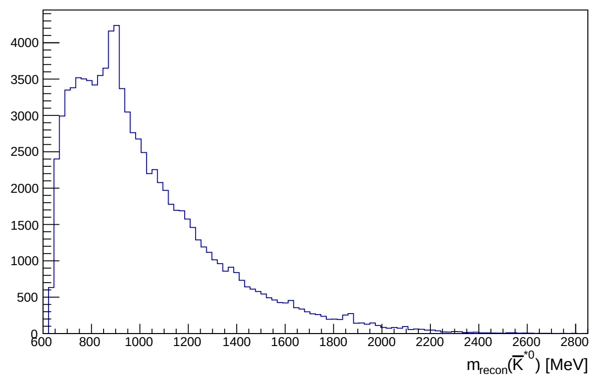

(c) $\overline{K}^{*0}$ peak.

Figure 8: Distribution of reconstructed Λ_c^+, D^- and $\overline{K}^{*0}$ masses with cuts in Table 5 applied.

With clean peaks of Λ_c^+, D^- and $\overline{K}^{*0}$, the Λ_b^0 signal peak can be obtained by applying mass cuts on the three intemediate particles. For Λ_c^+ and D^- the mass cuts are chosen to as narrow as possible while including enough amount of sideband, so that background shapes can be estimated correctly in the mass fits. The range for $\overline{K}^{*0}$ is set much wider, due to the large extension of the distribution of the resonance and also for the fits to be able to get information on the background. The upper range is set to $1000\,\mathrm{MeV}$ to reject potential feed-down from $\overline{K}^*$ with higher masses, as almost all of them decay into K^{*0} and γ or π^0 [51]. An acceptance cut is applied, selecting Λ_b^0 candidates that are reconstructed relatively far away from the boundary of the detector. A decay vertex cut is also applied on Λ_b, to require strictly that Λ_c^+, D^- and $\overline{K}^{*0}$ decay from Λ_b. The applied cuts are listed in Table 6.

To get better resolution of the Λ_b^0 spectrum, a decay tree fitter (DTF) is applied. The DTF is applied to improve the

cuts	Λ_c^+	D^-	$\overline{K}^{0*}$	Λ_b
M/MeV	(2256,2316)	(1829,1909)	(700,1000)	/
η	/	/	/	(2.2,4.5)
$\mathrm{ENDVERTEX}_{\chi^2/\mathrm{ndf}}$	/	/	/	< 4

Table 6: Applied Cuts on Λ_c^+, D^-, $\overline{K}^{0*}$ and Λ_b^0.

disadvantage of the "leaf-by-leaf" fitting, of which constraints that are upstream of a decay vertex do not contribute to the knowledge of the parameters of the vertex [52]. In this analysis the constraints are mass constraints on the final-state particles of Λ_c^+ and D^- and Λ_b^0 trajectory pointing to the pp colliding point. The Λ_b^0 DTF mass[6] and the Λ_b^0 mass are shown in Figure 9, where it can be clearly seen that with DTF the Λ_b^0 mass resolution is enhanced. The trigger and stripping lines will include some partially reconstructed decays while select the signal decay. Possible partially reconstructed decays are expected to be:

$$\Lambda_b^0 \rightarrow \Lambda_c^+[D^-\pi^0]_{D^{*-}}\overline{K}^{*0},$$

$$\Lambda_b^0 \rightarrow \Lambda_c^+[D^-\gamma]_{D^{*-}}\overline{K}^{*0},$$

$$\Lambda_b^0 \rightarrow [\Lambda_c^+\pi^0]_{\Sigma_c^+}D^-\overline{K}^{*0},$$

which are assumed to constitute the small peak around $5485\,\mathrm{MeV}$.

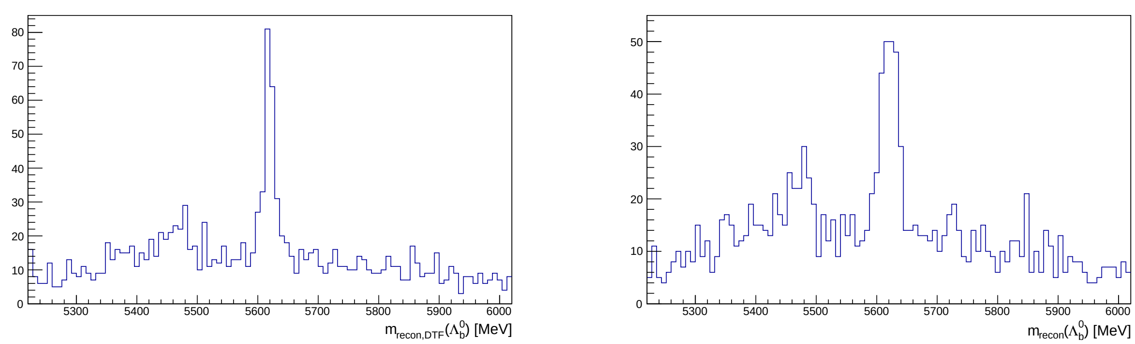

Figure 9: Left: Distribution of reconstructed Λ_b mass with the DTF applied. Right: Distribution of reconstructed Λ_b mass.

A mass cut of $30\,\mathrm{MeV}$ around the Λ_b^0 PDG mass is applied while dropping the mass cut on one of the three intermediate particles is dropped (mass cuts on the other two maintained), to exmaine if the selected Λ_c^+, D^- and $\overline{K}^{0*}$ are indeed coming from Λ_b^0. Three mass spectra returned from the procedure are illustrated in Figure 10. Clear signal peaks suggest that the selected Λ_c^+, D^- and $\overline{K}^{0*}$ do come from Λ_b^0.

[6] A series of Λ_b^0 DTF masses are returned from the fit procedure. The first one is chosen because it has the best quality.

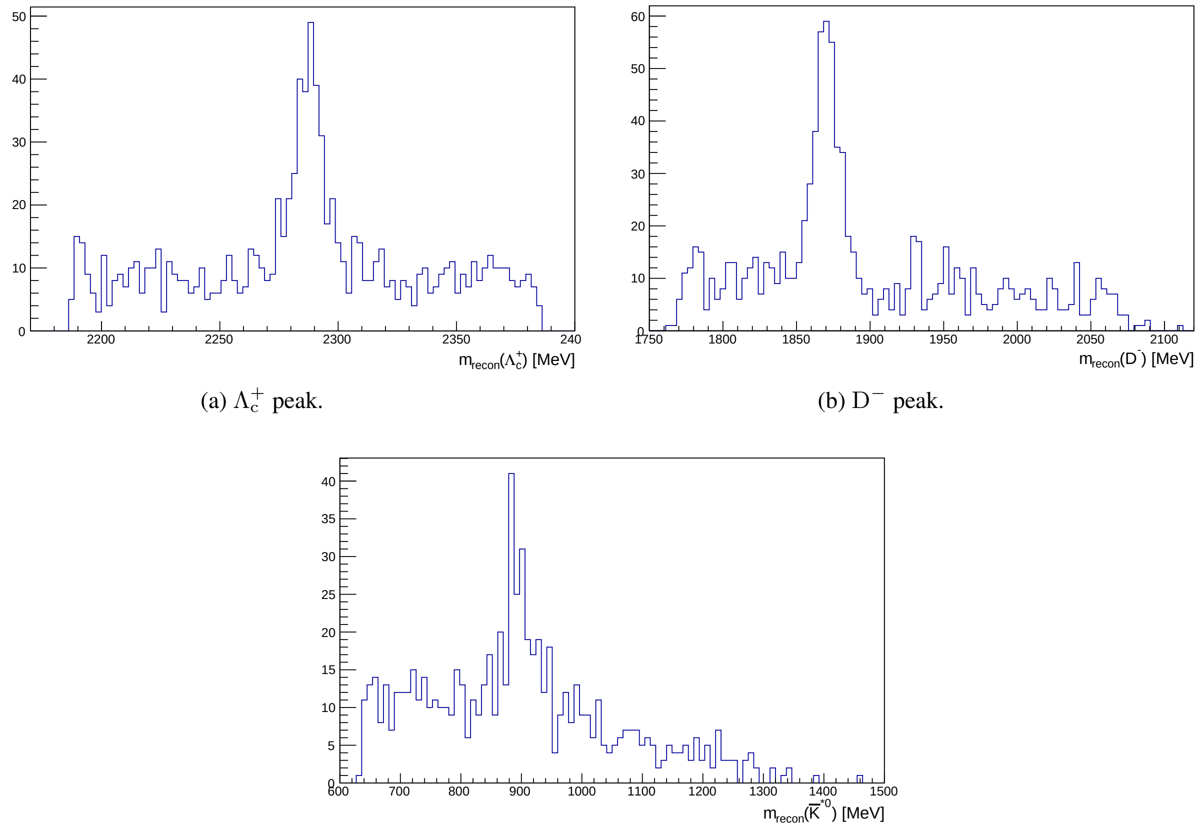

(a) Λ_c^+ peak.

(b) D^- peak.

(c) $\overline{K}^{*0}$ peak.

Figure 10: Check for distributions of reconstructed Λ_c^+, D^- and $\overline{K}^{*0}$ masses with cuts in Table 5, Table 6 and a mass cut $5590\,\mathrm{MeV} < m_{\mathrm{recon,DTF}(\Lambda_b)} < 5650\,\mathrm{MeV}$ applied. To show each individual spectrum, the mass cut on that particle is dropped.

4.3 Misidentification Control

To control misidenfication backgrounds after the cut-based selection, the method describe in [49] is used, with no mass cut applied[7]. It makes use of the fact, that swapping the mass hypotheses of a single particle in the decay chain can be fully described by the invariant mass of the combined system with original mass hypothesis M and a single particle momentum asymmetry β [53]. Resonances consisting of a misidentified particle will emerge as a band in the 2D plot of M and β.

As an exmaple, the misidentification check for the invariant mass combination M_{128} is shown in Figure 11, where the emumeration for the final-state particle is 1, 2, 3, 4, 5, 6, 7 and 8 for p^+, K^-(from Λ_c^+), π^+(from Λ_c^+), K^+, π_1^-, π_2^-, K^-(from $\overline{K}^{*0}$) and π^+(from $\overline{K}^{*0}$). A obvious band appears in the region $(-0.4, 0.8) \times (2276\,\mathrm{MeV}, 2296\,\mathrm{MeV})$, which corresponds to the situation where the p^+, K^-(from Λ_c^+) and π^+(from $\overline{K}^{*0}$) form a Λ_c^+. This region is cut out

[7]The mass cuts applied, the event number is too low that no clear structure can be senn, if there exists some misidentification background.

to reject the unwanted resonance. Some other misidentification backgrounds are also vetoed. Attention needs to be paid to the decay $\Lambda_b^0 \rightarrow [\Lambda_c^+\pi^+]_{\Sigma_c^{++}}D^-K^-$, which could be reconstructed as the signal decay, where the π^+ from $\overline{K}^{*0}$ and the Λ_c^+ decay from a Σ_c^{++}. However, by checking the 2D plot of M_{1238} against β_{1238} shown in Figure 12, no clear structure is seen. It need to be mentioned that due to the vast possible combinations of the eight final-state tracks, the misidentification check done here cannot be absolutely thorough and could be improved if time allowed. All applied cuts are listed in Table 7.

4.4 Mass Fits

Clear signal peaks are obtained from the cut-based selection. The signal yields can be estimated by just applying a 1D fit to the Λ_b^0 mass spectrum. The problem with the 1D fit is that it cannot distinguish decays, for example $\Lambda_b \rightarrow \Lambda_c^+K^+\pi^-\pi^-\overline{K}^{*0}$, from the signal decay $\Lambda_b^0 \rightarrow \Lambda_c^+D^-\overline{K}^{*0}$. Contributions of different backgrounds, however, can be estimated by implementing multi-dimensional mass fits. Three different fit procedures are applied to the data passing all the cuts listed in Table 7. They are described in details in the following.

4.4.1 3D Mass Fits

3D mass fits to Λ_b^0[8], Λ_c^+ and D^- spectra are conducted, mainly to estimate the backgrounds of the decays $\Lambda_b^0 \rightarrow \Lambda_c^+[K^+\pi^-\pi^-]\overline{K}^{*0}$ and $\Lambda_b^0 \rightarrow [p^+K^-\pi^+]D^-\overline{K}^{*0}$[9], where the system $[K^+\pi^-\pi^-]([p^+K^-\pi^+])$ does not form

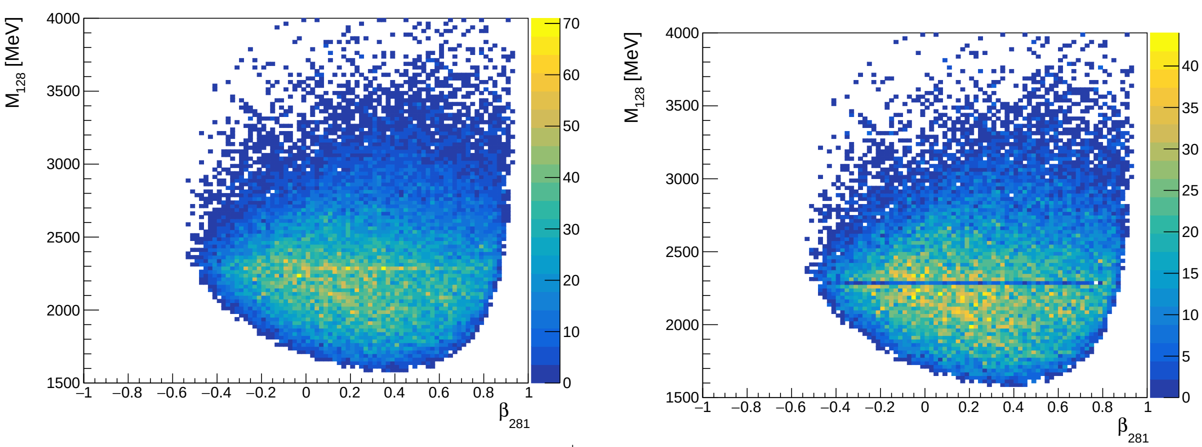

(a) Mass against momentum asymmetry of the system p^+, $K^-(\Lambda_c^+)$ and $\pi^+(\overline{K}^{*0})$ before veto cut. The band suggests that there is misidentified Λ_c^+.

(b) Mass against momentum asymmetry of the system p^+, $K^-(\Lambda_c^+)$ and $\pi^+(\overline{K}^{*0})$ after veto cut.

Figure 11: Misidentification check for the 3-body system p^+, $K^-(\Lambda_c^+)$ and $\pi^+(\overline{K}^{*0})$.

[8] Λ_b^0 DTF mass is used for all mass fits in this thesis.

[9] The decay $\Lambda_b^0 \rightarrow [K^+\pi^-\pi^-][K^+\pi^-\pi^-]\overline{K}^{*0}$ is ignored because of at least double Cabbibo suppression.

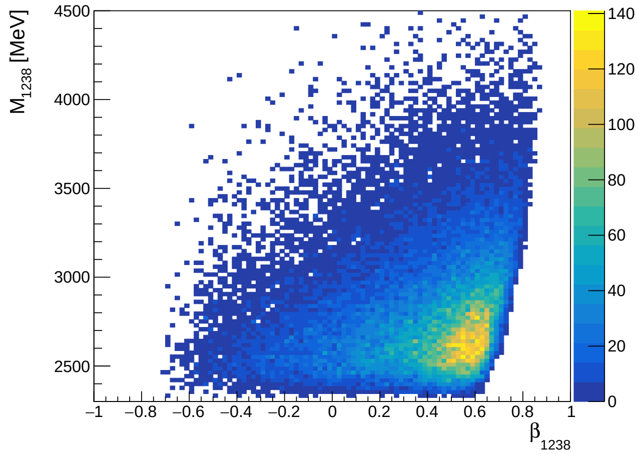

Figure 12: Check for potential resonance of Σ_c^{++}. The invariant mass of the system of p^+, K^- (Λ_c^+), π^+ (Λ_c^+) and π^+ $\left(\overline{K}^{*0}\right)$ is plotted against its momentum asymmetry. No clear structure is seen.

type	variable	range/cut
kinematics	p_{T,p^+}	$> 700\,\mathrm{MeV}$
	$p_{T,K^\pm}$	$> 400\,\mathrm{MeV}$
	$p_{T,\pi^\pm}$	$> 150\,\mathrm{MeV}$
PID	$\mathrm{PIDK}_{K^-(\overline{K}^{*0})}$	> 3
	$\mathrm{PIDK}_{\pi^+(\overline{K}^{*0})}$	< 3
	prod_ProbNN_p_K(p)	> 0.03
	prod_ProbNN_p_π(p)	> 0.03
	prod_ProbNN_K_π(K)	> 0.05
	prod_ProbNN_π_K(π)	> 0.05
reconstruction	$\mathrm{ENDVERTEX}_{\chi^2/\mathrm{ndf},\Lambda_c^+,D^-,\overline{K}^{0*},\Lambda_b^0}$	< 4
acceptance	$\eta_{K^-(\overline{K}^{*0}),\pi^+(\overline{K}^{*0})}$	< 5
	$\eta_{\Lambda_b^0}$	$\in (2.2, 4, 5)$
veto	(β_{817}, M_{178})	$\notin (0.5, 0.9) \times (2276\,\mathrm{MeV}, 2296\,\mathrm{MeV})$
	(β_{281}, M_{128})	$\notin (-0.4, 0.8) \times (2276\,\mathrm{MeV}, 2296\,\mathrm{MeV})$
	(β_{713}, M_{137})	$\notin (0.05, 0.75) \times (2276\,\mathrm{MeV}, 2296\,\mathrm{MeV})$
	(β_{24}, M_{24})	$\notin (-0.3, 0.3) \times (1010\,\mathrm{MeV}, 1030\,\mathrm{MeV})$
	(β_{28}, M_{28})	$\notin (-0.8, 0.3) \times (880\,\mathrm{MeV}, 910\,\mathrm{MeV})$
	(β_{37}, M_{37})	$\notin (-0.4, 0.7) \times (880\,\mathrm{MeV}, 910\,\mathrm{MeV})$
	(β_{47}, M_{47})	$\notin (-0.4, 0.3) \times (1010\,\mathrm{MeV}, 1030\,\mathrm{MeV})$
mass	$m_{\Lambda_c^+}$	$\in (2256\,\mathrm{MeV}, 2316\,\mathrm{MeV})$
	m_{D^-}	$\in (1829\,\mathrm{MeV}, 1909\,\mathrm{MeV})$
	$m_{\overline{K}^{*0}}$	$\in (700\,\mathrm{MeV}, 1000\,\mathrm{MeV})$

Table 7: All applied cuts on Λ_c^+, D^-, $\overline{K}^{0*}$ and Λ_b^0 in the cut-based selection.

a resonance in the $\mathrm{D}^-(\Lambda_c^+)$ mass range, but is still included in the DTF for the reconstruction of Λ_b^0. In the 3D mass fits, these two contributions will be flat in D^- or Λ_c^+ spectra respectively, but peaking in the other two dimensions.

Since the fits do not involve $\overline{\mathrm{K}}^{*0}$, the backgrounds of the partially reconstructed decays (see section 4.2) can be estimated with relatively few fit parameters. The simulated MC data from the RapidSim package is used to fit the partially reconstructed peak. Compared to the fully detector simulated MC data, the RapidSim package provides an excellent solution for the simulation of the kinematic properties of the decay of interest with very high speed and consistence [54]. The simulated data using RapidSim is assumed adequate for the estimation for the backgrounds of the partially reconstructed decays using kernel density estimation [55] embedded in the RooFit package [56]. The simulation contains PID information for the final-state particles and the LHCb smearing is applied. The center-of-mass colliding energies are different in 2011 ($\sqrt{s} = 7\,\mathrm{TeV}$) and in 2012 ($\sqrt{s} = 8\,\mathrm{TeV}$). It is assumed that the kinematics of the partially reconstructed decays are not significantly different in the two years. For the simulation it is chosen $\sqrt{s} = 8\,\mathrm{TeV}$. The numbers of events generated from the simulation for the decays $\Lambda_b^0 \to \Lambda_c^+[\mathrm{D}^-\pi^0]_{\mathrm{D}^{*-}}\overline{\mathrm{K}}^{*0}$ and $\Lambda_b^0 \to \Lambda_c^+[\mathrm{D}^-\gamma]_{\mathrm{D}^{*-}}\overline{\mathrm{K}}^{*0}$ are set the same to their relative branching ratio $\frac{\Gamma_{\mathrm{D}^{*-}\to\mathrm{D}^-\pi^0}}{\Gamma_{\mathrm{D}^{*-}\to\mathrm{D}^-\gamma}} = \frac{30.7\%}{1.6\%}$, according to PDG [51], and merged together. The spectra of The simulated partially reconstructed decays are shown together with the Λ_b^0 DTF mass in Figure 13.

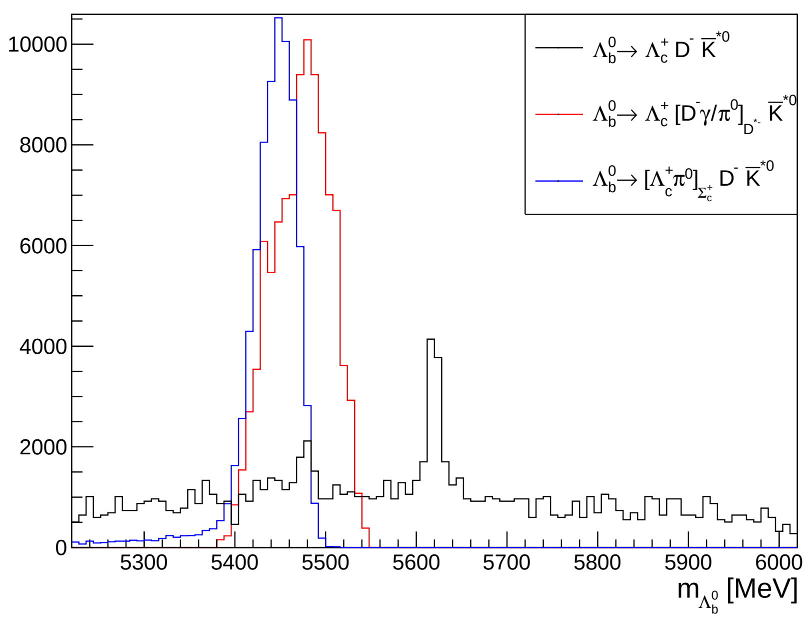

Figure 13: The simulated partially reconstructed decays plotted with the signal decay, normalized to 100000.

The shapes of Λ_b^0, Λ_c^+ and D^- signals are retrieved from the fully detector simulated MC data[10], with the same cuts listed in Table 7 applied. MC simulations are performed using PYTHIA [57] with the specific tuning given in

[10] The 2011 and 2012 datasets are merged together.

[58], and the LHCb detector description based on GEANT4 [59, 60], described in [61]. Decays of B hadrons are based on EVTGEN [62]. The Λ_b^0 signal shape is modeled by the sum of two Crystall Ball functions (a double Crystall Ball function), which takes the form:

$$f_\mathrm{DCB}\left(m;\mu,\sigma,\alpha,n,r_\mathrm{CB}\right) \coloneqq r_\mathrm{CB}\cdot f_\mathrm{CB}\left(m;\mu,\sigma,\alpha,n\right) + f_\mathrm{CB}\left(m;\mu,\sigma,-\alpha,n\right), \tag{3}$$

where the Crystall Ball function is defined as [63]:

$$f_\mathrm{CB}\left(m;\mu,\sigma,\alpha,n\right) = N\cdot\begin{cases}\exp\left(-\frac{(m-\mu)^2}{2\sigma^2}\right), & \text{for } \frac{m-\mu}{\sigma}\geqslant-\alpha\\ \left(\frac{n}{|\alpha|}\right)^n\exp\left(-\frac{|\alpha|^2}{2}\right)\left(\frac{n}{|\alpha|}-|\alpha|-\frac{m-\mu}{\sigma}\right)^{-n}, & \text{for } \frac{m-\mu}{\sigma}\leqslant-\alpha\end{cases}. \tag{4}$$

The normalization factor N is given as

$$N = \frac{1}{\sigma\left(\frac{n}{|\alpha|}\frac{1}{n-1}\exp\left(-\frac{|\alpha|^2}{2}\right)+\sqrt{\frac{\pi}{2}}\left(1+\mathrm{erf}\left(\frac{|\alpha|}{\sqrt{2}}\right)\right)\right)},$$

where erf is the error function[11]. The α parameter in the second Crystall Ball function is set to the negative value of the α parameter in the first Crystall Ball to model the sysmetric tail of the Λ_b^0 signal shape. The Λ_c^+ and D^- signal shapes are modeled by the sum of two Gaussian functions (a double Gaussian function):

$$f_\mathrm{DG}\left(m;\mu,\sigma,r_\mathrm{G},r_\sigma\right) \coloneqq r_\mathrm{G}\cdot f_\mathrm{G}\left(m;\mu,\sigma\right) + f_\mathrm{G}\left(m;\mu,r_\sigma\cdot\sigma\right), \tag{5}$$

where f_G is the Gaussian function given as:

$$f_\mathrm{G} = \frac{1}{\sqrt{2\pi\sigma^2}}\exp\left(-\frac{(m-\mu)^2}{2\sigma^2}\right). \tag{6}$$

The ratios in Eq. 3 and Eq. 5 are introduced into the fit models to make the fit process more stable and it is more convenient to fix some fit parameters with these ratios. The fits to the Λ_b^0, Λ_c^+ and D^- shapes from the MC data are shown in Figure 14 and the fit parameters r_CB, α, n, r_G and r_σ[12] are listed in Table 8. The resolution of Λ_b^0 from the fits is also listed in Table 8, for later comparison to the fit results from the real data.

Because of the utilization of DTF, it is expected that the resolutions of the signal decay and the decays $\Lambda_\mathrm{b}^0 \to \Lambda_\mathrm{c}^+[\mathrm{K}^+\pi^-\pi^-]\overline{\mathrm{K}}^{*0}$ and $\Lambda_\mathrm{b}^0 \to [\mathrm{p}^+\mathrm{K}^-\pi^+]\mathrm{D}^-\overline{\mathrm{K}}^{*0}$ can be different. In order to make the 3D fits work, the resolutions of the latter two decays are the set the same, but different from the signal decay. Two probability density functions

[11] erf is define as $\mathrm{erf}\left(x\right) = \frac{2}{\pi}\int_0^x e^{-t^2}dt$.

[12] It is expected that the means, widths and the ratios of the widths of the shapes taken from the MC data can vary from the means and widths in the data. However the parameters which describes the shapes (α, n, $r_{\mathrm{CB,G},\sigma}$) should be fixed for the fits to the real data.

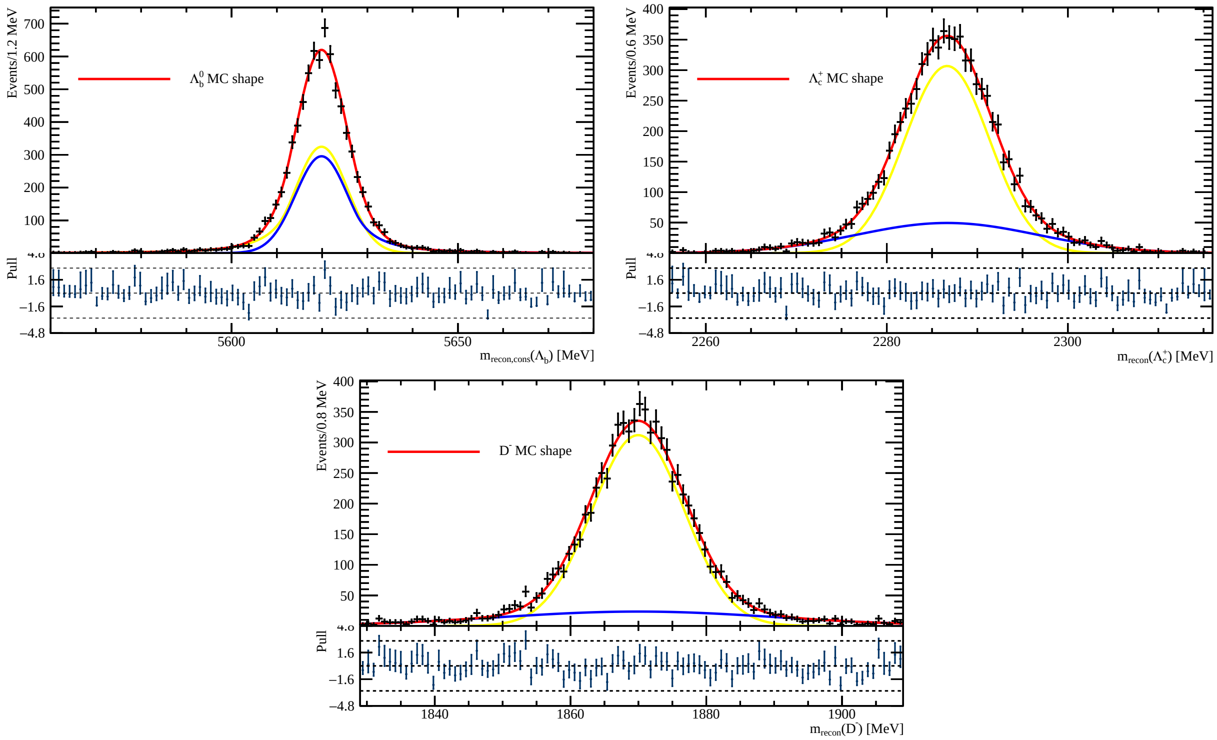

Figure 14: Fits to the shapes of Λ_{b}^0, Λ_{c}^+ and D^- in the MC data.

fit parameter	Λ_{b}^0	Λ_{c}^+	D^-
r_{CB}	0.523 ± 0.025	/	/
α	1.331 ± 0.080	/	/
n	3.02 ± 0.40	/	/
σ	$5.729 \pm 0.099\,\mathrm{MeV}$	/	/
r_{G}	/	0.744 ± 0.031	0.823 ± 0.019
r_σ	/	2.136 ± 0.062	3.02 ± 0.19

Table 8: Fit parameters returned from the fits to Λ_{b}^0, Λ_{c}^+ and D^- signal shapes in the MC data.

(p.d.f.s) are defined to model these two contributions:

$$F_{\Lambda_{\mathrm{b}}^0,\mathrm{Sig}} \coloneqq f_{\mathrm{DCB}}\left(m_{\Lambda_{\mathrm{b}}^0}; \mu_{\Lambda_{\mathrm{b}}^0}, \sigma_{\Lambda_{\mathrm{b}}^0,\mathrm{Sig}}, \alpha', n', r'_{\mathrm{CB}}\right), \text{ and}$$
$$F_{\Lambda_{\mathrm{b}}^0,\mathrm{singC}} \coloneqq f_{\mathrm{DCB}}\left(m_{\Lambda_{\mathrm{b}}^0}; \mu_{\Lambda_{\mathrm{b}}^0}, \sigma_{\Lambda_{\mathrm{b}}^0,\mathrm{singC}}, \alpha', n', r'_{\mathrm{CB}}\right),$$

where the subscript $_{\mathrm{signC}}$ denotes "single charm". The signal shapes of the three partially reconstructed decays (see section 4.2) extracted from the RapidSim simulated MC data using kernel density estimation are included as kernel density p.d.f.s, given as

$$F_{\Lambda_b^0 \to \Lambda_c^+ [D^- \gamma/\pi^0]_{D^{*-}} \overline{K}^{*0}} \coloneqq f_{\rm KDE}\left(m_{\Lambda_b^0} | x_{\Lambda_b^0 \to \Lambda_c^+ [D^- \gamma/\pi^0]_{D^{*-}} \overline{K}^{*0}}\right), \text{ and}$$
$$F_{\Lambda_b^0 \to [\Lambda_c^+ \pi^0]_{\Sigma_c^+} D^- \overline{K}^{*0}} \coloneqq f_{\rm KDE}\left(m_{\Lambda_b^0} | x_{\Lambda_b^0 \to [\Lambda_c^+ \pi^0]_{\Sigma_c^+} D^- \overline{K}^{*0}}\right).$$

The signal shapes of Λ_c^+ and D^- are modeled by the following p.d.f.s:

$$F_{\Lambda_c^+,\rm Sig} \coloneqq f_{\rm DG}\left(m_{\Lambda_c^+}; \mu_{\Lambda_c^+}, \sigma_{\Lambda_c^+}, r'_{G,\Lambda_c^+}, r'_{\sigma,\Lambda_c^+}\right), \text{ and}$$
$$F_{D^-,\rm Sig} \coloneqq f_{\rm DG}\left(m_{D^-}; \mu_{D^-}, \sigma_{D^-}, r'_{G,D^-}, r'_{\sigma,D^-}\right).$$

Fit parameters labeled with $'$ in the above given functions are fixed with values listed in Table 8, while the means and widths are to be determined by the fits.

The backgrounds of Λ_b^0, Λ_c^+ and D^- are modeled by the first order Chebychev polynomial[13], assuming they are flat (see section 4.2), given as

$$F_{\Lambda_b^0,\rm Bkg} \coloneqq f_{\rm Chebychev}\left(m_{\Lambda_b^0}; a_{\Lambda_b^0}\right) \coloneqq a_{\Lambda_b^0} \cdot T_1\left(m_{\Lambda_b^0}\right) = a_{\Lambda_b^0} \cdot m_{\Lambda_b^0},$$
$$F_{\Lambda_c^+,\rm Bkg} \coloneqq f_{\rm Chebychev}\left(m_{\Lambda_c^+}; a_{\Lambda_c^+}\right) \coloneqq a_{\Lambda_c^+} \cdot T_1\left(m_{\Lambda_c^+}\right) = a_{\Lambda_c^+} \cdot m_{\Lambda_c^+}, \text{ and}$$
$$F_{D^-,\rm Bkg} \coloneqq f_{\rm Chebychev}\left(m_{D^-}; a_{D^-}\right) \coloneqq a_{D^-} \cdot T_1\left(m_{D^-}\right) = a_{D^-} \cdot m_{D^-}.$$

The combinatorial backgrounds related to Λ_c^+ or D^-, random resonances formed by the final-state particles respectively, can be described by

$$F_{\Lambda_c^+,\rm Comb} \coloneqq F_{\Lambda_c^+,\rm Sig} \cdot F_{\Lambda_b^0,\rm Bkg} \cdot F_{D^-,\rm Bkg}, \text{ and}$$
$$F_{D^-,\rm Comb} \coloneqq F_{D^-,\rm Sig} \cdot F_{\Lambda_b^0,\rm Bkg} \cdot F_{\Lambda_c^+,\rm Bkg}.$$

A combined combinatorial background related Λ_c^+ and D^-, corresponding to the situation where the final-state particles form Λ_c^+ and D^- resonances at the same time, can be given as

$$F_{\Lambda_c^+ D^-,\rm Comb} \coloneqq F_{\Lambda_c^+,\rm Sig} \cdot F_{D^-,\rm Sig} \cdot F_{\Lambda_b^0,\rm Bkg}.$$

Analogously, the random combinatorial background, which will be flat in all the three dimensions, can be modeled by

$$F_{\rm Comb} \coloneqq F_{\Lambda_b^0,\rm Bkg} \cdot F_{\Lambda_c^+,\rm Bkg} \cdot F_{D^-,\rm Bkg}.$$

[13]The Chebychev polynomials of the first kind are defined by the recurrence relation: $T_0(x) = 1$, $T_1(x) = x, T_{n+1}(x) = 2xT_n(x) - T_{n-1}(x)$.

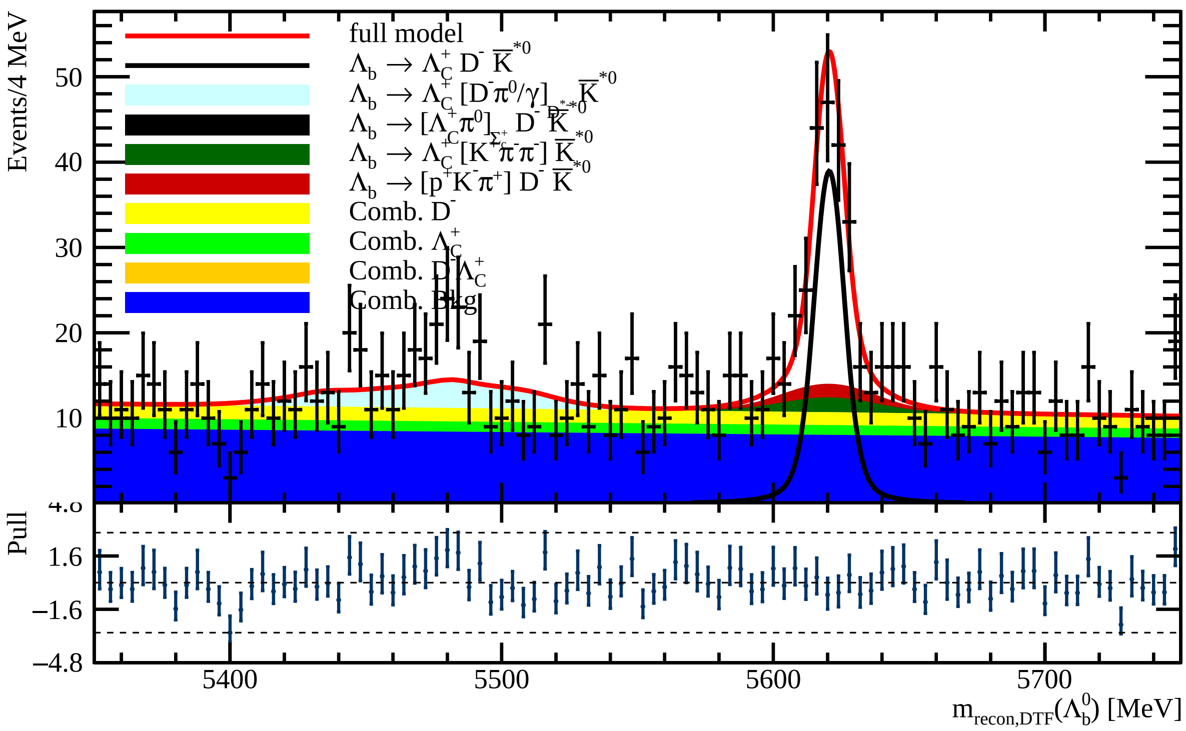

(a) Λ_b^0 mass from the 3D fits.

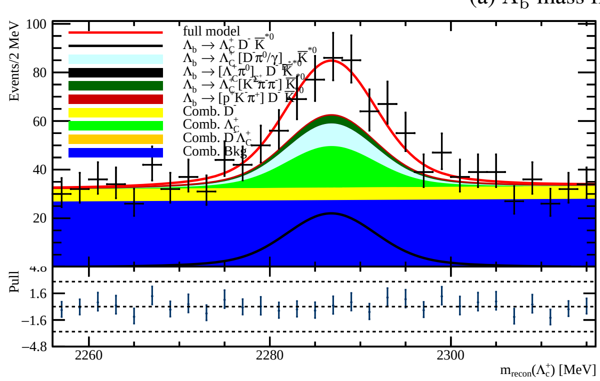

(b) Λ_c^+ mass from the 3D fits.

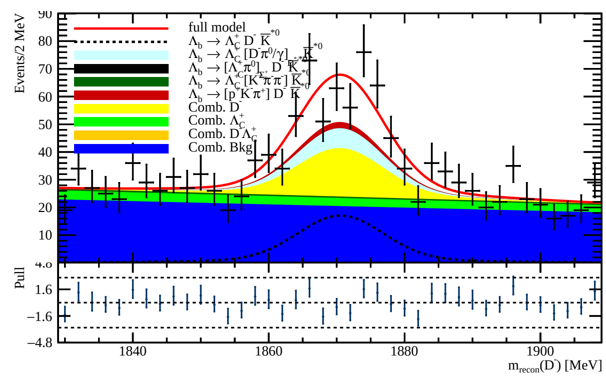

(c) D^- mass from the 3D fits.

Figure 15: Projections of the 3D mass fits into Λ_b^0, Λ_c^+ and D^- masses.

The total p.d.f. in the dimension of Λ_b^0 mass can be written as

$$\begin{aligned} F_{3D} = & N_{\Lambda_b^0 \to \Lambda_c^+ D^- \overline{K}^{*0}} \cdot F_{\Lambda_b^0,\mathrm{Sig}} \cdot F_{\Lambda_c^+,\mathrm{Sig}} \cdot F_{D^-,\mathrm{Sig}} \\ & + N_{\Lambda_b^0 \to \Lambda_c^+ [D^- \gamma/\pi^0]_{D^{*-}} \overline{K}^{*0}} \cdot F_{\Lambda_b^0 \to \Lambda_c^+ [D^- \gamma/\pi^0]_{D^{*-}} \overline{K}^{*0}} \cdot F_{\Lambda_c^+,\mathrm{Sig}} \cdot F_{D^-,\mathrm{Sig}} \\ & + N_{\Lambda_b^0 \to [\Lambda_c^+ \pi^0]_{\Sigma_c^+} D^- \overline{K}^{*0}} \cdot F_{\Lambda_b^0 \to [\Lambda_c^+ \pi^0]_{\Sigma_c^+} D^- \overline{K}^{*0}} \cdot F_{\Lambda_c^+,\mathrm{Sig}} \cdot F_{D^-,\mathrm{Sig}} \\ & + N_{\Lambda_b^0 \to \Lambda_c^+ [K^+ \pi^- \pi^-] \overline{K}^{*0}} \cdot F_{\Lambda_b^0,\mathrm{singC}} \cdot F_{\Lambda_c^+,\mathrm{Sig}} \cdot F_{D^-,\mathrm{Bkg}} \\ & + N_{\Lambda_b^0 \to [p^+ K^- \pi^+] D^- \overline{K}^{*0}} \cdot F_{\Lambda_b^0,\mathrm{singC}} \cdot F_{\Lambda_c^+,\mathrm{Bkg}} \cdot F_{D^-,\mathrm{Sig}} \\ & + N_{\mathrm{Bkg}} \left(r_{\Lambda_c^+,\mathrm{Comb}} \cdot F_{\Lambda_c^+,\mathrm{Comb}} + r_{D^-,\mathrm{Comb}} \cdot F_{D^-,\mathrm{Comb}} + r_{\Lambda_c^+ D^-,\mathrm{Comb}} \cdot F_{\Lambda_c^+ D^-,\mathrm{Comb}} + F_{\mathrm{Comb}} \right), \end{aligned} \tag{7}$$

which is used to fit the Λ_b^0 mass in the range $[5350\,\mathrm{MeV}, 5750\,\mathrm{MeV}]$. The plots of the 3D mass fits are demonstrated in Figure 15 and the fit parameters are given in Table 9.

fit parameter	Λ_b^0	Λ_c^+	D^-
μ/MeV	5620.60 ± 0.62	2286.80 ± 0.44	1870.60 ± 0.53
$\sigma / \left(\sigma_{\Lambda_b^0,\mathrm{singC}}\right)$ MeV	$5.66 \pm 0.60\,(18.0 \pm 9.3)$	4.73 ± 0.41	6.24 ± 0.50
a	-0.066 ± 0.057	0.021 ± 0.057	-0.113 ± 0.058
$N_{\Lambda_b^0 \to \Lambda_c^+ D^- \overline{K}^{*0}}$	151 ± 18		
$N_{\Lambda_b^0 \to \Lambda_c^+ [D^- \gamma/\pi^0]_{D^{*-}} \overline{K}^{*0}}$	64 ± 18		
$N_{\Lambda_b^0 \to [\Lambda_c^+ \pi^0]_{\Sigma_c^+} D^- \overline{K}^{*0}}$	0 ± 15		
$N_{\Lambda_b^0 \to \Lambda_c^+ [K^+ \pi^- \pi^-] \overline{K}^{*0}}$	21 ± 17		
$N_{\Lambda_b^0 \to [p^+ K^- \pi^+] D^- \overline{K}^{*0}}$	19 ± 17		
N_{Bkg}	1095 ± 40		
$r_{\Lambda_c^+,\mathrm{Comb}}$	0.107 ± 0.028		
$r_{D^-,\mathrm{Comb}}$	0.141 ± 0.028		
$r_{\Lambda_c^+ D^-,\mathrm{Comb}}$	0.000 ± 0.013		

Table 9: Fit parameters for Λ_b^0, Λ_c^+ and D^- from the 3D mass fits.

It can be seen in Figure 7 that the partially reconstructed decays have no leakage into the signal peak. Several conclusions can be drawn from the fit result. The combined combinatorial background related to Λ_c^+ and D^- is negligible. The contributions of the decays $\Lambda_b \to \Lambda_c^+[K^+\pi^-\pi^-]\overline{K}^{*0}$ and $\Lambda_b \to [p^+K^-\pi^+]D^-\overline{K}^{*0}$ are also negligible. The resolution of Λ_b^0 mass related to the signal decay is in 1σ accordance with the resolution from the fit to the MC data.

However, the 3D mass fits cannot estimate the background of the decay $\Lambda_b^0 \to \Lambda_c^+ D^- [K^-\pi^+]$, which is expected to have significant contribution to the signal peak. To isolate this decay from the signal decay, the $\overline{K}^{*0}$ mass needs to be included in the fits. The fits can be expanded into 4D mass fits, to study the background of the non-resonant K^- and π^+ and restudy the contributions of the two decays $\Lambda_b \to \Lambda_c^+[K^+\pi^-\pi^-]\overline{K}^{*0}$ and $\Lambda_b \to [p^+K^-\pi^+]D^-\overline{K}^{*0}$.

Useful information obtained from the 3D fits can be used to simply the 4D fit model. The fits can be conducted to a narrower range of $\Lambda_{\rm b}^{0}$ mass and no combined combinatorial needs to be included.

4.4.2 4D Mass Fits

According to PDG, $\overline{\rm K}^{*0}$ is a spin 1 resonance. The signal shape of $\overline{\rm K}^{*0}$ is expected to be describe by the relativistic Breit-Wigner function for a two-body decay, which takes the progagation and the spin of the intermediate resonance into consideration [64]. The definition is given by [65]

$$f_{\rm RelBW}\left(m;\mu,\Gamma,J,R\right)=\frac{m^{2}}{\left(m^{2}-\mu^{2}\right)^{2}+\mu^{2}\Gamma^{2}\left(m\right)},\tag{8}$$

where the mass dependent with Γ is defined as

$$\begin{aligned}\Gamma\left(m\right)&=\Gamma_{0}\frac{\mu}{m}\left(\frac{k\left(m\right)}{k\left(\mu\right)}\right)^{2J+1}\frac{F\left(Rk\left(m\right)\right)}{F\left(Rk\left(\mu\right)\right)},\ \text{with}\\ k\left(m\right)&=\frac{m}{2}\left(1-\frac{\left(m_{a}+m_{b}\right)^{2}}{m^{2}}\right)^{\frac{1}{2}}\left(1-\frac{\left(m_{a}-m_{b}\right)^{2}}{m^{2}}\right)^{\frac{1}{2}},\end{aligned}$$

where the function F is the spin dependent Blatt-Weisskopft form factor

$$\begin{aligned}F^{J=0}\left(x\right)&=1,\\ F^{J=1}\left(x\right)&=\frac{1}{1+x^{2}},\\ F^{J=2}\left(x\right)&=\frac{1}{9+3x^{2}+x^{4}},\end{aligned}$$

and the parameters Γ, J and R denote the decay width, the spin and the interaction radius of the resonance. There are some previous studies about R for assorted resonance including $\overline{\rm K}^{*0}$ [66, 67, 68, 69], but no special reason to fix R for $\overline{\rm K}^{*0}$ can be found. For the fit to the MC data, the range for R is set to $\left[-0.001\,{\rm MeV}^{-1},0.005\,{\rm MeV}^{-1}\right]$ and J is fixed to 1. The plot from the fit is given in Figure 16 (a). The fit result suggests that the relativistic Breit-Wigner function describes the $\overline{\rm K}^{*0}$ signal shape in the MC data relatively well. However it does not describe the upper tail very well. As an alternative, the sum of a non-relativistic Breit-Wigner function and a Crystall Ball function is used to fit the $\overline{\rm K}^{*0}$ signal shape in the MC data, defined as

$$f_{\rm BWCB}\left(m;\mu,\Gamma,\sigma,\alpha,n,r_{\rm BW}\right)\coloneqq r_{\rm BW}\cdot f_{\rm BW}\left(m;\mu,\Gamma\right)+f_{\rm CB}\left(m;\mu,\sigma,\alpha,n\right).\tag{9}$$

Scattering via a intermediate resonance can be described by the non-relativistic Breit-Wigner function [70], given by

$$f_{\rm BW}\left(m;\mu,\Gamma\right)=\frac{\Gamma}{2}\frac{1}{\left(m-\mu\right)^{2}+\left(\frac{\Gamma}{2}\right)^{2}}.\tag{10}$$

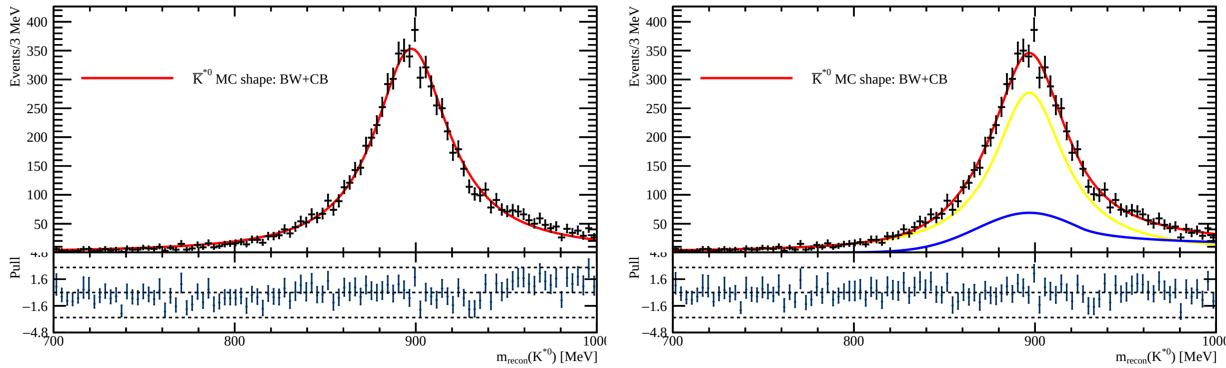

(a) Fit to the $\overline{\mathrm{K}}^{*0}$ signal shape in the MC data using a relativistic Breit-Wigner function.

(b) Fit to the $\overline{\mathrm{K}}^{*0}$ signal shape from the MC data using the sum of a Breit-Wigner function and a Crystall Ball function.

Figure 16: Fits to the $\overline{\mathrm{K}}^{*0}$ signal shape in the MC data.

The Crystall ball function (see Eq. 4) is used to model the asymmetry shape. The fit parameter Γ is constraint to $47.3 \pm 0.5\,\mathrm{MeV}$, the width given by PDG. The plot from the fit is given in Figure 16 (b). The pulls are more homogeneously distributed. The fit results are listed in Table 10[14] for the two different p.d.f.s. The p.d.f. for $\overline{\mathrm{K}}^{*0}$ signal shape for the $4\mathrm{D}$ mass fits is defined as

$$F_{\overline{\mathrm{K}}^{*0},\mathrm{Sig}} \coloneqq f_{\mathrm{BWCB}}\left(m;\mu,\Gamma',\sigma',\alpha',n',r'_{\mathrm{BW}}\right),$$

where fit parameters labeled with $'$ are to be fixed in the fit procedure.

formular	Γ/MeV	σ/MeV	α	n	r_{BW}	R/MeV^{-1}
f_{RelBW}	50.1 ± 1.0	/	/	/	/	0.0027 ± 0.0018
f_{BWCB}	46.96 ± 0.50	29.0 ± 2.1	-0.99 ± 0.21	0.44 ± 0.32	0.750 ± 0.034	/

Table 10: Fit parameters for $\overline{\mathrm{K}}^{*0}$ signal shape in the MC data.

The background of $\overline{\mathrm{K}}^{*0}$ is modeled by a second order Chebychev polynomial, to describe the slight curvature of the phase space distribution, given by

$$F_{\overline{\mathrm{K}}^{*0},\mathrm{Bkg}} \coloneqq f_{\mathrm{Chebychev}}\left(m_{\overline{\mathrm{K}}^{*0}};a_{\overline{\mathrm{K}}^{*0}},b_{\overline{\mathrm{K}}^{*0}}\right) \coloneqq 2a_{\overline{\mathrm{K}}^{*0}}\cdot m^2_{\overline{\mathrm{K}}^{*0}} - b_{\overline{\mathrm{K}}^{*0}}.$$

The models for the signal decay, the decays $\Lambda_{\mathrm{b}}^0 \to \Lambda_{\mathrm{c}}^+[\mathrm{K}^+\pi^-\pi^-]\overline{\mathrm{K}}^{*0}$ and $\Lambda_{\mathrm{b}}^0 \to [\mathrm{p}^+\mathrm{K}^-\pi^+]\mathrm{D}^-\overline{\mathrm{K}}^{*0}$, and the Λ_{c}^+ and D^- signal shapes are exactly the same as in section 4.4.1. A new entry needs to be added to the total p.d.f., to estimate the background of the decay $\Lambda_{\mathrm{b}}^0 \to \Lambda_{\mathrm{c}}^+\mathrm{D}^-[\mathrm{K}^-\pi^+]$. The $\overline{\mathrm{K}}^{*0}$ combinatorial background, which is random

[14] The mean will be floating for the fits to the real data, see section 4.4.1.

resonance of K^- and π^+ is added to the combinatorial backgrounds given in section 4.4.1 (except the combined $\Lambda_c^+\mathrm{D}^-$ combinatorial background) to model all combinatorial backgrounds in the 4D mass fits, which are defined as:

$$\begin{aligned}
F_{\mathrm{Comb}} &\coloneqq F_{\Lambda_b^0,\mathrm{Bkg}} \cdot F_{\Lambda_c^+,\mathrm{Bkg}} \cdot F_{\mathrm{D}^-,\mathrm{Bkg}} \cdot F_{\overline{\mathrm{K}}^{*0},\mathrm{Bkg}}, \\
F_{\Lambda_c^+,\mathrm{Comb}} &\coloneqq F_{\Lambda_b^0,\mathrm{Bkg}} \cdot F_{\Lambda_c^+,\mathrm{Sig}} \cdot F_{\mathrm{D}^-,\mathrm{Bkg}} \cdot F_{\overline{\mathrm{K}}^{*0},\mathrm{Bkg}}, \\
F_{\mathrm{D}^-,\mathrm{Comb}} &\coloneqq F_{\Lambda_b^0,\mathrm{Bkg}} \cdot F_{\Lambda_c^+,\mathrm{Bkg}} \cdot F_{\mathrm{D}^-,\mathrm{Sig}} \cdot F_{\overline{\mathrm{K}}^{*0},\mathrm{Bkg}}, \\
F_{\overline{\mathrm{K}}^{*0},\mathrm{Comb}} &\coloneqq F_{\Lambda_b^0,\mathrm{Bkg}} \cdot F_{\Lambda_c^+,\mathrm{Bkg}} \cdot F_{\mathrm{D}^-,\mathrm{Sig}} \cdot F_{\overline{\mathrm{K}}^{*0},\mathrm{Sig}}.
\end{aligned}$$

Similarly, the total p.d.f. for the 4D mass fits can be written as

$$\begin{aligned}
F_{\mathrm{4D}} = & N_{\Lambda_b^0\to\Lambda_c^+\mathrm{D}^-\overline{\mathrm{K}}^{*0}} \cdot F_{\Lambda_b^0,\mathrm{Sig}} \cdot F_{\Lambda_c^+,\mathrm{Sig}} \cdot F_{\mathrm{D}^-,\mathrm{Sig}} \cdot F_{\overline{\mathrm{K}}^{*0},\mathrm{Sig}} \\
& + N_{\Lambda_b^0\to\Lambda_c^+[\mathrm{K}^+\pi^-\pi^-]\overline{\mathrm{K}}^{*0}} \cdot F_{\Lambda_b^0,\mathrm{singC}} \cdot F_{\Lambda_c^+,\mathrm{Sig}} \cdot F_{\mathrm{D}^-,\mathrm{Bkg}} \cdot F_{\overline{\mathrm{K}}^{*0},\mathrm{Sig}} \\
& + N_{\Lambda_b^0\to[\mathrm{p}^+\mathrm{K}^-\pi^+]\mathrm{D}^-\overline{\mathrm{K}}^{*0}} \cdot F_{\Lambda_b^0,\mathrm{singC}} \cdot F_{\Lambda_c^+,\mathrm{Bkg}} \cdot F_{\mathrm{D}^-,\mathrm{Sig}} \cdot F_{\overline{\mathrm{K}}^{*0},\mathrm{Sig}} \\
& + N_{\Lambda_b^0\to\Lambda_c^+\mathrm{D}^-[\mathrm{K}^-\pi^+]} \cdot F_{\Lambda_b^0,\mathrm{Sig}} \cdot F_{\Lambda_c^+,\mathrm{Sig}} \cdot F_{\mathrm{D}^-,\mathrm{Sig}} \cdot F_{\overline{\mathrm{K}}^{*0},\mathrm{Bkg}} \\
& + N_{\mathrm{Bkg}} \left(r_{\Lambda_c^+,\mathrm{Comb}} \cdot F_{\Lambda_c^+,\mathrm{Comb}} + r_{\mathrm{D}^-,\mathrm{Comb}} \cdot F_{\mathrm{D}^-,\mathrm{Comb}} + r_{\overline{\mathrm{K}}^{*0},\mathrm{Comb}} \cdot F_{\overline{\mathrm{K}}^{*0},\mathrm{Comb}} + F_{\mathrm{Comb}} \right),
\end{aligned} \tag{11}$$

which is used to fit the Λ_b^0 mass in the range $[5560\,\mathrm{MeV}, 5680\,\mathrm{MeV}]$. It needs to be mentioned that the resolution of Λ_b^0 mass corresponding to the decay $\Lambda_b^0 \to \Lambda_c^+\mathrm{D}^-[\mathrm{K}^-\pi^+]$ is set the same as to the signal decay, since the DTF does not contain any constraint on $\overline{\mathrm{K}}^{*0}$. The fit parameters listed in Table 8 and Table 10 are fixed in Eq. 11 in the fit procedure.

The plots of the 4D mass fits are illustrated in Figure 17 and the fit parameters are given in Table 11.

From the fit result, the signal yield are 63 ± 15. The resolution of Λ_b^0 mass related to the signal decay is in 1σ accordance of the resolution from the fit to the MC data. The resolution of Λ_b^0 mass related to the decays $\Lambda_b^0 \to \Lambda_c^+[\mathrm{K}^+\pi^-\pi^-]\overline{\mathrm{K}}^{*0}$ and $\Lambda_b^0 \to [\mathrm{p}^+\mathrm{K}^-\pi^+]\mathrm{D}^-\overline{\mathrm{K}}^{*0}$ is $42 \pm 22\,\mathrm{MeV}$, which is too much large than the resolution corresponding to the signal decay. The yields of the decay $\Lambda_b^0 \to \Lambda_c^+\mathrm{D}^-[\mathrm{K}^-\pi^+]$ is 97 ± 16, while the yields of the decays $\Lambda_b^0 \to \Lambda_c^+[\mathrm{K}^+\pi^-\pi^-]\overline{\mathrm{K}}^{*0}$ and $\Lambda_b^0 \to [\mathrm{p}^+\mathrm{K}^-\pi^+]\mathrm{D}^-\overline{\mathrm{K}}^{*0}$ are not so significantly different from 0. Together with the result of the 3D mass fits, it is concluded that the contributions of the two decays $\Lambda_b^0 \to \Lambda_c^+[\mathrm{K}^+\pi^-\pi^-]\overline{\mathrm{K}}^{*0}$ and $\Lambda_b^0 \to [\mathrm{p}^+\mathrm{K}^-\pi^+]\mathrm{D}^-\overline{\mathrm{K}}^{*0}$ are negligible, and the contribution of the decay $\Lambda_b^0 \to \Lambda_c^+\mathrm{D}^-[\mathrm{K}^-\pi^+]$ is dominant. 2D mass fits will be enough to estimate the background of the decay $\Lambda_b^0 \to \Lambda_c^+\mathrm{D}^-[\mathrm{K}^-\pi^+]$.

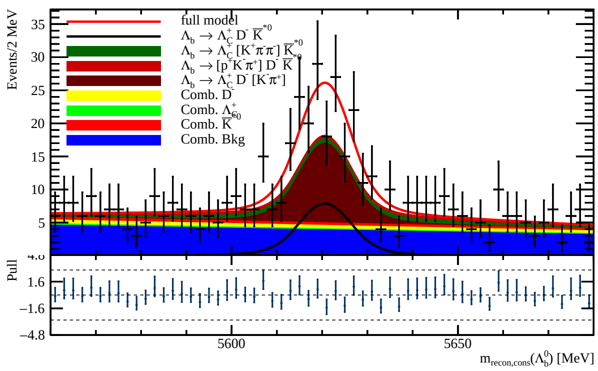

(a) Λ_b spectrum from the 4D mass fits.

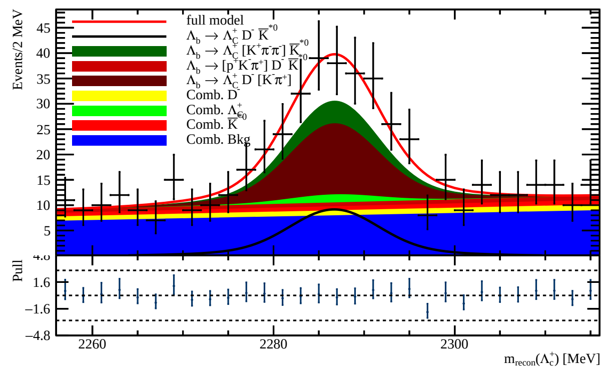

(b) Λ_c^+ spectrum from the 4D mass fits.

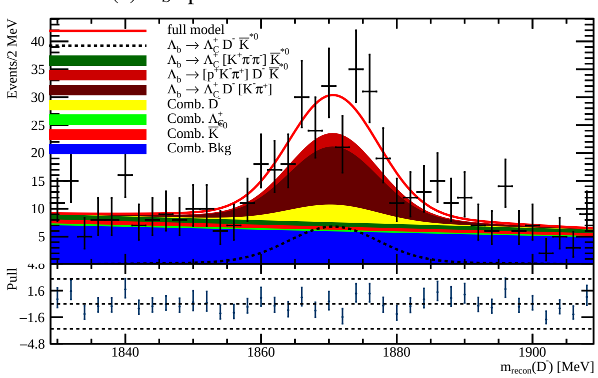

(c) D^- spectrum from the 4D mass fits.

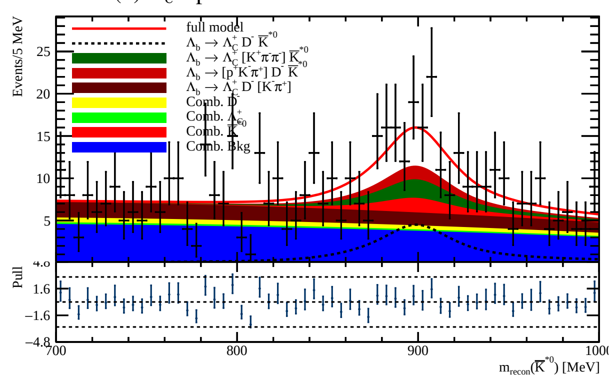

(d) $\overline{K}^{*0}$ spectrum from the 4D mass fits.

Figure 17: Projections of the 4D mass fits into Λ_b^0, Λ_c^+, D^- and $\overline{K}^{*0}$ spectra.

fit parameter	Λ_b^0	Λ_c^+	D^-	$\overline{K}^{*0}$
μ/MeV	5620.60 ± 0.64	2286.70 ± 0.50	1870.70 ± 0.67	899.0 ± 4.0
$\sigma/\left(\sigma_{\Lambda_b^0,\mathrm{singC}}\right)$ MeV	$5.90 \pm 0.63\,(42 \pm 22)$	4.75 ± 0.43	6.55 ± 0.60	/
a	-0.18 ± 0.10	0.131 ± 0.098	-0.18 ± 0.10	-0.20 ± 0.12
b	/	/	/	-0.03 ± 0.11
$N_{\Lambda_b^0 \to \Lambda_c^+ D^- \overline{K}^{*0}}$	63 ± 15			
$N_{\Lambda_b^0 \to \Lambda_c^+ [K^+\pi^-\pi^-] \overline{K}^{*0}}$	31 ± 16			
$N_{\Lambda_b^0 \to [p^+K^-\pi^+] D^- \overline{K}^{*0}}$	23 ± 15			
$N_{\Lambda_b^0 \to \Lambda_c^+ D^- [K^-\pi^+]}$	97 ± 16			
N_{Bkg}	304 ± 28			
$r_{\Lambda_c^+,\mathrm{Comb}}$	0.036 ± 0.061			
$r_{D^-,\mathrm{Comb}}$	0.097 ± 0.059			
$r_{\overline{K}^{*0},\mathrm{Comb}}$	0.079 ± 0.075			

Table 11: Fit parameters for Λ_b^0, Λ_c^+, D^- and $\overline{K}^{*0}$ from the 4D mass fits.

4.4.3 2D Mass Fits

In 2D, the combinatorial backgrounds can be written as:

$$
\begin{aligned}
F_{\mathrm{Comb}} &\coloneqq F_{\Lambda_b^0,\mathrm{Bkg}} \cdot F_{\overline{K}^{*0},\mathrm{Bkg}}, \\
F_{\overline{K}^{*0},\mathrm{Comb}} &\coloneqq F_{\Lambda_b^0,\mathrm{Bkg}} \cdot F_{\overline{K}^{*0},\mathrm{Sig}}.
\end{aligned}
$$

The total p.d.f is given by

$$
\begin{aligned}
F_{2\mathrm{D}} = {} & N_{\Lambda_b^0 \to \Lambda_c^+ D^- \overline{K}^{*0}} \cdot F_{\Lambda_b^0,\mathrm{Sig}} \cdot F_{\overline{K}^{*0},\mathrm{Sig}} \\
& + N_{\Lambda_b^0 \to \Lambda_c^+ D^- [K^-\pi^+]} \cdot F_{\Lambda_b^0,\mathrm{Sig}} \cdot F_{\overline{K}^{*0},\mathrm{Bkg}} \\
& + N_{\mathrm{Bkg}} \left(r_{\overline{K}^{*0},\mathrm{Comb}} \cdot F_{\overline{K}^{*0},\mathrm{Comb}} + F_{\mathrm{Comb}} \right),
\end{aligned}
\tag{12}
$$

which is used to fit the Λ_b^0 mass in the range $[5560\,\mathrm{MeV}, 5680\,\mathrm{MeV}]$. Again, for the fits, the parameters listed in Table 8 and Table 10 are fixed in Eq. 12. The plots of the 2D mass fits are given in Figure 18. The fit result provided listed in Table 12.

From the fit result, the signal yield are 66 ± 17, which is in 1σ accordance with the signal yields returned from the 4D mass fits (see Table 11). The resolution of Λ_b^0 mass related to the signal decay is in 1σ accordance with the resolution from the fit to the MC data. The yields of the decay $\Lambda_b^0 \to \Lambda_c^+ D^- [K^-\pi^+]$ is 95 ± 19, which is in 1σ accordance with the yields from the 4D mass fits (see Table 11). The contribution of the two decays $\Lambda_b^0 \to \Lambda_c^+ [K^+\pi^-\pi^-] \overline{K}^{*0}$ and $\Lambda_b^0 \to [p^+K^-\pi^+] D^- \overline{K}^{*0}$ are absorbed into the random combinatorial background, which is

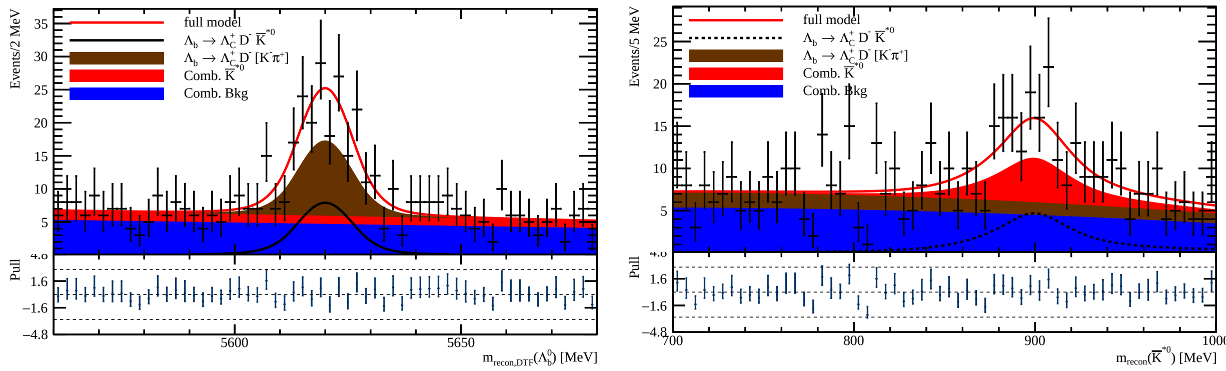

(a) Λ_b spectrum from the 2D fits.

(b) $\overline{K}^{*0}$ spectrum from the 2D fits.

Figure 18: Projections of the 2D mass fits into Λ_b^0 and $\overline{K}^{*0}$ spectra.

fit parameter	Λ_b^0	$\overline{K}^{*0}$
μ/MeV	5620.00 ± 0.76	900 ± 4.1
σ/MeV	6.11 ± 0.84	/
a	-0.130 ± 0.094	-0.20 ± 0.12
b	/	-0.05 ± 0.11
$N_{\Lambda_b^0 \to \Lambda_c^+ D^- \overline{K}^{*0}}$	66 ± 17	
$N_{\Lambda_b^0 \to \Lambda_c^+ D^- [K^- \pi +]}$	95 ± 19	
N_{Bkg}	357 ± 24	
$r_{\overline{K}^{*0},\text{Comb}}$	0.206 ± 0.069	

Table 12: Fit parameters for Λ_b^0 and $\overline{K}^{*0}$ from the 2D mass fits.

consistent with the expectation above that the 4D mass fits can be simplified by 2D mass fits.

4.5 A Brief Efficiency Study

A brief efficiency study is conducted in this section, to get the efficiency corrected signal yields from the 2D mass fits. Two types of efficiencies needed to be considered: the efficiency of detector acceptance, trigger, reconstruction and stripping (denoted by ϵ_{ARTS}) and the efficiency of the offline cut-based selection including PID efficiency (ϵ_{PID}), efficiency of cuts related to kinematics, reconstruction quality of decay vertices, angular acceptance (ϵ_{kin}), efficiency of the veto cuts (ϵ_{veto}) and efficiency of the mass cuts (ϵ_{mass}). The two types of efficiencies are extracted from the generated and fully detector simulated MC data, assuming that the MC data can describe the real data well. The general form to calculated the efficiency of a selection process A is given by

$$\epsilon_{\text{A}} := \frac{N_{\text{passed}}}{N_{\text{input}}}, \tag{13}$$

where N_{input} and N_{passed} denote the event number before and after the selection process. The total efficiency will be calculated in the following order. At first the efficiency ϵ_{ARTS} is calculated, by comparing the event number of the generated MC data and the event number of the MC data passing the stripping lines. Then ϵ_{PID} is obtained, using the PIDCalib package. Finally ϵ_{kin}, ϵ_{veto} and ϵ_{mass} are calculated in the mentioned order. The total efficiency ϵ_{tot} can be written as

$$\epsilon_{\mathrm{tot}} \coloneqq \epsilon_{\mathrm{ARTS}} \cdot \epsilon_{\mathrm{PID}} \cdot \epsilon_{\mathrm{kin}} \cdot \epsilon_{\mathrm{veto}} \cdot \epsilon_{\mathrm{mass}}, \tag{14}$$

with error obtained by the Gaussian error propagation

$$\Delta_{\epsilon_{\mathrm{tot}}} = \epsilon_{\mathrm{ARTS}}\epsilon_{\mathrm{PID}}\epsilon_{\mathrm{kin}}\epsilon_{\mathrm{veto}}\epsilon_{\mathrm{mass}} \left(\left(\frac{\Delta_{\epsilon_{\mathrm{ARTS}}}}{\epsilon_{\mathrm{ARTS}}} \right) + \left(\frac{\Delta_{\epsilon_{\mathrm{PID}}}}{\epsilon_{\mathrm{PID}}} \right) + \left(\frac{\Delta_{\epsilon_{\mathrm{kin}}}}{\epsilon_{\mathrm{kin}}} \right) + \left(\frac{\Delta_{\epsilon_{\mathrm{veto}}}}{\epsilon_{\mathrm{veto}}} \right) + \left(\frac{\Delta_{\epsilon_{\mathrm{mass}}}}{\epsilon_{\mathrm{mass}}} \right) \right)^{\frac{1}{2}} \tag{15}$$

4.5.1 Efficiency of Detector Acceptance, Trigger, Reconstruction and Stripping

The Efficiency of detector acceptance, trigger, reconstruction and stripping ϵ_{ARTS} is obtained in the following way. Several dozons of small samples containing the event number of generated MC data and the event number passing the whole selection process of detector acceptance, trigger, reconstruction and stripping are produced. The efficiency obtained from each sample is registered in a histogram. The histogram is fitted with a Gaussian p.d.f.. The mean and σ of the Gaussian distribution is the value and error of ϵ_{ARTS}. The fit result returns $\epsilon_{\mathrm{ARTS}} = 4.17\% \pm 0.56\%$.

4.5.2 Efficiency of the Offline Cut-based Selection

The calculation of the efficiency of the offline cut-based selection, including the efficiency of the PID cuts, the efficiency of kinematic cuts, cuts related to tracks and decay vertices reconstruction quality and acceptance cuts, the efficiency of veto cuts and the efficiency of mass cuts (see Table 7), is described in the following. Before calculating the efficiencies, the distributions of two commonly used control variables, p_{T} and η of Λ_{b}^{0}, of the data weighted by ${}_{s}Weights$[15] (the sweighted data) and the fully detector simulated MC data are compared, to control if the MC data matches the real data. The ${}_{s}Weights$ are the weights assigned to each event using the ${}_{s}Plot$ technique embedded in the ROOT framework [71, 72], to statistically remove background contribution. Shown in Figure 19, the distributions of the MC and sweighted data match relatively well. No weighting procedure is needed for the MC data.

The PID efficiency ϵ_{PID} is calculated by the PIDCalib package. The efficiency of the PID cuts of each single final-state particle is calculated from the data samples used in the PIDCalib package, using a customed binning scheme[16] for three default kinematic variables, p (momentum), η (pseudorapidity) and $\mathrm{nTracks}$ (track multiplicity). Sample datasets used by the PIDCalib package are divided into years and magnet polarities (for this analysis: 2011MagUp, 2011MagDown, 2012MagUp and 2012MagDown). Here as a brief efficiency study, the averaged efficiency of the four combinations will be used as the efficiency of the PID cuts applied to the final-state particles. Efficiencies for all the

[15] The data refers to the data passing the offline cut-based selection.

[16] The binning for p is $[0, 300000\,\mathrm{MeV}]$ with bin boundries $15000\,\mathrm{MeV}$ and $30000\,\mathrm{MeV}$, for η $[1.0, 5.5]$ with bin boundries 3.0 and 3.5 and for $\mathrm{nTracks}$ $[0, 800]$ with bin boundries 130 and 200.

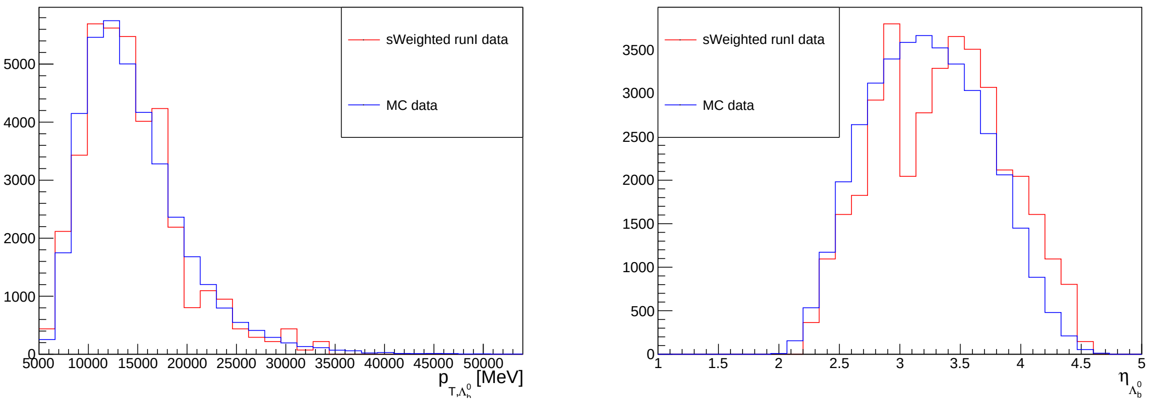

(a) Comparison of distributions of $p_{\mathrm{T},\Lambda_b^0}$ of the $_sWeighted$ runI data.

(b) Comparison of distributions of $\eta_{\Lambda_b^0}$ of the $_sWeighted$ runI data.

Figure 19: Comparison of the $_sWeighted$ runI data and the MC data in $p_{\mathrm{T},\Lambda_b^0}$ and $\eta_{\Lambda_b^0}$.

PID cuts listed in Table 7 are given in Table 13. Assuming PID cuts on different final-state tracks are independent of each other. The total PID efficiency can be given by the product of all averaged efficiencies with the Gaussian error propagation, which is $\epsilon_{\mathrm{PID}} = 68.62\% \pm 0.93\%$. The PID cuts are applied to the MC data before the next step.

The efficiency of kinematic cuts, cuts related to tracks and decay vertices reconstruction quality and acceptance cuts ϵ_{kin} is extracted from the MC data, by comparing the numbers of event before and after applying these cuts, which is $\epsilon_{\mathrm{kin}} = 55.85\% \pm 0.58\%$. These cuts are applied to the MC data before getting the efficiency of the veto cuts.

Using the same method, the veto efficiency is $\epsilon_{\mathrm{veto}} = 55.98\% \pm 0.78\%$. Veto cuts are applied to the MC data before getting the efficiency of the mass cuts, including a mass cut on Λ_b^0 mass: $\Lambda_b^0 \in (5560\,\mathrm{MeV}, 5680\,\mathrm{MeV})$, which is the range used in the 2D mass fits. The efficiency of the mass cuts is found to be $\epsilon_{\mathrm{mass}} = 99.6\% \pm 1.6\%$.

Using Eq. 14 and Eq. 15, the total efficiency is $\epsilon_{\mathrm{tot}} = 0.89\% \pm 0.12\%$.

4.6 Summary

This can be concluded as the first observation of the decay $\Lambda_b^0 \to \Lambda_c^+ \mathrm{D}^- \overline{\mathrm{K}}^{*0}$. With the signal yields from the 2D mass fits $N_{\Lambda_b^0 \to \Lambda_c^+ \mathrm{D}^- \overline{\mathrm{K}}^{*0}} = 66 \pm 17$ and the efficiency $\epsilon_{\mathrm{tot}} = 0.89\%$, the efficiency corrected signal yields from the 2D mass fits are calculated as $N_{\Lambda_b^0 \to \Lambda_c^+ \mathrm{D}^- \overline{\mathrm{K}}^{*0},\mathrm{corr}} = 7400 \pm 2200$. The error is purely statistical. The main contribution to the error is the relatively large error of the signal yields from the 2D mass fits, mainly because of the low statistics data sample.

particle	PID cut	dataset	efficiency
p^+	prod_ProbNN_p_K > 0.03 and	2011MagUp	$93.162\% \pm 0.022\%$
	prod_ProbNN_p_$\pi > 0.03$	2011MagDown	$92.821\% \pm 0.016\%$
	averaged efficiency	2012MagUp	$94.751\% \pm 0.049\%$
	$93.6\% \pm 1.0\%$	2012MagDown	/[17]
$K^-(\Lambda_c^+)$	prod_ProbNN_K_$\pi > 0.05$	2011MagUp	$94.7825\% \pm 0.0018\%$
		2011MagDown	$94.8758\% \pm 0.0014\%$
	averaged efficiency	2012MagUp	$94.94990\% \pm 0.00065\%$
	$94.98\% \pm 0.22\%$	2012MagDown	$95.29669\% \pm 0.00060\%$
$\pi^+(\Lambda_c^+)$	prod_ProbNN_π_K > 0.05	2011MagUp	$99.1243\% \pm 0.0011\%$
		2011MagDown	$99.12079\% \pm 0.00093\%$
	averaged efficiency	2012MagUp	$99.17278\% \pm 0.00042\%$
	$99.152\% \pm 0.035\%$	2012MagDown	$99.19140\% \pm 0.00040\%$
K^+	prod_ProbNN_K_$\pi > 0.05$	2011MagUp	$94.8423\% \pm 0.0018\%$
		2011MagDown	$94.8834\% \pm 0.0014\%$
	averaged efficiency	2012MagUp	$94.91358\% \pm 0.00067\%$
	$94.95\% \pm 0.14\%$	2012MagDown	$95.14769\% \pm 0.00063\%$
π_1^-	prod_ProbNN_π_K > 0.05	2011MagUp	$99.03074\% \pm 0.00099\%$
		2011MagDown	$99.01738\% \pm 0.00084\%$
	averaged efficiency	2012MagUp	$99.05534\% \pm 0.00037\%$
	$99.053\% \pm 0.041\%$	2012MagDown	$99.11022\% \pm 0.00035\%$
π_2^-	prod_ProbNN_π_K > 0.05	2011MagUp	$99.00463\% \pm 0.00091\%$
		2011MagDown	$99.02006\% \pm 0.00077\%$
	averaged efficiency	2012MagUp	$99.05060\% \pm 0.00036\%$
	$99.046\% \pm 0.047\%$	2012MagDown	$99.11059\% \pm 0.00035\%$
$K^-(\overline{K}^{*0})$	PIDK > 3 and	2011MagUp	$90.8406\% \pm 0.0017\%$
	prod_ProbNN_K_$\pi > 0.05$	2011MagDown	$90.5891\% \pm 0.0014\%$
	averaged efficiency	2012MagUp	$89.86056\% \pm 0.00064\%$
	$90.38\% \pm 0.43\%$	2012MagDown	$90.21170\% \pm 0.00060\%$
$\pi^+(\overline{K}^{*0})$	PIDK < 3 and	2011MagUp	$92.0149\% \pm 0.0016\%$
	prod_ProbNN_π_K > 0.05	2011MagDown	$91.9749\% \pm 0.0013\%$
	averaged efficiency	2012MagUp	$92.74198\% \pm 0.00061\%$
	$92.47\% \pm 0.57\%$	2012MagDown	$93.14965\% \pm 0.00057\%$

Table 13: Efficiencies of PID cuts.

5 Offline Selection using two BDTs and Rectangular Cuts

The cut-based offline selection delivers clear signal peaks of Λ_c^+, D^-, $\overline{K}^{*0}$ and Λ_b^0 (see section 4.2). However, the number of event passing the selection is not quite enough for the 2D mass fits, which are supposed to reduce the statictical error. In this section, an alternative to the purely cut-based offline selection, a selection using two BDTs and rectangular cuts, is described. The selection returns more availabe number of event for mass fits, which is expected to decrease the statistical error. The selection starts with the identification of the two open-charm intermediate particle, using BDTs trained on real data. The strategy for the selection is the same as for the cut-based selection: to obtain clear signal peaks of Λ_c^+, D^- and $\overline{K}^{*0}$ and then Λ_b^0.

5.1 Selection of Λ_c^+ and D^- using BDTs

BDT is a multivariate analysis technique using supervised machine learning. Two boosted decision trees, termed *D-from-B* BDTs, are applied for the selection of the two open-charm[18] intermediate particles Λ_c^+ and D^- decaying from Λ_b^0. BDT based selection is far more powerful than traditional, one-dimensional cut based methods [73]. These two BDTs are trained on data of the decays $\Lambda_b^0 \to \Lambda_c^+\pi^-$ and $B^0 \to D^-\pi^+$ by year, to identify their decays into final-state particles $\Lambda_c^+ \to p^+K^-\pi^+$ and $D^- \to K^+\pi^-\pi^-$. The software framework for the implementation of the two BDTs is developed by the Heidelberg LHCb group and is available in Gitlab repositories [74, 75].

The Λ_c^+ BDT is fully explained in [49]. The training of D^- BDT is briefly describe in the following. The decay channel $B^0 \to D^-\pi^+$ is used for the training of the BDT. The online and offline selection of the decay $B^0 \to D^-\pi^+$ is similar to those mentioned in section 5 in [49]. 2D mass fits are then applied to B^0 and D^-, to get the ${}_sWeight$s for the signal yields. Plots of the 2D mass fits are shown in Figure 20. A classifier using 69 discriminating variables is trained on sweighted training sample by years using the TMVA package embedded in the ROOT framework [76], including β (momentum asymmetry, see [53]), FDCHI2_OWNPV (χ^2 of the flight distance of a particle related to the primary vertex), IPCHI2_OWNPV, kinematic varialbes (e.g. p and p_{T}) (see section 4.1 and 4.2) and a set of boolean variables provided by the VELO, the RICH detectors and the muon stations, of D^- and its final-state particles. A testing sample is created to control potential over-training of the BDT. The BDT response to the testing sample should match the BDT response to the training sample [73]. Shown in Figure 21, it can be seen that the BDT responses to the training sample and the testing sample match very well. The trained BDT is applied to the signal decay $\Lambda_b^0 \to \Lambda_c^+ D^- \overline{K}^{*0}$, to extract the one-dimensional BDT response, which is dependent on the 69 discriminating varialbes of different degrees. A single cut on the BDT response can be applied to control the strictness of the selection for D^-. The response of the Λ_c^+ BDT is obtained in the same way.

The optimization of the cuts on the two BDT responses naturally becomes a task. However, with only cuts on the two BDT responses cannot deliver clear Λ_b^0 signal shape. A clear $\overline{K}^{*0}$ signal peak is still necessary to get a clear Λ_b^0 signal shape. The optimization will be performed later.

5.2 Cut-based Selection of $\overline{K}^{*0}$ and Λ_b^0

Based on the result from the cut-based selection (see section 4.2), the cuts on the final-state particles K^- and π^+ from $\overline{K}^{*0}$ listed in Table 5 are enough to get a clear $\overline{K}^{*0}$ signal peak. Two cuts to control the reconstruction quality

[18] This term is used to describe particle with quantum number $c \neq 0$

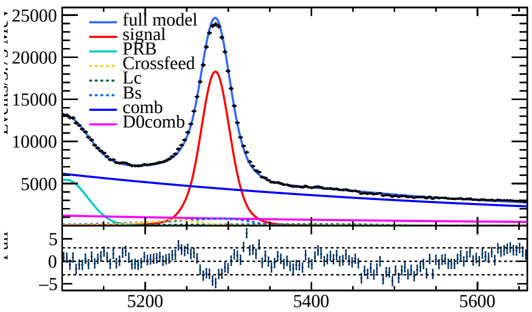

(a) 2011 B^0 mass fit.

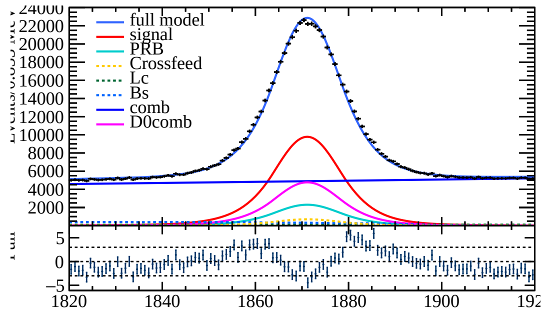

(b) 2011 D^- mass fit.

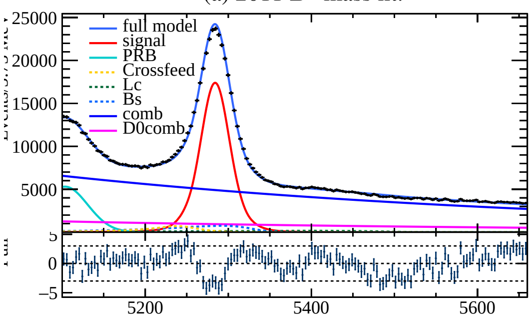

(c) 2012 B^0 mass fit.

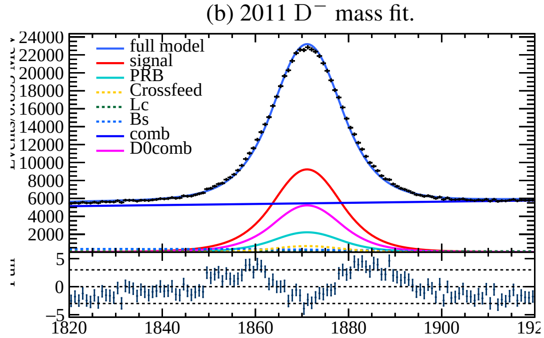

(d) 2012 D^- mass fit.

Figure 20: Projections of the 2D mass fits in B^0 and D^- masses for 2011 and 2012.

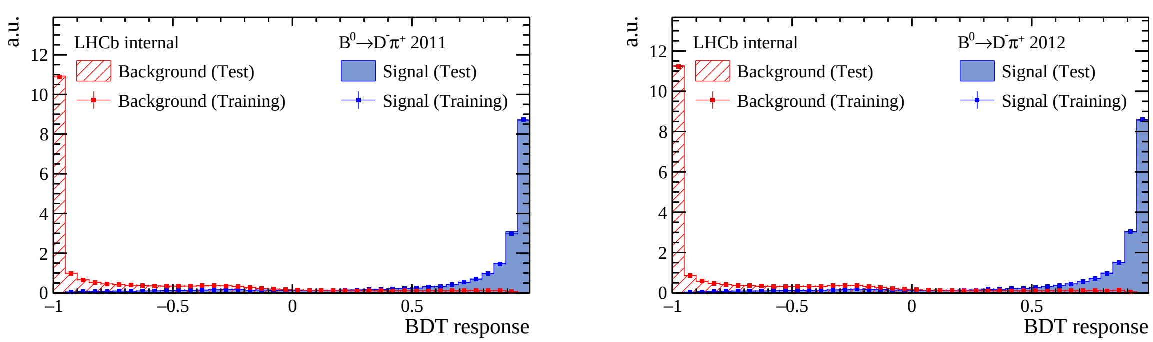

Figure 21: Distribution of D^-BDT reponses to the tesing sample and the training sample in 2011 (left) and 2012 (right).

of Λ_b^0 and $\overline{\mathrm{K}}^{*0}$ decay vertices are applied. The cuts on prod_ProbNN variables and pseudorapidities can be omitted to increase the number of events passing the selection. To get Λ_b^0 signal peak, mass cuts on Λ_c^+, D^- and $\overline{\mathrm{K}}^{*0}$ are needed. The applied rectangular cuts are listed in Table 14.

cuts	Λ_b^0	Λ_c^+	D^-	$\overline{K}^{0*}$	K^-	π^+
M/MeV	/	(2256,2316)	(1829,1909)	(700,1000)	/	/
p_T/MeV	/	/	/	/	> 400	> 150
$\text{ENDVERTEX}_{\chi^2/\text{ndf}}$	< 4	/	/	< 4	/	/
PIDK	/	/	/	/	> 3	< 3

Table 14: Applied cuts for $\overline{K}^{0*}$ and Λ_b^0 selection.

5.3 Optimization of the two BDT Responses

The cuts listed in Table 14, excecpt the mass cuts are applied for the optimization, so that with cuts on the two BDT responses a clear Λ_b^0 peak can be seen. The strategy is to find a combination of the two cuts on the BDT responses, with which the figure of merit (FoM), defined as

$$\text{FoM} := \frac{N}{\sqrt{N+S}},$$

where N and S are the signal and background yields returned from one-dimensional fits to Λ_b^0 mass in the range $[5560\,\text{MeV}, 5680\,\text{MeV}]$. A scan of the two BDT responses in the region $[-0.2, 0.8] \times [-0.5, 0.5]$ in 0.05 step along each axis is conducted. The optimization is separately done for 2011 and 2012 data, since the BDT trainings are divide by years. Here the fits are performed to the whole 2011 and 2012 data. A k-fold cross-validation can be done to avoid observer bias. 2D plots for the optimization for the year 2011 and 2012 are shown in Figure 22. The maximal figure of merit for 2011 data is found for the cuts $\Lambda_c^+\text{BDT} > 0.65$ and $D^-\text{BDT} > -0.3$; for 2012 data $\Lambda_c^+\text{BDT} > 0.5$ and $D^-\text{BDT} > -0.2$. It can be seen that for both 2011 and 2012 data, the figure of merit has relatively large values around the absolute maxima. While tightening up the cuts on both the BDT responses increases the figure of merit, however, too strict cuts cause a drop in FoM. For the simplicity, a common combination $\Lambda_c^+\text{BDT} > 0.5$ and $D^-\text{BDT} > -0.35$ is chosen. It needs to emphasized that the optimization done here is based on other fixed cuts that are already applied. As an improvement, other retangular cuts can be optimized with the cuts on the BDT responses, with k-fold cross-validation. This process will consume much longer time.

5.4 Misidentification Control

Same procedure used in section 4.3 can be used to control misidentification backgrounds. 2D plots invariant mass and momentum asymmetry of different final-state particles containing possible misidentification backgrounds are shown in Figure 23. The bands in Figure 23 (a), (c) and (e) corresponding to resonances formed by different final-state particles that ressemble Λ_c^+. The band in Figure 23 (g) correspond to undesirable $\overline{K}^{0*}$ formed by π^+ from Λ_c^+ and K^- from $\overline{K}^{0*}$. These obvious bands are vetoed, shown also in Figure 23. All cuts applied are listed in Table

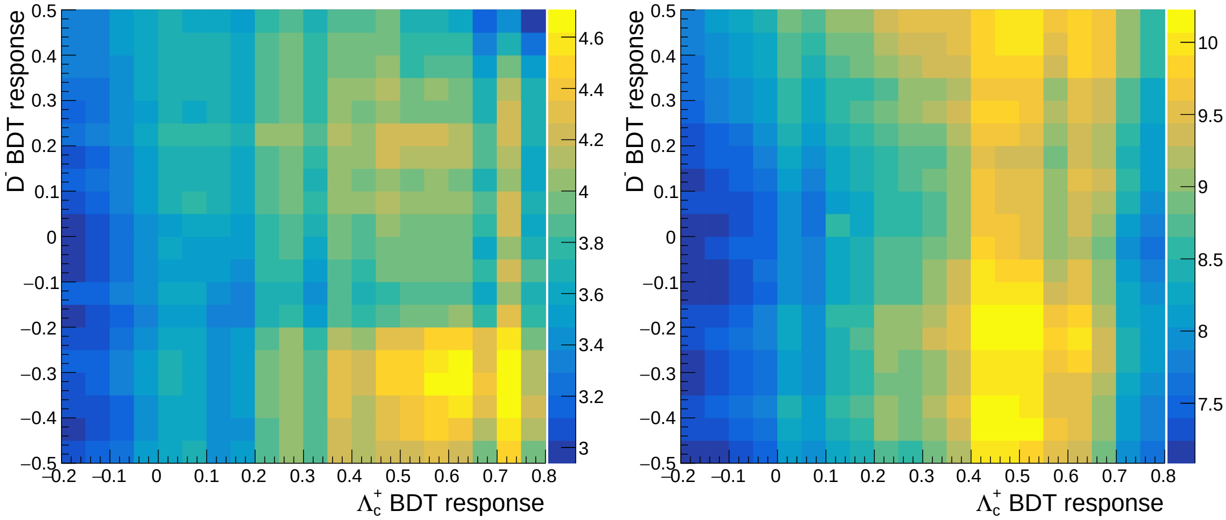

Figure 22: Optimization of the two BDT reponses for 2011 (left) and 2012 data (right).

15. The signal peaks of Λ_c^+, D^-, $\overline{K}^{0*}$[19] and Λ_b^0 are shown in Figure 24.

type	variable	range/cut
BDT response	Λ_c^+BDT	> 0.5
	D^-BDT	> -0.35
kinematics	$p_{T,K^\pm}$	$> 400\,\text{MeV}$
	$p_{T,\pi^\pm}$	$> 150\,\text{MeV}$
PID	$\text{PIDK}_{K^-(\overline{K}^{*0})}$	> 3
	$\text{PIDK}_{\pi^+(\overline{K}^{*0})}$	< 3
reconstruction	$\text{ENDVERTEX}_{\chi^2/\text{ndf},\overline{K}^{0*},\Lambda_b^0}$	< 4
veto	(β_{128}, M_{128})	$\notin (-0.5, 0.5) \times (2274\,\text{MeV}, 2298\,\text{MeV})$
	(β_{137}, M_{137})	$\notin (-0.4, 0.5) \times (2274\,\text{MeV}, 2298\,\text{MeV})$
	(β_{178}, M_{178})	$\notin (-0.3, 0.55) \times (2274\,\text{MeV}, 2298\,\text{MeV})$
	(β_{37}, M_{37})	$\notin (-1.0, 0.3) \times (880\,\text{MeV}, 910\,\text{MeV})$
mass	$m_{\Lambda_c^+}$	$\in (2256\,\text{MeV}, 2316\,\text{MeV})$
	m_{D^-}	$\in (1829\,\text{MeV}, 1909\,\text{MeV})$
	$m_{\overline{K}^{*0}}$	$\in (700\,\text{MeV}, 1000\,\text{MeV})$

Table 15: All applied cuts in the selection.

[19] show the full spectra the mass cuts are not applied.

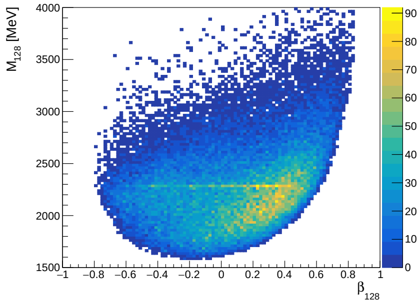

(a) Invariant mass of p^+, $K^-_{\Lambda_c^+}$ and $\pi^+_{\overline{K}^{*0}}$ against momentum asymmetry without veto cut.

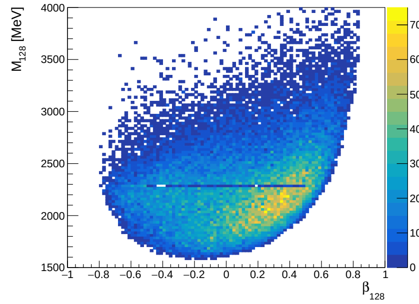

(b) Invariant mass of p^+, $K^-_{\Lambda_c^+}$ and $\pi^+_{\overline{K}^{*0}}$ against momentum asymmetry with veto cut.

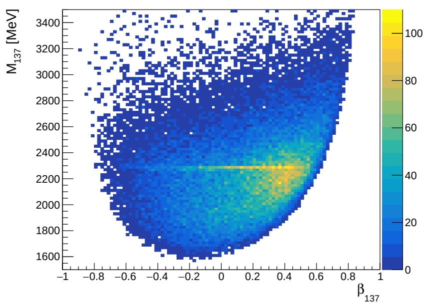

(c) Invariant mass of p^+, $\pi^+_{\Lambda_c^+}$ and $K^-_{\overline{K}^{*0}}$ against momentum asymmetry without veto cut.

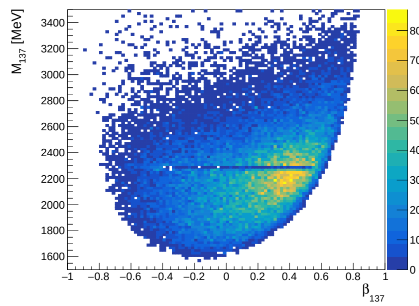

(d) Invariant mass of p^+, $\pi^+_{\Lambda_c^+}$ and $K^-_{\overline{K}^{*0}}$ against momentum asymmetry with veto cut.

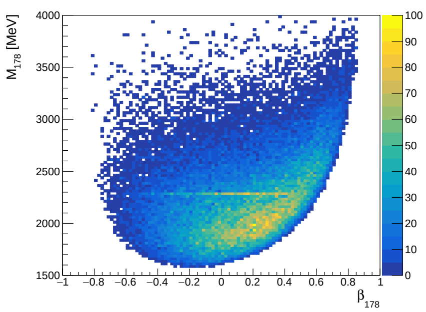

(e) Invariant mass of p^+, $K^-_{\overline{K}^{*0}}$ and $\pi^+_{\overline{K}^{*0}}$ against momentum asymmetry without veto cut.

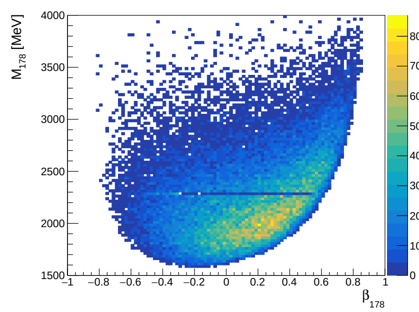

(f) Invariant mass of p^+, $K^-_{\overline{K}^{*0}}$ and $\pi^+_{\overline{K}^{*0}}$ against momentum asymmetry with veto cut.

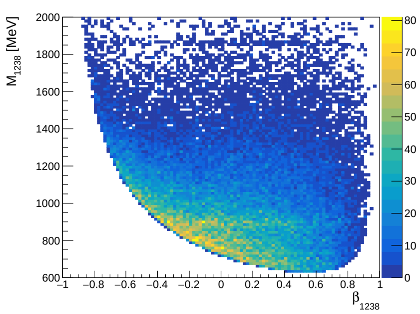

(g) Invariant mass of p^+, $K^-_{\overline{K}^{*0}}$ and $\pi^+_{\overline{K}^{*0}}$ against momentum asymmetry without veto cut.

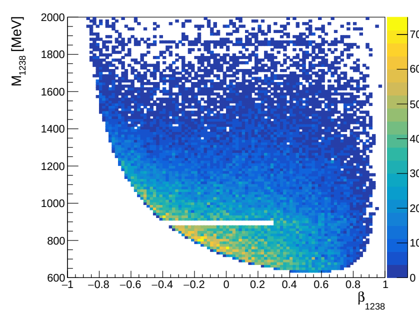

(h) Invariant mass of p^+, $K^-_{\overline{K}^{*0}}$ and $\pi^+_{\overline{K}^{*0}}$ against momentum asymmetry with veto cut.

Figure 23: Misidenfication control before and after veto cuts.

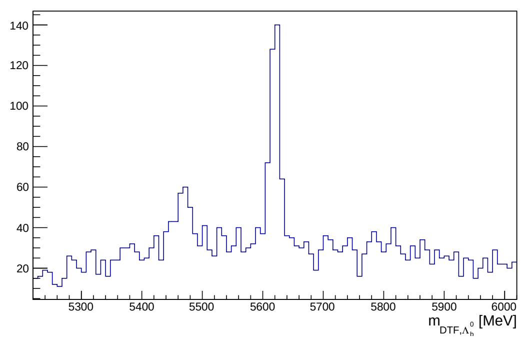

(a) Λ_b mass after selection.

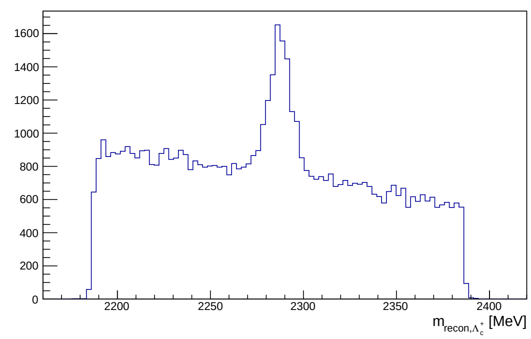

(b) Λ_c^+ mass after selection.

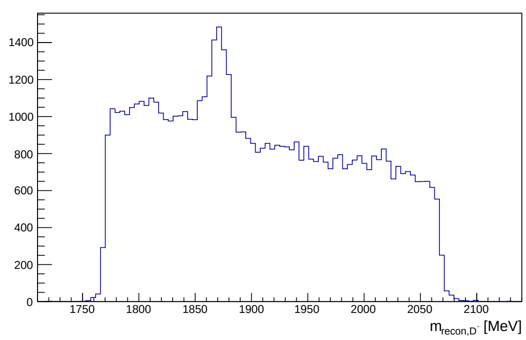

(c) D^- mass after selection.

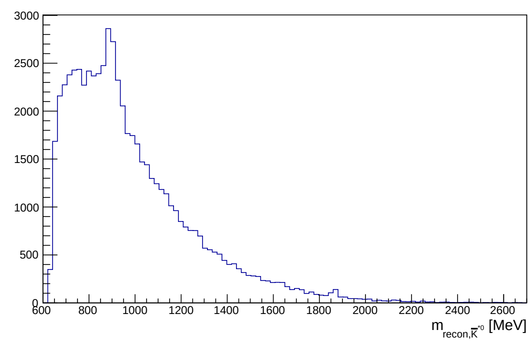

(d) $\overline{\mathrm{K}}^{*0}$ mass after selection.

Figure 24: Mass spectra of Λ_b^0, Λ_c^+, D^- and $\overline{\mathrm{K}}^{*0}$ after the selection.

5.5 Quality Control of the Selection

A mass cut of $30\,\mathrm{MeV}$ around the Λ_{b}^{0} PDG mass is applied while dropping the mass cut on one of the three intermediate particles is dropped (mass cuts on the other two maintained), to exmaine if the selected Λ_{c}^{+}, D^{-} and $\overline{\mathrm{K}}^{0*}$ are indeed coming from Λ_{b}^{0}. Three mass spectra returned from the procedure are given in Figure 25. It can be clear seen that the reconstructed Λ_{c}^{+}, D^{-} and $\overline{\mathrm{K}}^{0*}$ do come from Λ_{b}^{0}. Like in section 4.3, to rule out the decay $\Lambda_{\mathrm{b}}^{0} \rightarrow [\Lambda_{\mathrm{c}}^{+}\pi^{+}]_{\Sigma_{\mathrm{c}}^{++}}\mathrm{D}^{-}\mathrm{K}^{-}$, which could be reconstructed as the signal decay, where the π^{+} from $\overline{\mathrm{K}}^{*0}$ and the Λ_{c}^{+} decay from a Σ_{c}^{++}, the 2D plot of M_{1238} against β_{1238} need to be checked. Shown in Figure 26, no clear structure is seen.

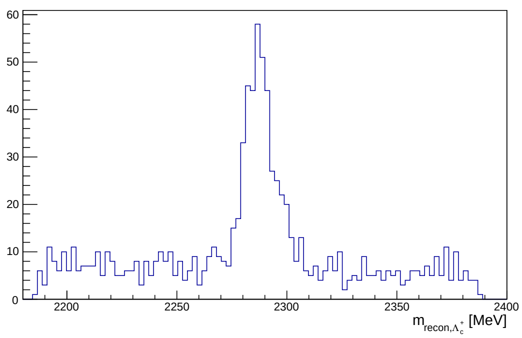

(a) Λ_{c}^{+} peak.

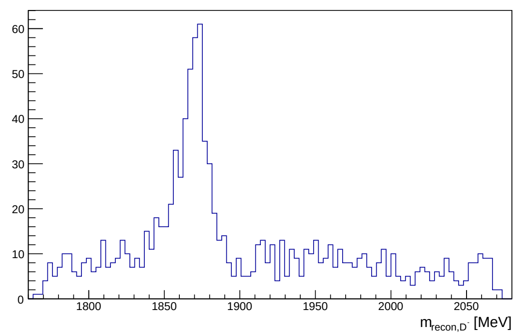

(b) D^{-} peak.

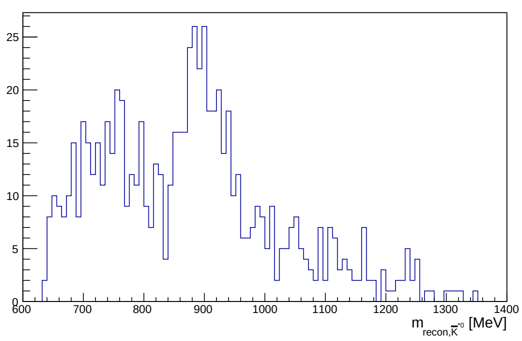

(c) $\overline{\mathrm{K}}^{*0}$ peak.

Figure 25: Signal peaks of the three intemediate particles.

6 Mass Fits

It is concluded in section 4.4 that the main contribution to signal peak, besides the signal decay, is from the decay $\Lambda_{\mathrm{b}}^{0} \rightarrow \Lambda_{\mathrm{c}}^{+}\mathrm{D}^{-}[\mathrm{K}^{-}\pi^{+}]$. Thus 2D mass fits is adequate to isolate this decay from the signal decay $\Lambda_{\mathrm{b}}^{0} \rightarrow \Lambda_{\mathrm{c}}^{+}\mathrm{D}^{-}\overline{\mathrm{K}}^{*0}$. Exactly the same fit procedure performed in section 4.4.3 can be used to fit the data passing the selection using two

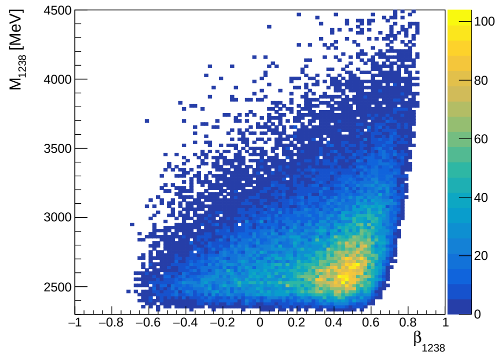

Figure 26: Check for potential resonance of Σ_{c}^{++}.

BDTs along with other rectangular cuts (see Table 15), described in section 5.

Since the selection is different from the previous cut-based selection, the MC data, which is cut the same way as the data, is different. The two BDTs are also applied to the MC data, to get the BDTs responses, so that the cuts on the BDT responses applied to the real data can also be applied to the MC data. Despite the difference of the MC data, the p.d.f.s used to fit the signal shapes of Λ_{b}^0, Λ_{c}^+, D^- and $\overline{\mathrm{K}}^{*0}$ are the same (see section 4.4). The Λ_{b}^0 shape is fit with a double Crystall Ball function defined in Eq. 3. The signal shapes of Λ_{c}^+ and D^- are fit with double Gaussian functions defined in Eq. 5. The $\overline{\mathrm{K}}^{*0}$ signal shape is fit with the sum of a Crystall Ball function and a Gaussian function, defined in Eq. 9. Plots of the fits to the signal shapes in the MC data are shown in Figure 27. Fit results are listed in Table 16.

fit parameter	Λ_{b}^0	Λ_{c}^+	D^-	$\overline{\mathrm{K}}^{*0}$
r_{CB}	0.517 ± 0.020	/	/	/
α	1.401 ± 0.074	/	/	-0.77 ± 0.22
n	2.41 ± 0.28	/	/	0.96 ± 0.75
σ	$5.820 \pm 0.087\,\mathrm{MeV}$	/	/	$29.4 \pm 2.0\,\mathrm{MeV}$
Γ	/	/	/	$47.07 \pm 0.49\,\mathrm{MeV}$
r_{BW}	/	/	/	0.765 ± 0.030
r_{G}	/	0.817 ± 0.025	0.824 ± 0.015	/
r_{σ}	/	2.160 ± 0.077	3.39 ± 0.23	/

Table 16: Fit parameters returned from the fits to Λ_{b}^0, Λ_{c}^+, D^- and $\overline{\mathrm{K}}^{*0}$ signal shapes in the MC data.

Fit parameters listed in Table 16 are fixed for the 2D mass fits[20]. The total p.d.f. defined in Eq. 12 is used to fit Λ_{b}^0 mass in the range $[5560\,\mathrm{MeV}, 5680\,\mathrm{MeV}]$. Plots from the 2D mass fits are shown in Figure 28. The fit result is given in Table 17.

From the fit result, the signal yield are 134 ± 22. The means of the masses of Λ_{b}^0 and $\overline{\mathrm{K}}^{*0}$ are both in 1σ accordance

[20]The parameter $\sigma_{\Lambda_{\mathrm{b}}^0}$ is not fixed. It will be used to be compared with the resolution of Λ_{b}^0 related to the signal decay in the 2D mass fits.

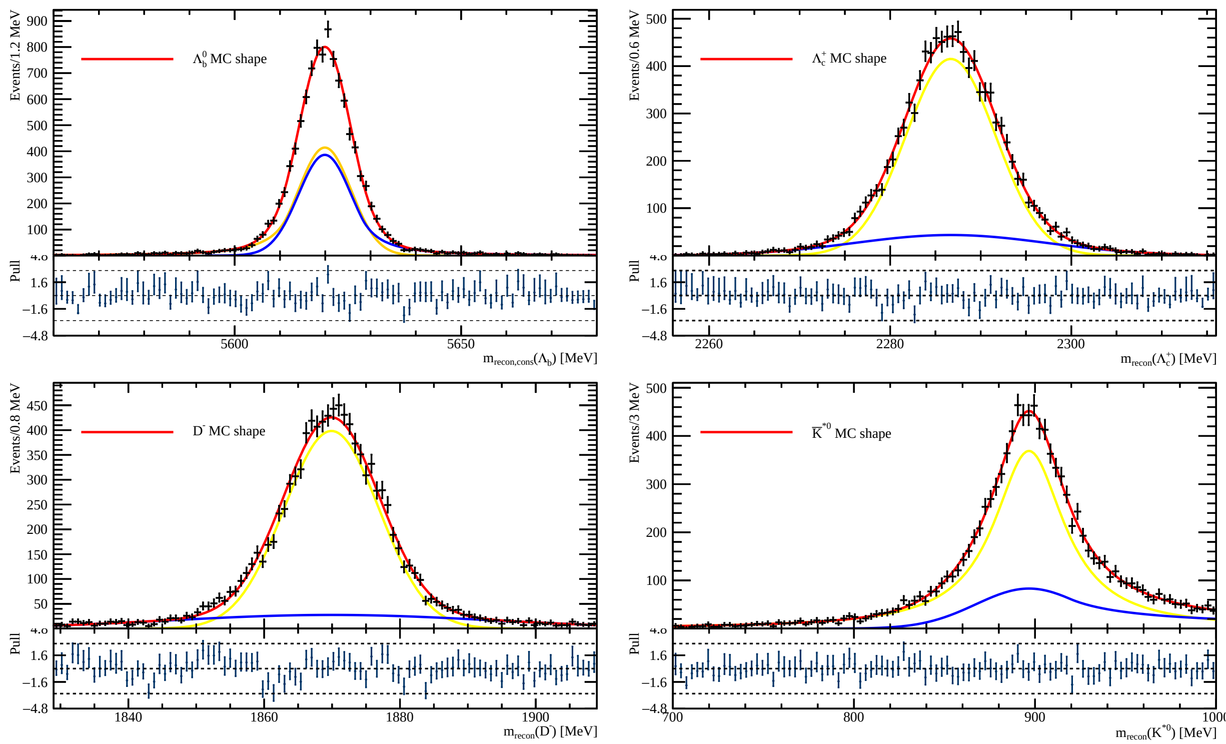

Figure 27: Fits to the shapes of Λ_b^0, Λ_c^+, D^- and $\overline{K}^{*0}$ in the MC data.

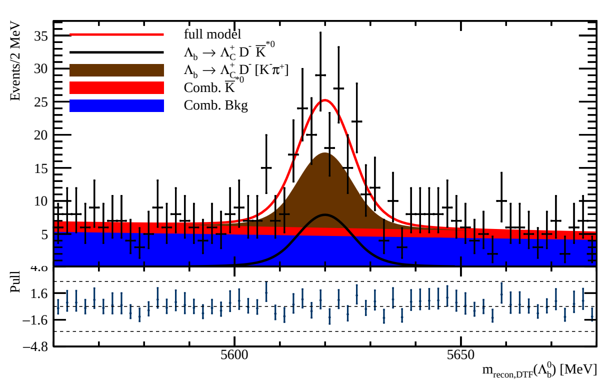

(a) Λ_b spectrum from the 2D fits.

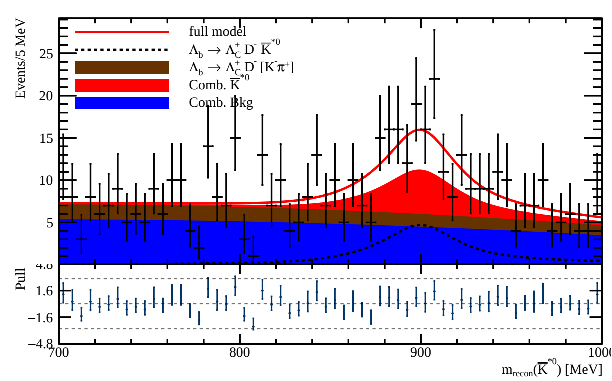

(b) $\overline{K}^{*0}$ spectrum from the 2D fits.

Figure 28: Projections of the 2D mass fits into Λ_b^0 and $\overline{K}^{*0}$ spectra.

fit parameter	Λ_b^0	$\overline{K}^{*0}$
μ/MeV	5620.20 ± 0.67	896 ± 4.1
σ/MeV	7.48 ± 0.67	/
a	-0.054 ± 0.082	-0.285 ± 0.089
b	/	-0.016 ± 0.086
$N_{\Lambda_b^0 \to \Lambda_c^+ D^- \overline{K}^{*0}}$	134 ± 22	
$N_{\Lambda_b^0 \to \Lambda_c^+ D^- [K^- \pi +]}$	169 ± 28	
N_{Bkg}	471 ± 29	
$r_{\overline{K}^{*0},\mathrm{Comb}}$	0.043 ± 0.059	

Table 17: Fit parameters for Λ_b^0 and $\overline{K}^{*0}$ from the 2D mass fits.

with the PDG masses. The resolution of Λ_b^0 mass related to the signal decay is in 3σ accordance of the resolution from the fit to the MC data. The yields of the decay $\Lambda_b^0 \to \Lambda_c^+ D^- [K^- \pi^+]$ is 169 ± 28.

7 Efficiency Study

An efficiency study is conducted, to get the efficiency corrected signal yields from the 2D mass fits (see section 6). The efficiency of detector acceptance, trigger, reconstruction and stripping (denoted by ϵ_{ARTS}) is already calculated in section 4.5.1. The efficiency of the offline selection using two BDTs and rectangular cuts is calculated in the following, including PID efficiency (ϵ_{PID}), efficiency of the cuts on the BDT responses (ϵ_{BDT}), efficiency of cuts related to kinematics and reconstruction quality of decay vertices (ϵ_{kin}), efficiency of the veto cuts (ϵ_{veto}) and efficiency of the mass cuts (ϵ_{mass}). The efficiencies are extracted from the fully detector simulated MC data. It is assumed that the MC data can describe the real data perfectly. All efficiency calculations use the formular given in Eq. 13. The total efficiency is given as

$$\epsilon_{\mathrm{tot}} \coloneqq \epsilon_{\mathrm{ARTS}} \cdot \epsilon_{\mathrm{PID}} \cdot \epsilon_{\mathrm{BDT}} \cdot \epsilon_{\mathrm{kin}} \cdot \epsilon_{\mathrm{veto}} \cdot \epsilon_{\mathrm{mass}}, \tag{16}$$

with the Gaussian error propagation

$$\Delta_{\epsilon_{\mathrm{tot}}} = \prod_{i \in I} \epsilon_i \cdot \sqrt{\sum_{i \in I} \left(\frac{\Delta_{\epsilon_i}}{\epsilon_i} \right)^2}, \text{ with } I \coloneqq \{\mathrm{ARTS, PID, BDT, kin, veto, mass}\}. \tag{17}$$

The total efficiency is calculated as $\epsilon_{\mathrm{tot}} = 1.15\% \pm 0.19\%$, using the result $\epsilon_{\mathrm{ARTS}} = 4.17\% \pm 0.56\%$ from section 4.5.1. Detailed calculations are explained in the following.

7.1 PID Efficiency

Two PID cuts are applied in the selection: $\mathrm{PIDK}\left(\mathrm{K}^{-}_{\overline{\mathrm{K}}^{*0}}\right) > 3$ and $\mathrm{PIDK}\left(\pi^{+}_{\overline{\mathrm{K}}^{*0}}\right) < 3$. The efficiency of these two cuts is calculated by the PIDCalib package from its calibration samples, using a customed binning scheme[21] for three default kinematic variables, p (momentum), η (pseudorapidity) and $\mathrm{nTracks}$ (track multiplicity). These kinematic variables are chosen for the calibration because the tracking and reconstruction efficiency of the RICH detectors and the tracking stations depends on these variables [77, 78, 79]. As mentioned before, the PID efficiency is calculated by year and magnet polarity for the MC data, listed in Table 19. PID weights are assigned to each event in the MC data. These weights are applied to the MC data by year and magnet polarity and merged together by year before next steps. An averaged PID efficiencies are calculated for the two applied PID cuts. The total PID efficiency is given as the product of the two PID efficiencies, assuming the two are independent of each other, which takes the value $\epsilon_{\mathrm{PID}} = 83.78\% \pm 0.64\%$.

particle	PID cut	dataset	efficiency
$\mathrm{K}^{-}(\overline{\mathrm{K}}^{*0})$	$\mathrm{PIDK} > 3$ and	2011MagUp	$92.4056\% \pm 0.0015\%$
	$\mathrm{prod\_ProbNN\_K\_}\pi > 0.05$	2011MagDown	$92.1409\% \pm 0.0012\%$
	averaged efficiency	2012MagUp	$91.13478\% \pm 0.00057\%$
	$90.38\% \pm 0.43\%$	2012MagDown	$91.47469\% \pm 0.00053\%$
$\pi^{+}(\overline{\mathrm{K}}^{*0})$	$\mathrm{PIDK} < 3$ and	2011MagUp	$92.2277\% \pm 0.0013\%$
	$\mathrm{prod\_ProbNN\_}\pi\mathrm{\_K} > 0.05$	2011MagDown	$92.2500\% \pm 0.0015\%$
	averaged efficiency	2012MagUp	$92.97554\% \pm 0.00057\%$
	$92.70\% \pm 0.56\%$	2012MagDown	$93.37284\% \pm 0.00053\%$

Table 18: Efficiencies of the two PID cuts.

7.2 BDT Efficiency

Efficiency lookup tables are created from the training samples by year, the data of the decay $\Lambda^0_\mathrm{b} \to \Lambda^+_\mathrm{c}\pi-$ for the cut $\Lambda^+_\mathrm{c}\mathrm{BDT} > 0.5$ and of the decay $\mathrm{B}^0 \to \mathrm{D}^-\pi+$ for $\mathrm{D}^-\mathrm{BDT} > -0.35$, shown in Figure 29. The 2D histograms use fixed binning scheme in variable $\log\left(\mathrm{FDCHI2\_OWNPV}_{\Lambda^+_\mathrm{c},\mathrm{D}^-}\right)$ and $\mathrm{nTrakcs}$. The bin boundries are chosen to make the number of event roughly the same in each bin. The efficiency of the two cuts are calculated separately for the MC data (with PID weights applied) in the following way. The sweighted data from the fits in the training procedure (see section 5.1) with and without one of the two BDT response cuts is arranged in the 2D histogram. In each bin, one-dimensional mass fits to Λ^0_b (for $\Lambda^+_\mathrm{c}\mathrm{BDT}$) or B^0 (for $\mathrm{D}^-\mathrm{BDT}$) before after the cut are performed to get the signal yields N_{before} and N_{after}. The efficiency of the cut in this bin is then, according to Eq. 13, $\epsilon\left(\mathrm{cut},\mathrm{bin}\right) = \frac{N_{\mathrm{after}}}{N_{\mathrm{before}}}$[22].

[21] The binning for p is $[0, 260000\,\mathrm{MeV}]$ with bin boundries $15000\,\mathrm{MeV}$ and $30000\,\mathrm{MeV}$, for η $[1.0, 5.5]$ with bin boundries 3.0 and 3.5 and for $\mathrm{nTracks}$ $[0, 800]$ with bin boundries 130 and 200.

[22] The error can be calculated with the Poisson error. However, it is expected that the Poisson error is at least one order smaller than the statistical error of the averaged efficiency for all bins. The calculation for the error of the efficiency in each bin is thus omitted.

Each event in the MC data is then arranged in the same binning scheme and is assigned with the efficiency of that bin it is in. The efficiency for each event is applied to the MC data by year as a weight. The averaged efficiency is calculated from the efficiencies of each bin and used as the efficiency for a single BDT response cut. In this analysis, the efficiency weights of $\Lambda_c^+ \mathrm{BDT}$ are applied to the MC data by year at first. The efficiency weights of $\mathrm{D}^- \mathrm{BDT}$ are then applied to the MC data (with $\Lambda_c^+ \mathrm{BDT}$ efficiency weights) by year, assuming the two BDT responses are independent. Finally the two sets of weighted MC data by year are merged together to get the efficiency of the other cuts. The averaged $\Lambda_c^+ \mathrm{BDT}$ and $\mathrm{D}^- \mathrm{BDT}$ are listed in Table 19. The total BDT efficiency of the two cuts is then the product of the two averaged efficiencies, which takes the value $\epsilon_{\mathrm{BDT}} = 72.4\% \pm 7.2\%$.

BDT cut	$\Lambda_c^+ \mathrm{BDT}$	$\mathrm{D}^- \mathrm{BDT}$
2011 Efficiency	$76.9\% \pm 8.3\%$	$94.5 \pm 7.1\%$
2012 Efficiency	$75.9\% \pm 9.4\%$	$95.1 \pm 7.8\%$
averaged efficiency	$76.4\% \pm 6.3\%$	$94.8\% \pm 5.3\%$

Table 19: Efficiencies of the two BDT response cuts.

7.3 Efficiencis of Kinemtic and Decay Vertex Cuts, Veto Cuts and Mass Cuts

The distributions of the cuts, of which the efficiencies will be calculated, in the MC data are plotted against the distributions in the sweighted data from the 2D mass fits, shown in Figure 30. Almost all distributions match very well with each other. However, there is some discrepency between the distributions of $\mathrm{ENDVERTEX}_{\chi^2/ndf,\Lambda_b^0}$. The distribution in the MC data is shifted to the left. It is expected that the influence of this shift on the total efficiency is small. No weighting of the MC data is conducted to make it match the sweighted data in $\mathrm{ENDVERTEX}_{\chi^2/ndf,\Lambda_b^0}$.

The efficiency of kinematic and decay vertex cuts is obtained, by comparing the number of event in the weighted MC data before and after applying the cuts. The efficiency is calculated as $\epsilon_{\mathrm{kin}} = 74.36\% \pm 0.59\%$, with the Poisson error. Similarly, The efficiencies of veto cuts and mass cuts are $\epsilon_{\mathrm{veto}} = 87.95\% \pm 0.77\%$ and $\epsilon_{\mathrm{mass}} = 69.76\% \pm 0.69\%$.

8 Results

With the signal yields from the 2D mass fits $N_{\Lambda_b^0 \to \Lambda_c^+ \mathrm{D}^- \overline{\mathrm{K}}^{*0}} = 134 \pm 22$ (see section 6) and the total efficiency $\epsilon_{\mathrm{tot}} = 1.15\% \pm 0.19\%$, the efficiency corrected signal yields can be calculated as $N_{\Lambda_b^0 \to \Lambda_c^+ \mathrm{D}^- \overline{\mathrm{K}}^{*0},\mathrm{corr}} = 8900 \pm 1900$. Compared with the efficiency corrected signal yields from the 2D mass fits to the data with cut-based selection $N'_{\Lambda_b^0 \to \Lambda_c^+ \mathrm{D}^- \overline{\mathrm{K}}^{*0},\mathrm{corr}} = 7400 \pm 2200$, the two results are in 1σ accordance, mainly due to their relatively large errors. A main contribution to the error is the statistical error of the signal yields from the 2D mass fits, which originates from the fit procedure. A huge challenge to the study of the signal decay $\Lambda_b^0 \to \Lambda_c^+ \mathrm{D}^- \overline{\mathrm{K}}^{*0}$ is that the number of event passing the offline selection is very limited, due to the difficulty of reconstructing such a decay with eight final-state

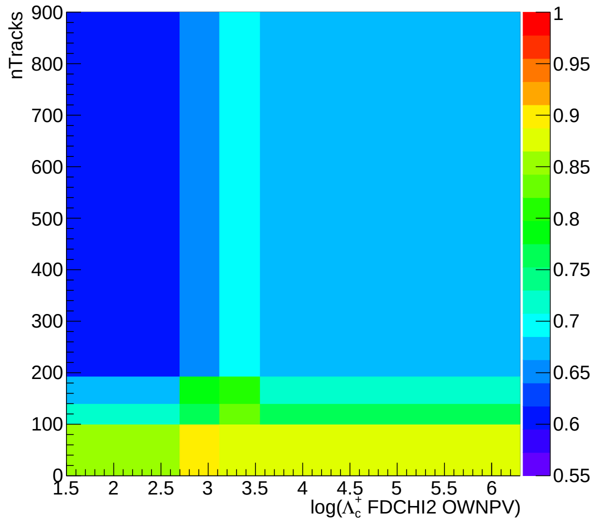

(a) 2011 Λ_c^+ BDT efficiency for $\Lambda_c^+\mathrm{BDT} > 0.5$.

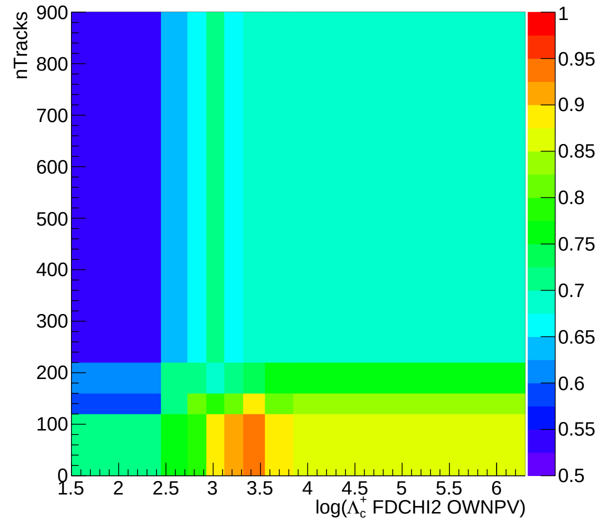

(b) 2012 Λ_c^+ BDT efficiency for $\Lambda_c^+\mathrm{BDT} > 0.5$.

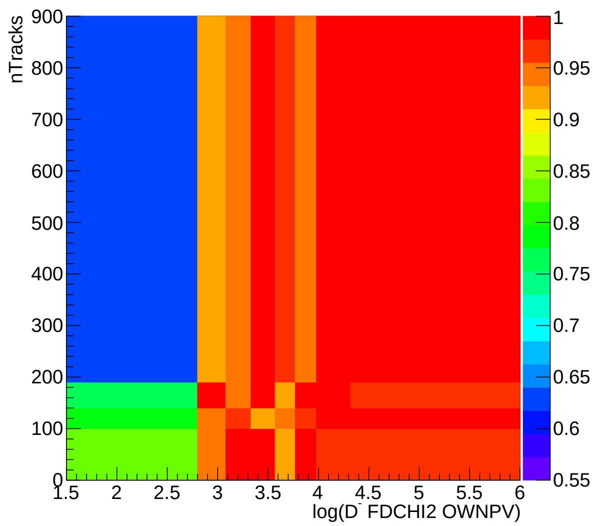

(c) 2011 D^- BDT efficiency for $\mathrm{D}^-\mathrm{BDT} > -0.35$.

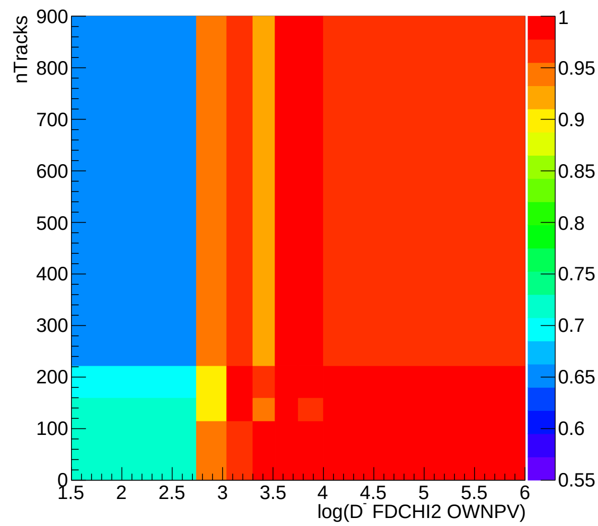

(d) 2012 D^- BDT efficiency for $\mathrm{D}^-\mathrm{BDT} > -0.35$.

Figure 29: BDT efficiency lookup tables for 2011 and 2012 with fixed binning scheme.

tracks. The backgrounds rejection becomes a huge task: On one hand backgrounds need to be suppressed, while on the other hand the backgrounds rejection needs to be efficient. Besides the two BDTs applied to identify non-prompt Λ_c^+ and D^-, a BDT for the selection of $\overline{\mathrm{K}}^{*0}$ coule be trained to replace the rectangular cuts. The number of events passing the selection could increase, and the statistical error from the fit procedure could be reduced. The fit model and fit method used in the fits can be improved. Another contraibution is the statistical error of the averaged efficiency of the

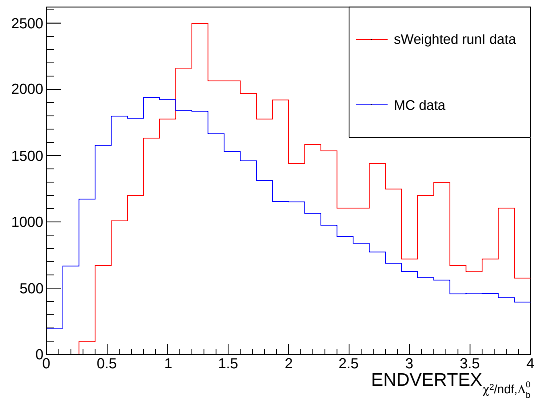

(a) Comparison of $\mathrm{ENDVERTEX}_{\chi^2/ndf,\Lambda_b^0}$ distributions.

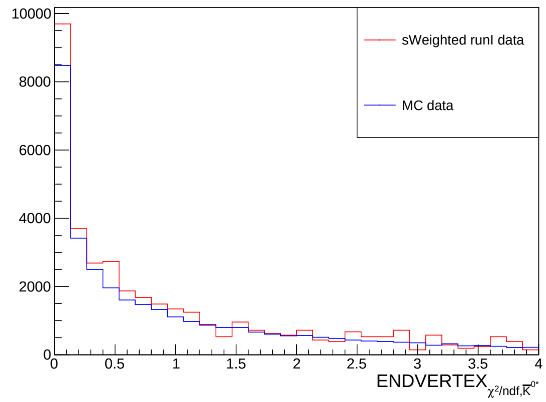

(b) Comparison of $\mathrm{ENDVERTEX}_{\chi^2/ndf,\overline{\mathrm{K}}^{*0}}$ distributions.

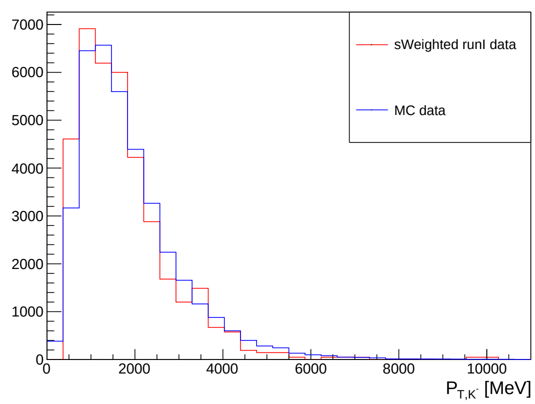

(c) Comparison of $p_{\mathrm{T,K^-}}$ distributions.

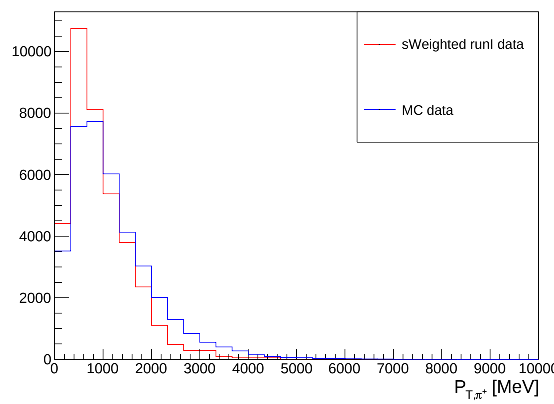

(d) Comparison of p_{T,π^+} distributions.

Figure 30: Comparison of $\mathrm{ENDVERTEX}_{\chi^2/ndf,\Lambda_b^0}$, $\mathrm{ENDVERTEX}_{\chi^2/ndf,\overline{\mathrm{K}}^{*0}}$, $p_{\mathrm{T,K^-}}$ and p_{T,π^+} distributions between the MC data and sweighted data.

two BDT response cuts, which is 1 order larger than the errors of other efficiencies (see section 7). A more advanced technique can be used to calculate the statistical error of the averaged BDT efficiency instead of the tradidional one.

Due to time limit, no study of systematic uncertainties is done to this analysis. Potential sources of systematic uncertainties are briefly listed below. It is expected that main systematic uncertainty comes from the MC data. It is assumed that the MC data matches the sweighted data perfectly. However this is not the case. For example, these is a discrepancy between the distributions of the varialbe $\mathrm{ENDVERTEX}_{\chi^2,\Lambda_b^0}$ in the MC data and the sweighted data (see section 7.3). As a consequence, the efficiencies extracted from the MC data will contain systematic errors. The binning scheme used to calculate PID efficiencies can be improved, since the MC data is not expected to contain correct $\mathrm{nTracks}$ information. The BDT efficiency is calculated with fixed binning scheme as an alternative to the adaptive binning scheme used by the software framework, which leaves systematic uncertatinty. The fit models and fit methods used in this analysis are also important sources, since varying fit models and changing fixed fit parameters will change the fit results. A toy-MC study can be conducted to the chosen fit model, to check potential bias. The choies of one-dimensional cuts used in the offline selection also give systematic uncertainty. Different optimization strategies for the cuts can bring different results. However, this effect is expected to be small.

9 Conclusion and Outlook

The first observation of the decay $\Lambda_b^0 \rightarrow \Lambda_c^+ D^- \overline{K}^{*0}$ and the measured efficiency corrected signal yields are presented in this thesis, using the runI data corresponding to an integrated luminosity of $3.0\,\mathrm{fb}^{-1}$ collected at center-of-mass colliding energies of $7\,\mathrm{TeV}$ and $8\,\mathrm{TeV}$ in 2011 and 2012 by the LHCb detector. The efficiency corrected signal yields are $N_{\Lambda_b^0 \rightarrow \Lambda_c^+ D^- \overline{K}^{*0},\mathrm{corr}} = 8900 \pm 1900$, where the error is the statistical one.

A study of systematic uncertainties still needs to be conducted to this analysis. The runII data, which corresponds to integrated luminosities of $328\,\mathrm{pb}^{-1}$ and $1665\,\mathrm{pb}^{-1}$ collected at $\sqrt{s} = 13\,\mathrm{MeV}$ in 2015 and 2016, can also be included, which is expected to at least double the number of events passing the offline selection. A branching fraction measurement with reference to the normalization channel $\Lambda_b^0 \rightarrow \Lambda_c^+ D_s^-$ can be performed. By using the same BDT repsonse cuts, the relatively large error of the averaged BDT efficiency can be cancelled, which will leads to better accuracy. With a well-measured branching fraction, an amplitude analysis can be done to the $\Lambda_c^+ D^-$ subsystem, for the search for neutral hidden charm pentaquarks with quark content $\mathrm{c\overline{c}udd}$.

References

[1] *External Software Frameworks*. https://gitlab.cern.ch/lhcb-bandq-exotics/Lb2LcD0K/tree/master/externals, Accessed: August 28, 2018.

[2] R. Aaij *et al.*, "Observation of $J/\psi p$ Resonances Consistent with Pentaquark States in $\Lambda_b^0 \to J/\psi K^- p$ Decays," *Phys. Rev. Lett.*, vol. 115, p. 072001, 2015.

[3] M. Thomson, *Modern particle physics*. New York: Cambridge University Press, 2013.

[4] G. Aad *et al.*, "Observation of a new particle in the search for the Standard Model Higgs boson with the ATLAS detector at the LHC," *Phys. Lett.*, vol. B716, pp. 1–29, 2012.

[5] S. Chatrchyan *et al.*, "Observation of a new boson at a mass of 125 GeV with the CMS experiment at the LHC," *Phys. Lett.*, vol. B716, pp. 30–61, 2012.

[6] M. E. Peskin and D. V. Schroeder, *An Introduction to quantum field theory*. Reading, USA: Addison-Wesley, 1995.

[7] I. J. R. Aitchison and A. J. G. Hey, *Gauge theories in particle physics: A practical introduction. Vol. 2: Non-Abelian gauge theories: QCD and the electroweak theory*. Bristol, UK: CRC Press, 2012.

[8] D. H. Perkins, *Introduction to high energy physics*. 1982.

[9] I. J. R. Aitchison and A. J. G. Hey, *Gauge theories in particle physics: A practical introduction. Vol. 1: From relativistic quantum mechanics to QED*. Bristol, UK: CRC Press, 2012.

[10] T. D. Lee and C. N. Yang, "Question of parity conservation in weak interactions," *Phys. Rev.*, vol. 104, pp. 254–258, Oct 1956.

[11] C. S. Wu, E. Ambler, R. W. Hayward, D. D. Hoppes, and R. P. Hudson, "Experimental test of parity conservation in beta decay," *Phys. Rev.*, vol. 105, pp. 1413–1415, Feb 1957.

[12] G. Arnison *et al.*, "Experimental Observation of Isolated Large Transverse Energy Electrons with Associated Missing Energy at s**(1/2) = 540-GeV," *Phys. Lett.*, vol. B122, pp. 103–116, 1983. [,611(1983)].

[13] M. Banner *et al.*, "Observation of Single Isolated Electrons of High Transverse Momentum in Events with Missing Transverse Energy at the CERN anti-p p Collider," *Phys. Lett.*, vol. B122, pp. 476–485, 1983. [,7.45(1983)].

[14] J. Albrecht *et al.*, "Performance of the LHCb High Level Trigger in 2012," *J. Phys. Conf. Ser.*, vol. 513, p. 012001, 2014.

[15] V. P. Andreev, "B production at the LHC / QCD aspects," in *Proceedings, 42nd Rencontres de Moriond on QCD and High Energy Hadronic Interactions: La Thuile, Italy, March 17-24, 2007*, pp. 103–106, 2007.

[16] I. Polyakov, "Heavy flavor production in the forward acceptance at the LHC," Jul 2015.

[17] E. L. Bratkovskaya *et al.*, "Heavy flavor in relativistic heavy-ion collisions," *J. Phys. Conf. Ser.*, vol. 668, no. 1, p. 012008, 2016.

[18] *The Large Hadron Collider*. https://home.cern/topics/large-hadron-collider, Accessed: August 28, 2018.

[19] R. Aaij *et al.*, "Prompt charm production in pp collisions at sqrt(s)=7 TeV," *Nucl. Phys.*, vol. B871, pp. 1–20, 2013.

[20] R. Aaij *et al.*, "Measurements of prompt charm production cross-sections in pp collisions at $\sqrt{s} = 5$ TeV," *JHEP*, vol. 06, p. 147, 2017.

[21] R. Lindner, "LHCb layout 2. LHCb schema 2." LHCb Collection., Feb 2008.

[22] P. R. Barbosa-Marinho *et al.*, *LHCb VELO (VErtex LOcator): Technical Design Report*. Technical Design Report LHCb, Geneva: CERN, 2001.

[23] P. Collins, "Overview diagram showing spacing of modules along Z, and positions open and closed." LHCb Collection.

[24] S. Amato *et al.*, *LHCb magnet: Technical Design Report*. Technical Design Report LHCb, Geneva: CERN, 2000.

[25] P. R. Barbosa-Marinho *et al.*, *LHCb inner tracker: Technical Design Report*. Technical Design Report LHCb, Geneva: CERN, 2002. revised version number 1 submitted on 2002-11-13 14:14:34.

[26] P. R. Barbosa-Marinho *et al.*, *LHCb outer tracker: Technical Design Report*. Technical Design Report LHCb, Geneva: CERN, 2001.

[27] S. Amato *et al.*, *LHCb RICH: Technical Design Report*. Technical Design Report LHCb, Geneva: CERN, 2000.

[28] P. A. Čerenkov, "Visible radiation produced by electrons moving in a medium with velocities exceeding that of light," *Phys. Rev.*, vol. 52, pp. 378–379, Aug 1937.

[29] M. Adinolfi *et al.*, "Performance of the LHCb RICH detector at the LHC," *Eur. Phys. J. C*, vol. 73, p. 2431. 25 p, Nov 2012.

[30] "Pictures, figures, and plots." LHCb Collection.

[31] S. Amato *et al.*, *LHCb calorimeters: Technical Design Report*. Technical Design Report LHCb, Geneva: CERN, 2000.

[32] P. R. Barbosa-Marinho *et al.*, *LHCb muon system: Technical Design Report*. Technical Design Report LHCb, Geneva: CERN, 2001.

[33] R. Antunes-Nobrega *et al.*, *LHCb trigger system: Technical Design Report*. Technical Design Report LHCb, Geneva: CERN, 2003. revised version number 1 submitted on 2003-09-24 12:12:22.

[34] A. A. Alves, Jr. *et al.*, "The LHCb Detector at the LHC," *JINST*, vol. 3, p. S08005, 2008.

[35] *Trigger system*. https://lhcb-public.web.cern.ch/lhcb-public/en/Data%20Collection/Triggers2-en.html, Accessed: August 28, 2018.

[36] S. Tolk *et al.*, "Data driven trigger efficiency determination at LHCb," Tech. Rep. LHCb-PUB-2014-039. CERN-LHCb-PUB-2014-039, CERN, Geneva, May 2014.

[37] M. Williams *et al.*, "The HLT2 Topological Lines," Tech. Rep. LHCb-PUB-2011-002. CERN-LHCb-PUB-2011-002, CERN, Geneva, Jan 2011.

[38] M. Patel, "An Inclusive ϕ Stream for the LHCb High Level Trigger," Tech. Rep. LHCb-2006-041. CERN-LHCb-2006-041, CERN, Geneva, Jul 2006.

[39] M. Gell-Mann, "A Schematic Model of Baryons and Mesons," *Phys. Lett.*, vol. 8, pp. 214–215, 1964.

[40] R. L. Jaffe, "Multi-Quark Hadrons. 1. The Phenomenology of (2 Quark 2 anti-Quark) Mesons," *Phys. Rev.*, vol. D15, p. 267, 1977.

[41] D. Strottman, "Multi - Quark Baryons and the MIT Bag Model," *Phys. Rev.*, vol. D20, pp. 748–767, 1979.

[42] K. H. Hicks, "On the conundrum of the pentaquark," *Eur. Phys. J.*, vol. H37, pp. 1–31, 2012.

[43] R. Aaij *et al.*, "Model-independent evidence for $J/\psi p$ contributions to $\Lambda_b^0 \to J/\psi p K^-$ decays," *Phys. Rev. Lett.*, vol. 117, p. 082002. 9 p, Apr 2016. 21 pages, 12 figures (including the supplemental section added at the end).

[44] R. Aaij *et al.*, "Amplitude analysis and branching fraction measurement of $\overline{b}_s^0 \to j/\psi K^+ K^-$," *Phys. Rev. D*, vol. 87, p. 072004, Apr 2013.

[45] R. Aaij *et al.*, "Study of the production of Λ_b^0 and $\overline{B}^0$ hadrons in pp collisions and first measurement of the $\Lambda_b^0 \to J/\psi p K^-$ branching fraction," *Chin. Phys. C*, vol. 40, p. 011001. 16 p, Sep 2015. 29 pages, 19figures. All figures and tables, along with any supplementary material and additional information, are available at https://lhcbproject.web.cern.ch/lhcbproject/Publications/LHCbProjectPublic/LHCb-PAPER-2015-032.html.

[46] L. Anderlini *et al.*, "The PIDCalib package," Tech. Rep. LHCb-PUB-2016-021. CERN-LHCb-PUB-2016-021, CERN, Geneva, Jul 2016.

[47] *StrippingLb2LcDKstBeauty2CharmLine(21r1)*. http://lhcbdoc.web.cern.ch/lhcbdoc/stripping/config/stripping21r1/bhadron/strippi Accessed: August 28, 2018.

[48] *StrippingLb2LcDKstBeauty2CharmLine(21)*. http://lhcbdoc.web.cern.ch/lhcbdoc/stripping/config/stripping21/bhadron/strippinglb Accessed: August 28, 2018.

[49] M. Stahl, *First observation of the decay $\Lambda_b^0 \to \Lambda_c^+ \overline{D}^{(*)0} K^-$ in preparation of a pentaquark search in the $\Lambda_c^+ \overline{D}^{(*)0}$ system at the LHCb experiment*. PhD thesis, Heidelberg University, Heidelberg, 2018.

[50] L. Anderlini *et al.*, "Computing strategy for PID calibration samples for LHCb Run 2," Tech. Rep. LHCb-PUB-2016-020. CERN-LHCb-PUB-2016-020, CERN, Geneva, Jul 2016.

[51] M. Tanabashi *et al.*, "Review of particle physics," *Phys. Rev. D*, vol. 98, p. 030001, Aug 2018.

[52] W. D. Hulsbergen, "Decay chain fitting with a Kalman filter," *Nucl. Instrum. Meth.*, vol. A552, pp. 566–575, 2005.

[53] M. Artuso *et al.*, "Measurement of the CP violating asymmetry a_{sl}^s," May 2016.

[54] G. A. Cowan *et al.*, "RapidSim: an application for the fast simulation of heavy-quark hadron decays," *Comput. Phys. Commun.*, vol. 214, pp. 239–246, 2017.

[55] K. S. Cranmer, "Kernel estimation in high-energy physics," *Comput. Phys. Commun.*, vol. 136, pp. 198–207, 2001.

[56] W. Verkerke and D. P. Kirkby, "The RooFit toolkit for data modeling," *eConf*, vol. C0303241, p. MOLT007, 2003. [,186(2003)].

[57] T. Sjostrand *et al.*, "PYTHIA 6.4 Physics and Manual," *JHEP*, vol. 05, p. 026, 2006.

[58] I. Belyaev *et al.*, "Handling of the generation of primary events in Gauss, the LHCb simulation framework," in *Proceedings, 2010 IEEE Nuclear Science Symposium and Medical Imaging Conference (NSS/MIC 2010): Knoxville, Tennessee, October 30-November 6, 2010*, pp. 1155–1161, 2010.

[59] S. Agostinelli *et al.*, "GEANT4: A Simulation toolkit," *Nucl. Instrum. Meth.*, vol. A506, pp. 250–303, 2003.

[60] J. Allison *et al.*, "Geant4 developments and applications," *IEEE Trans. Nucl. Sci.*, vol. 53, p. 270, 2006.

[61] M. Clemencic *et al.*, "The LHCb simulation application, Gauss: Design, evolution and experience," *J. Phys. Conf. Ser.*, vol. 331, p. 032023, 2011.

[62] D. J. Lange, “The EvtGen particle decay simulation package,” *Nucl. Instrum. Meth.*, vol. A462, pp. 152–155, 2001.

[63] J. E. Gaiser, *Charmonium Spectroscopy From Radiative Decays of the J/ψ and ψ'*. PhD thesis, SLAC, 1982.

[64] A. R. Bohm and Y. Sato, “Relativistic resonances: Their masses, widths, lifetimes, superposition, and causal evolution,” *Phys. Rev.*, vol. D71, p. 085018, 2005.

[65] L. de Nooij, *The Φ(1020)-Meson Production Cross Section Measured with the ATLAS Detector at $\sqrt{S}$ = 7 TeV*. PhD thesis, Amsterdam U., 2014.

[66] F. Von Hippel and C. Quigg, “Centrifugal-barrier effects in resonance partial decay widths, shapes, and production amplitudes,” *Phys. Rev.*, vol. D5, pp. 624–638, 1972.

[67] N. Wu, “Centrifugal-Barrier Effects and Determination of Interaction Radius,” *Commun. Theor. Phys.*, vol. 61, no. 1, pp. 89–94, 2014.

[68] D. Aston *et al.*, “A Study of K- pi+ Scattering in the Reaction K- p —> K- pi+ n at 11-GeV/c,” *Nucl. Phys.*, vol. B296, pp. 493–526, 1988.

[69] F. Wick, *Charmed Baryon Spectroscopy and Search for CP Violation in $D^0 \to K^0_S \pi^+ \pi^-$ at CDF*. PhD thesis, KIT, Karlsruhe, 2011.

[70] G. Breit and E. Wigner, “Capture of slow neutrons,” *Phys. Rev.*, vol. 49, pp. 519–531, Apr 1936.

[71] M. Pivk and F. R. Le Diberder, “SPlot: A Statistical tool to unfold data distributions,” *Nucl. Instrum. Meth.*, vol. A555, pp. 356–369, 2005.

[72] *ROOT Data Analysis Framework*. https://root.cern.ch/, Accessed: August 28, 2018.

[73] N. Skidmore, *Amplitude analysis of $D^0 \to K^+K^-\pi^+\pi^-$ and its subsequent use in measuring the CKM phase γ through $B^\pm \to D\left(K^+K^-\pi^+\pi^-\right)K^\pm$ decays at LHCb Experiment*. PhD thesis, University of Bristol, Bristol, 2017.

[74] *DfromBBDTs*. https://gitlab.cern.ch/sneubert/DfromBBDTs, Accessed: August 28, 2018.

[75] *DfromBBDTs*. https://gitlab.cern.ch/nskidmor/DfromBBDTs, Accessed: August 28, 2018.

[76] A. Hocker *et al.*, “TMVA - Toolkit for Multivariate Data Analysis,” 2007.

[77] M. Adinolfi *et al.*, “Performance of the LHCb RICH detector at the LHC,” *Eur. Phys. J.*, vol. C73, p. 2431, 2013.

[78] A. Powell, “Reconstruction and PID performance of the LHCb RICH detectors,” *Nucl. Instrum. Meth.*, vol. A639, pp. 260–263, 2011.

[79] R. Aaij *et al.*, “Measurement of the track reconstruction efficiency at LHCb,” *JINST*, vol. 10, no. 02, p. P02007, 2015.

Erklärung

Ich versichere, dass ich diese Arbeit selbstständig verfasst und keine anderen als die angegebenen Quellen und Hilfsmittel benutzt habe.

Heidelberg, den 11.09.2018,